



Polarimetry of Solar System minor bodies and planets

Stefano Bagnulo¹ · Irina Belskaya² · Alberto Cellino³ ·
Yuna G. Kwon⁴ · Olga Muñoz⁵ · Daphne M. Stam⁶

Received: 24 June 2024 / Accepted: 18 October 2024
© The Author(s) 2024

Abstract

The study of the polarisation of light is a powerful tool for probing the physical and compositional properties of astrophysical sources, including Solar System objects. In this article, we provide a comprehensive overview of the state-of-the-art in polarimetric studies of various celestial bodies within our Solar System: planets, moons, asteroids, and comets. Additionally, we review relevant laboratory measurements and summarise the fundamental principles of polarimetric observational techniques.

Keywords Solar System astronomy · Polarimetry · Laboratory astrophysics

Contents

1	Introduction.....	3
2	Asteroids and NEAs.....	7
2.1	Traditional applications of asteroid polarimetry: main belt asteroids.....	7
2.1.1	Determination of the geometric albedo.....	9
2.1.2	Polarimetric parameters as diagnostic of surface regolith properties.....	11
2.1.3	Polarimetry and asteroid taxonomy.....	12
2.1.4	Analysis of spectropolarimetric data.....	13
2.2	Polarimetry of near-Earth asteroids (NEAs).....	15
2.2.1	The DART mission.....	16
2.3	Investigations of unusual classes of objects.....	17
2.3.1	Polarimetric studies of new taxonomic classes.....	20
2.4	Asteroid polarimetry at near-IR wavelengths.....	21
2.5	Future plans for asteroid polarimetry, and synergy with GAIA.....	21
2.6	Conclusions.....	22
3	Jupiter Trojans, Centaurs, TNOs, and icy moons.....	22

Stefano Bagnulo, Irina Belskaya, Alberto Cellino, Yuna G. Kwon, Olga Muñoz and Daphne M. Stam have contributed equally to this work.

Extended author information available on the last page of the article

3.1	Jupiter Trojans.....	22
3.2	Polarimetry of Centaurs.....	23
3.3	Polarimetry of trans-Neptunian objects.....	25
3.4	Polarimetry of icy moons.....	26
3.4.1	Jovian satellites.....	27
3.4.2	Saturnian satellites.....	28
3.4.3	Uranian satellites.....	28
3.5	Comparison of the polarimetric properties.....	28
4	Comets.....	30
4.1	Methodology.....	31
4.2	Main observational results in linear polarisation.....	32
4.2.1	Polarisation-phase curve.....	32
4.2.2	Polarisation spectra.....	33
4.2.3	Polarisation mapping.....	35
4.2.4	Polarisation by gas molecules.....	36
4.2.5	Polarisation by comet nuclei.....	37
4.3	Insights provided by comet polarimetry.....	38
4.3.1	Phase-angle dependence of linear polarisation.....	39
4.3.2	Wavelength dependence of linear polarisation.....	40
4.3.3	Plausible relationship with comet dynamics.....	41
4.4	Open questions.....	42
5	Solar System planets, the Moon, and Titan.....	43
5.1	Phase angles and scattering angles.....	44
5.2	The Moon.....	45
5.3	Mercury.....	47
5.4	Venus.....	48
5.5	Earth.....	50
5.6	Mars.....	53
5.7	Jupiter.....	54
5.8	Saturn.....	57
5.9	Titan.....	58
5.10	Uranus and Neptune.....	59
6	Dusty laboratory measurements and modelling.....	60
6.1	Light-scattering techniques.....	62
6.2	Scattering matrix formalism.....	64
6.3	Experimental polarisation curves under single-scattering conditions.....	65
6.3.1	Size effect.....	65
6.3.2	Composition effect.....	66
6.3.3	Morphology effect.....	69
6.4	Experimental polarisation curves under multiple scattering effects: negative polarisation branch of regoliths.....	71
6.4.1	Regolith grains' composition effect.....	72
6.4.2	Regolith grains size effect.....	72
6.4.3	Particulate media morphology effect: compact vs porous regoliths.....	73
Appendix A: Observing techniques.....		75
A.1:	Definitions.....	75
A.2:	How polarisation is measured.....	77
A.2.1:	Polarimetry with linear polarisers only.....	77
A.2.2:	The beam-swapping technique.....	79
A.2.3:	Chromatism of the retarder waveplate.....	81
A.2.4:	Cross-talk from linear to circular polarisation.....	81
A.3:	Observing techniques and data reduction.....	81
A.3.1:	Broadband polarimetry.....	81
A.3.2:	Polarimetric maps.....	82
A.3.3:	Spectropolarimetry.....	82

A.4: Quality checks.....	82
References.....	84

1 Introduction

Most astronomical observations rely on measurements of the intensity or flux of radiation, and observations of Solar System objects are no exception. However, radiation carries far more information than intensity alone can reveal. Any asymmetry in the source of radiation, or in the scattering medium between the source and the observer, influences the oscillations of the associated electric fields, and the changes in the directions of the oscillations depend on the nature of the asymmetry or on the physical properties of the scatterers. Polarimetric techniques are designed to characterise the changes in these oscillations. By developing theoretical models, we can interpret polarimetric data to infer the properties of the source or the scattering medium.

Solar System bodies, such as planets, asteroids, comets, and moons, scatter sunlight that is incident upon them, either in their atmospheres, or by the particles on their surfaces, or in the cometary comae. Since scattered light is generally polarised, Solar System bodies are primary targets for polarimetric techniques. The first use of polarimetry in astronomy was by the French astronomer François Arago during his observations of the Great Comet in 1819 (Arago 1820). Arago compared the polarised light from the comet's tail with the unpolarised light from the star Capella. His conclusion was that the comet's light was at least in part reflected light, building on the earlier discovery by Malus (1809), who demonstrated that reflected light is generally polarised. The next most significant discovery was made by Lyot (1929), who showed, using an accurate polarimeter of his own design, that the sunlight reflected by the Moon was polarised in the direction perpendicular to what is expected from simple scattering models. It took nearly a century to theoretically interpret this phenomenon, known as *negative* polarisation (see review by Shkuratov et al. 1994). Lyot (1929) provided a comprehensive overview of polarisation observations of the Moon and some planets by Arago and other early observers. He noted that the existing data had too much scatter, and that there was too little information on the accuracy of the instruments used, preventing to perform a meaningful analysis. This prompted Lyot to perform his own measurements. Lyot also compared his observations of Solar System bodies with laboratory measurements of the polarisation of light scattered by various surface types and water droplets.

In the 1970s, it was found that asteroids could exhibit a variety of polarimetric signatures, and that their albedo could be estimated with polarimetric techniques (e.g., Zellner et al. 1974). Applied to planetary atmospheres, polarimetric techniques have, for example, allowed to unveil the size and composition of Venus's clouds (Hansen and Hovenier 1974). In more recent years, it has been investigated how polarimetry could be used for detection and characterisation of extrasolar planets

(Seager et al. 2000; Stam et al. 2004; Fossati et al. 2012; Trees and Stam 2022; West et al. 2022).

The properties of a beam of radiation can be fully specified by four independent quantities. Commonly, we employ the so-called Stokes parameters $IQUV$ (Stokes 1852), where I describes the total intensity or flux, Q and U the linear polarisation, and V the circular polarisation. Detailed definitions of the Stokes parameters can be found in various textbooks and papers (e.g., Landi Degl’Innocenti et al. 2007, and references therein). In Solar System science, circular polarisation is seldom considered, because the signal tends to be very small. It appears to depend mostly on the illumination and viewing geometries, and holds little information about the properties of the scatterers (except in the case of organic materials, see Sect. 5). For symmetry reasons, the objects under study nearly always produce linear polarisation that is directed either parallel to the scattering plane (i.e., the plane that contains both the direction of the incident light and the direction of the scattered light), or perpendicular to it. Therefore, in most situations (and neglecting the circular polarisation), the quantity of interest is

$$P_r(\lambda) = \frac{F_{\perp}(\lambda) - F_{\parallel}(\lambda)}{F_{\perp}(\lambda) + F_{\parallel}(\lambda)}, \quad (1)$$

where F_{\parallel} and F_{\perp} are the fluxes measured through a linear polariser parallel (\parallel) or perpendicular (\perp) to the scattering plane, respectively, and λ represents the wavelength. The absolute value of P_r generally corresponds to the total fraction of linear polarisation, and its sign indicates the orientation of the polarisation plane: trivially, a positive sign means that the polarisation is perpendicular to the scattering plane, and a negative sign means that is parallel to it. Unless otherwise stated, in this review, the term polarisation will refer to the quantity P_r defined by Eq. (1).

Most of the polarimetric studies are based on observations of P_r as a function of the phase angle α , the angle between the direction to the Sun and to the observer as seen from the object (see Fig. 1). For most Solar System objects, but with important exceptions, P_r is negative in the range $0^\circ \leq \alpha \leq 20^\circ$, positive at $\alpha \geq 20^\circ$, and reaches a maximum around $90 - 100^\circ$. The interval of phase angles for which P_r is negative is called the *negative polarisation branch* (NPB). In the NPB, the polarisation typically reaches a minimum (P_{\min}) between 5° and 15° . The angle at which P_r changes its sign is called inversion angle, α_{inv} , and the slope of the curve at the inversion angle, h , are also important characteristic features of the curve (see Fig. 2). It was empirically found that in atmosphere-less bodies of the Solar System, both P_{\min} and h are related to the albedo: the darker the object, the larger P_{\min} and the slope h . More generally, the morphology of the phase-polarisation curve is sensitive to the surface structure and composition of the asteroids (see Sects. 2 and 3), to the scattering properties of cometary dust (Sect. 4), or to the atmosphere of a planet (Sect. 5). For comparison, photometric curves generally have a simple linear behaviour with the phase angle.

Given its rich diagnostic content, it may be surprising that polarimetry is not routinely exploited for studies of Solar System objects. One explanation is that, with the exception of the inner planets Mercury and Venus, the Moon, the near-Earth

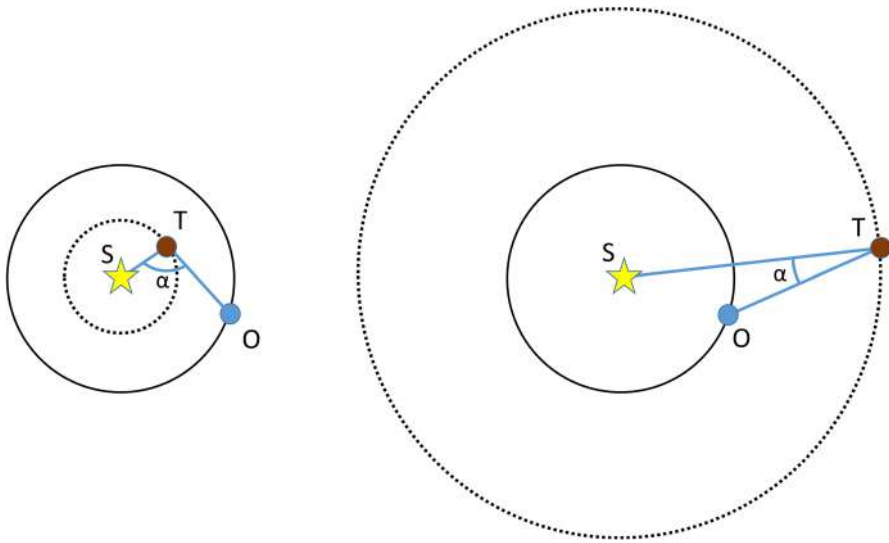


Fig. 1 Illustration of the phase angle α , the angle between the direction to the Sun S and the observer O as seen from target T , when the target is in an inner orbit (left panel) or in an outer orbit (right panel) with respect to the observer. A target in an inner orbit can be observed at phase angles ranging from close to 0° to close to 180° . For a target in an outer orbit, the minimum phase angle is (close to) zero, and the maximum phase angle at which it can be observed from Earth is given by $\arcsin(1/r)$, where r is the target's heliocentric distance expressed in astronomical units (au)

asteroids (NEAs), and occasionally certain comets, Solar System objects are generally observed under small phase angles from Earth (see Fig. 1), and thus under somewhat unfavourable geometries, resulting in small polarisation signals, typically around 1% or even less. Asteroids in the main belt are often in viewing conditions corresponding to phase angles close to the inversion of their polarimetric curves. The giant planets can be observed only at small phase angle, in the NPB. The maximum phase angle at which trans-Neptunian objects (TNOs) can be seen is $\leq 2^\circ$. The consequence is that, with ground-based observations, the observed polarisation features of objects with entirely different scattering properties are not so well differentiated as they would be if the same objects could be viewed over a much wider range of phase angles. Therefore, for polarimetric measurements at such small phase angles to still be useful, they often need an accuracy better than 0.1%. Detection of such small polarisation signals requires exposure times as if the sources were 1000 or 10000 times fainter than they appear when observed with traditional photometric or spectroscopic techniques using the same telescope.

Another challenge is that, similar to how light scattered by an asteroid is polarised, light reflected by any oblique mirror positioned in front of polarimetric optics introduces instrumental polarisation. This can significantly impact scientific measurements, if the polarimeter is attached for instance to a Nasmyth focus. To minimise this effect, measurements of the polarisation of the continuum are best performed with instruments attached at the prime focus or the Cassegrain focus of a telescope. This imposes practical limitations—in fact, some telescopes may not even

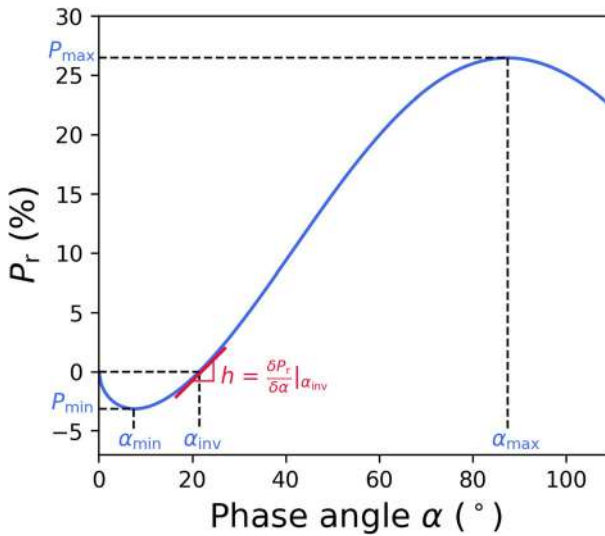


Fig. 2 An example of a polarisation phase curve of a Solar System object, with its main characteristics. The curve is produced using Eq. (7) with $b = 0.4$, $c_1 = 0.55$, $c_2 = 1.0$, $\alpha_{\text{inv}} = 21.5^\circ$. We note that, with ground-based observations, such a large phase angle range would only be accessible for a limited number of objects, such as the inner planets, the Moon, some so-called near-Earth asteroids, and certain comets

have a prime or a Cassegrain focus. In practical terms, only a few observatories are equipped with instruments capable of measuring the polarisation of Solar System objects, and even fewer are available as common-user facilities. Perhaps, the most useful and frequently used instrument with polarimetric capabilities in the continuum, accessible to a wide international community through competitive proposals, is the FORS2 instrument (Appenzeller et al. 1998) of the European Southern Observatory (ESO) Very Large Telescope (VLT). Other instruments are typically available only to smaller consortia, which may be open to external collaborations.

Finally, the theoretical interpretation of observations is often complex, precisely because the polarisation is very sensitive to the physical properties of the scatterers. Although empirical formulas exist that can quickly estimate an asteroid's albedo from a limited number of polarimetric observations (see Sect. 2.1.1), further data interpretation typically requires sophisticated and time-consuming modelling.

Polarimetry of Solar System objects covers so many diverse aspects that we can only provide a broad overview of its key aspects. Whilst the Sun is the most intensively observed object in polarimetric studies, particularly for investigating its magnetic field, this review will focus on other celestial bodies, such as planets, moons, asteroids, and comets, and will omit discussions of solar polarimetry. Atmosphereless objects such as main belt asteroids and near-Earth asteroids (NEAs) are discussed in Sect. 2. Next, in Sect. 3, trans-Neptunian objects, Centaurs, Jupiter Trojans, and icy moons of the planets are discussed. Comet polarimetry is reviewed in Sect. 4, and planets (including Earth), the Moon, and Titan in Sect. 5. Section 6 is about laboratory measurements and modelling of light scattered by dust.

Finally, readers interested in more details about the observational aspects may refer to Appendix A.

2 Asteroids and NEAs

The foundations of modern asteroid polarimetry were laid in the 1960s and 70s, with the first polarimetric measurements (mostly main belt asteroids), and comparisons with laboratory studies. Some early, important investigations were published by [Bowell and Zellner \(1974\)](#) in the *Planets, Stars and Nebulae studied with Photopolarimetry* book. A short list of a few other seminal papers published in those years includes [Zellner et al. \(1974\)](#), [Zellner and Gradie \(1976\)](#), [Zellner et al. \(1977\)](#), and [Dollfus and Zellner \(1979\)](#).

In these early investigations, many of the important properties concerning the polarimetric behaviour of the light we receive from the small bodies of the Solar System, in particular those having solid, rocky surfaces, were described. One of these fundamental properties is that at visible wavelengths, the sunlight scattered from these bodies is in a state of partial linear polarisation, which depends upon the so-called phase angle (see Sect. 1). Furthermore, whenever small bodies are seen as point sources (which is true for all asteroids and NEAs), for symmetry reasons, the polarisation is always either perpendicular or parallel to the scattering plane.

In the case of main belt asteroids, the maximum attainable value of phase angle, which is orbit-dependent, rarely exceeds 30° . In the case of near-Earth asteroids (NEAs), which can have close approaches with the Earth, much higher values of phase angle are possible, up to more than 100° in some circumstances, although not all NEAs can be observed in any given apparition over a sufficiently wide range of phase angles to measure P_{\max} (see Sect. 2.2). NEAs are a much less numerous population than main belt asteroids, and they are generally much fainter. Moreover, their apparent motion is much faster. They are visible from ground-based facilities only for relatively short intervals of time. Their phase angle also changes quickly, even in the course of a few nights. Because of these important differences in the viewing conditions, and, consequently, in the outcome of observations, we will treat these two classes of objects separately (Sects. 2.1 and 2.2, respectively). Other classes of special asteroids will also be described in Sects. 2.3. Obviously, all sections are closely linked to each other, and in particular, the one dedicated to main belt asteroids includes general concepts and results that apply to other classes of objects.

2.1 Traditional applications of asteroid polarimetry: main belt asteroids

The shape of the phase-polarisation curves of main belt asteroids, which are visible in a limited interval of phase angles, can be described using the empirical representation ([Muinonen et al. 2009](#))

$$P_r(\alpha) = A(e^{-B/\alpha} - 1) + C\alpha, \quad (2)$$

where A , B , C are free parameters to be derived for each object from the phase-

polarisation data, and α is the phase angle. Empirically, it is found that this representation is valid up to phase angles of $50 - 60^\circ$, and hence may not be always suitable for NEAs and comets. At smaller phase angles, it can describe the behaviour of all known phase-polarisation curves. As an example, Fig. 3 shows two very different cases, corresponding to a high-albedo asteroid and a low-albedo asteroid. The differences amongst the phase-polarisation curves of different objects are very important, because they are diagnostic of the values characterising some important physical properties, including primarily the geometric albedo.

It is remarkable that the state of linear polarisation of the asteroids in a given wavelength range is a function of the phase angle only. In principle, one could expect that the polarisation of the scattered sunlight depends also on the side of the surface of the asteroid illuminated by the Sun. In practice, apart from a very few cases (the most important one being that of the large asteroid (4) Vesta (Cellino et al. 2016; Wiktorowicz and Nofi 2015), observations of the same asteroids obtained at very different epochs, corresponding to a wide variety of visible and illuminated regions of their surfaces, but at similar phase angles, are fully consistent amongst themselves. This means that asteroid surfaces are significantly homogeneous, at least in terms of the properties that determine the outcome of light scattering.

The case of (4) Vesta is peculiar in many respects. With its diameter of about 500 km, it is one of the largest main belt asteroids. Its general shape is close to a spheroid, and its brightness variations at different apparitions are mostly determined by an important albedo variegation, predicted by Degewij et al. (1979), Cellino et al. (1987) and subsequently proven by in situ observations by the *Dawn* probe (see, for what concerns ground-based polarimetric measurements of Vesta, Cellino et al. 2016, and references therein). In addition, (4) Vesta is known to have a very unusual surface composition, mostly basaltic (McCord et al. 1970). Its reflectance spectrum makes it the prototype of a rare taxonomic class (V, from Vesta). The large majority of V-class asteroids are members of the Vesta dynamical family, thought to be formed by fragments ejected by energetic impact cratering events, whose remnants are well visible in the *Dawn* high-resolution images.

In many respects, asteroid polarimetry has been for a long time a discipline mostly based on laboratory experiments and empirical relations. The most traditional activities have been mostly aimed at exploiting the fact that the parameters describing the morphology of the phase-polarisation curves had been found to be diagnostic of some important physical properties of the surfaces, including primarily the geometric albedo (Sect. 2.1.1) and the properties of surface regoliths (Sect. 2.1.2). Polarimetry is also an important technique for asteroid classification (Sect. 2.1.3).

Starting since the 1990s, there was an increasing interest in organising new observation campaigns. The consequent increase of the data-set of asteroid polarimetric measurements,¹ led to the discovery of new classes of objects exhibiting unusual polarimetric properties. Investigating the behaviour of these objects became

¹ A traditional repository of asteroid polarimetric data is maintained by D.F. Lupishko at the NASA Planetary Data System at <http://pds.jpl.nasa.gov/>. Another catalogue, maintained by R. Gil-Hutton, is available at <http://gcpjsj.sdf-eu.org/catalogo.html>. The catalogue of polarimetric data taken at Calern (see Bendjoya et al. 2022) is available at the CDS via anonymous ftp to cdsarc.u-strasbg.fr (130.79.128.5) or via <http://cdsarc.u-strasbg.fr/viz-bin/cat/J/A+A/665/A66>.

an important field of investigation. In the following, we briefly describe some major topics which have been objects of investigation in the last decades.

2.1.1 Determination of the geometric albedo

The geometric albedo is defined as the ratio between the brightness of a body measured in a standard V filter at zero phase angle (ideal solar opposition) to that of an idealised flat, diffusively scattering (Lambertian) disc with the same cross-section, observed at the same distance. This parameter, which quantifies the intuitive notion of intrinsic brightness or darkness of a surface at visible wavelengths, is of fundamental importance to characterise the surface of an object, being directly related to its composition and also to the macroscopic and microscopic roughness and texture of the surface layer responsible of the scattering of incoming sunlight. A well-known relation links together the geometric albedo $p_{\mathcal{F}}$ (where \mathcal{F} is a photometric filter), with two other fundamental properties of an asteroid, namely its size (or equivalent diameter) D , and its absolute magnitude $H_{\mathcal{F}}$, which is the magnitude in the \mathcal{F} filter that an asteroid would have if observed at ideal solar opposition (0° phase angle) at 1 au from both the Sun and an observer

$$\log(D) = K - 0.2 H_{\mathcal{F}} - 0.5 \log(p_{\mathcal{F}}); \quad (3)$$

K is a constant that, in the case of data taken in a V filter, takes the value $K = 3.1236$ (see, for instance, Cellino et al. 2012, and references therein). The determination of the geometric albedo is therefore essential to derive the size of an object for which the absolute magnitude H is known, or to derive H for an object for which size and albedo are known.

In the most common situations, one wants to derive $p_{\mathcal{F}}$ from knowledge of size and absolute magnitude $H_{\mathcal{F}}$. Size D may be accurately determined from thermal IR flux measurements or star occultation observations, whilst the value of $H_{\mathcal{F}}$ may be derived from photometry by extrapolating to zero phase angle magnitude measurements obtained at non-zero phase angles during a given apparition of the object. Unfortunately, however, asteroid magnitudes tend to have an unpredictable and non-linear surge when observed at increasingly smaller phase angles, and their sizes are often not very well known.

The existence of some empirical relations between the geometric albedo and some of the parameters describing the phase-polarisation curves (see Sect. 1) has always been exploited to derive $p_{\mathcal{F}}$ from polarimetric data, without the need of any ancillary information. The relations between the slope h and the P_{\min} polarimetric parameters measured in the \mathcal{F} photometric filter and $p_{\mathcal{F}}$, based on empirical data are usually expressed in the form

$$\begin{aligned} \log(p_{\mathcal{F}}) &= C_1 \log(h_{\mathcal{F}}) + C_2 \quad \text{or} \\ \log(p_{\mathcal{F}}) &= C_3 \log(P_{\mathcal{F}}^{\min}) + C_4 \end{aligned} \quad (4)$$

We note that the photometric filter adopted in nearly all practical cases is the standard V filter, due to lack of polarimetric data taken in different bands. Alternative relations

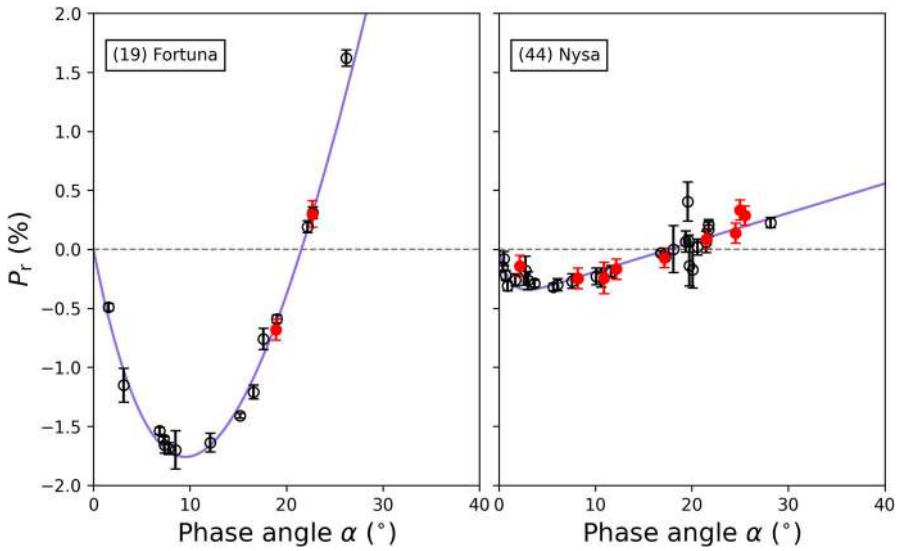


Fig. 3 Phase-polarisation curves of two main belt asteroids. Left panel: (19) Fortuna, a low-albedo object. Right panel: (44) Nysa, a very high-albedo asteroid. Red symbols show data obtained in the framework of the CAPS survey (see Sect. 2.5) and highlight that coherent and self-consistent phase-polarisation curves are obtained even by combining data taken at very different epochs and using different instruments. The best-fit curves have been computed using the exponential-linear function (see Eq. 2)

between albedo and polarisation have been suggested in the literature, for instance by using, instead of h or P_{\min} , the parameter

$$\Psi = P_r(30^\circ) - P_r(10^\circ) \tag{5}$$

(Cellino et al. 2015), or the parameter

$$p^* = (0.79 \pm 0.02) \log(h) + (0.61 \pm 0.03) \log(P_{\min}) \tag{6}$$

(Masiero et al. 2012). The general idea is that parameters such as Ψ and p^* may better reflect the overall behaviour of the phase-polarisation curve (see Cellino et al. 2015, in particular their Table 1, and references therein).

Whatever parameters are adopted, Eq. (4) needs to be calibrated using accurate polarimetric data for a large sample of asteroids of known size and absolute magnitude, ideally in various filters. A suitable large calibration database does not exist yet. The most recent, systematic investigations are by Cellino et al. (2015) and Lupishko (2018), and are limited to the V filter. The validity of their “recipes” to derive the geometric albedo from polarimetric data was confirmed by an analysis of disc-integrated polarisation measurements obtained at different epochs for the asteroid (4) Vesta, and the *in situ* spectroscopic and photometric measurements of the Vesta’s surface by the *Dawn* space mission (Cellino et al. 2016, and references therein). Asteroid (4) Vesta is an ideal target for this kind of investigation also, because it has a well-known surface heterogeneity in surface composition, which is also related to the presence of big impact craters. An analysis of the available

Table 1 Polarimetric parameters of satellites

Satellites	D^1	Albedo	$ P_{\min} $ (V)	α_{\min}	Reference
<i>Jupiter satellites</i>					
Io	3643	0.63	0.25±0.02	2.1±0.5	Kiselev et al. (2024a)
Europa	3122	0.67	0.26±0.03	0.3±0.1	Kiselev et al. (2022a)
Ganymede	5262	0.43	0.34±0.01	0.5±0.1	Kiselev et al. (2024a)
Callisto	4821	<0.2 (L) 0.2 (T)	0.85±0.05 0.63±0.05	10.1±0.3 4.9±0.4	Rosenbush et al. (2002)
Himalia	170	0.06 ²	1.6	7	Degewij et al. (1980)
<i>Saturnian satellites</i>					
Enceladus	504	1.24	0.51	2.4	Zaitsev et al. (2015b)
Rhea	1527	0.89	0.57	2.2	Zaitsev et al. (2015a)
Iapetus	1469	0.04 (L) 0.55 (T)	1.2 0.7	4 1	Rosenbush et al. (2015)
Dione	1123	0.75 (T)	0.83	1.6	Rosenbush et al. (2015)
Titan	5150				See Sect. 5.8
<i>Uranian satellites</i>					
Ariel	1158	0.36	1.4	1	Afanasiev et al. (2014)
Titania	1578	0.30	1.2	1.4	Afanasiev et al. (2014)
Oberon	1523	0.22	1.1	1.8	Afanasiev et al. (2014)
Umbriel	1169	0.20	1.7	2.4	Afanasiev et al. (2014)

¹https://ssd.jpl.nasa.gov/sats/phys_par/²Grav et al. (2015)

“polarimetric lightcurves” of Vesta, namely the remote measurements of the variation in disc-integrated polarisation as a function of rotation, led to confirm that the predictions of the albedo of different regions of Vesta based on the measured $h - p_V$ data were basically correct. Of course, this first example of “ground-truth” in asteroid polarimetry is valid only for the limited range of relatively high albedo characterising (4) Vesta.

2.1.2 Polarimetric parameters as diagnostic of surface regolith properties

Early investigations based on laboratory analyses of the polarimetric properties of different samples of materials, of both terrestrial and meteoric origin, had suggested that the measured values of the parameters describing the phase-polarisation curves were strongly dependent upon the state of fragmentation of the samples (Dollfus et al. 1989). It should be noted that, in the case of the Moon, polarimetric measurements and comparison with laboratory experiments had been used many decades ago to infer the presence of a layer of fine regolith covering the lunar surface, well before the landing of the first lunar exploration missions, which confirmed these predictions (Dollfus 1961; Dollfus et al. 1971).

Dollfus et al. (1989) suggested that the location of asteroid polarimetric data in the $P_{\min} - \alpha_{\min}$ plane should be considered to be diagnostic of the average sizes of surface regolith particles. In this plot, asteroids belonging to different taxonomic classes characterised by different values of the geometric albedo were found to be well distinguished in terms of their P_{\min} values, but they were characterised by similar inversion angles, mostly between 18° and 22° . According to Dollfus et al. (1989), these values of the polarimetric inversion angle are typical for pulverised meteorites and terrestrial silicates having grain sizes between 30 and $300 \mu\text{m}$ (see also Sect. 6.4.2). The location of asteroid data in the $P_{\min} - \alpha_{\min}$ plane was found in a region in between those occupied by bare rocks ($\alpha_{\text{inv}} < 18^\circ$) and by lunar fines ($18^\circ \leq \alpha_{\text{inv}} \leq 25^\circ$). This led Dollfus et al. (1989) to the conclusion that asteroid surfaces are covered by a regolith that is coarser than lunar surface, but finer than bare rocks. They also suggested that this could be a consequence of a depletion of fine regolith particles caused by collisions, assuming that the smallest fragments are ejected at speeds exceeding the escape velocity of these small bodies.

Nowadays, these classic results are still relevant, but in recent years, there has been the discovery of classes of objects which occupy regions of the $P_{\min} - \alpha_{\text{inv}}$ plane where no objects were known to exist at the epoch of the *Asteroids II* book. This can be seen in Fig. 4. Some mixing of low-albedo objects is visible, but this can be a consequence of using slightly uncertain albedo values. What is more important is that in the modern $P_{\min} - \alpha_{\text{inv}}$ plot, there are several objects located at high values of the polarimetric inversion angle, largely exceeding the region of lunar fines identified by Dollfus et al. (1989). Moreover, the region located at low values of α_{inv} angle smaller than 18° is now populated. These facts are related to the existence of classes of objects characterised by unusual polarimetric properties, as discussed in Sect. 2.3.

2.1.3 Polarimetry and asteroid taxonomy

Asteroid taxonomy has been historically based on multi-band photometry data and reflectance spectra of the objects at visible and near-infrared wavelengths (Bowell and Lumme 1979; Gradie and Tedesco 1982; Tholen 1984; Bus and Binzel 2002; DeMeo et al. 2009). However, even since the first extensive analysis by Tholen (1984), it was discovered that objects exhibiting very similar reflectance spectra could be distinguished based on important differences in the albedo estimated by polarimetric investigations. In particular, the E, M, P taxonomic classes turned out to be characterised by very similar, reddish reflectance spectra, and the only way to discriminate amongst objects sharing this property was to consider their albedo, which turned out to be very high, average, and low, respectively, for the three above-mentioned classes. Penttila et al. (2005) showed that a taxonomic classification based on polarimetric properties alone was possible. However, at that time, the fraction of known asteroids having well-determined polarimetric phase-polarisation curves was very low, and the Penttila et al. (2005) results had no fundamental impact on asteroid taxonomy. In more recent times, after the increase of published polarimetric data, Belskaya et al. (2017) could develop a deeper analysis of the differences in the polarimetric behaviour of asteroids belonging to different taxonomic classes, and

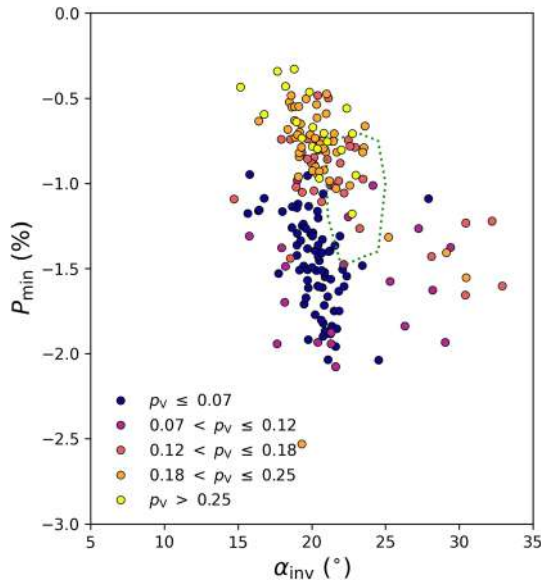


Fig. 4 Plot of the P_{\min} parameter vs. the polarimetric inversion angle. The polarimetric parameters shown in this plot have been derived by processing all available literature data, including also those recently published by Bendjoya et al. (2022). This plot replaces now the classical plot by Dollfus et al. (1989). The albedos used to colour-code the data points have been taken from the MP3C repository (<https://mp3c.oca.eu/>). The area delimited by the dots corresponds to the region occupied by thin lunar fines in the original Dollfus et al. (1989) plot. This area, which was nearly empty at the epoch of the *Asteroids II* book, is now populated by many objects, mainly of middle-to-high albedo

Belskaya et al. (2022) demonstrated the ability of polarimetry to distinguish subtypes amongst M-class asteroids. In the current situation, it is sure that polarimetric data are fundamental input for analyses of many individual objects, especially those being rather bright, whilst in the case of the large fraction of very small and faint objects, polarimetric data are still insufficient to play a primary role. An important exception can become that of newly discovered NEAs (Kiselev et al. 2024b), for which, in case of a possible intersection with the Earth's orbit, quickly obtained polarimetric data can become crucial to infer the size and albedo, in such a way as to determine the risk posed by such objects.

2.1.4 Analysis of spectropolarimetric data

Historically, most polarimetric investigations of asteroids have been based using V band data. The first extensive analysis of multi-band optical data was published by Belskaya et al. (2009) (see also references therein). In that paper, some of the most important features of the relation between the state of linear polarisation and the wavelength were discovered. In most general terms, at optical wavelengths, from blue to red, the fraction of linear polarisation as a function of wavelength is found to change, but in a quite complicated way. In particular, for any given object, the polarisation state as a function of wavelength depends upon whether the object is

observed in the negative or the positive polarisation branch. By calling “red polarisation” the situation in which linear polarisation increases (in module) for increasing wavelength, and “blue polarisation” the situation in which polarisation decreases (again, in module) for increasing wavelength, it has been found that whenever an object displays red polarisation in the negative branch, then it will exhibit blue polarisation when observed in its positive polarisation branch, and vice versa (the inversion of the polarisation slope in *S*-type asteroids was noted earlier by Kiselev et al. 1994). Interestingly, in this respect, the behaviour of intermediate-albedo, *S* class asteroids has been found to be opposite to that of low-albedo, *C* class asteroids. These preliminary results were later confirmed by Bagnulo et al. (2015) in their first application to asteroids of the full spectropolarimetric technique, in which it is possible to analyse the continuous variation of both reflectance and linear polarisation as a function of wavelength.

With respect to polarimetric measurements limited to one optical band, only spectropolarimetry adds a new dimension to the description of the asteroid’s surface properties. Not only it is still possible to derive normal reflectance spectra and monochromatic polarisation properties, but a new observable, namely the polarimetric gradient as a function of wavelength, can be analysed. As a trivial example, the dependence upon the wavelength of the polarimetric inversion angle can be easily determined and linked to other surface properties, including those that determine the classical phase-polarisation parameters, the albedo, the most likely composition derived from reflectance spectroscopy, and the taxonomic classification.

Spectropolarimetric properties have been analysed also in a more recent work by Kwon et al. (2023). This analysis was limited to a sample of 64 sizeable asteroids belonging to the *C* taxonomic complex, which includes several taxonomic sub-classes. Some differences in the spectropolarimetric behaviour were found to distinguish amongst different sub-classes, and were tentatively interpreted in terms of composition and possible aqueous alteration.

Compared to reflectance spectra, that need an accurate calibration sometimes difficult to achieve, polarisation spectra can be routinely measured with very high precision. The reason is that flux measurements, even when normalised using a solar analogue observed with the same instrument as the primary target, are always influenced by the Earth’s atmospheric transmission, which can vary during the course of a single observing night. Even relative reflectance spectra (normalised to a specific wavelength) can be affected, as changes in the wavelength-dependent transparency of the sky may occur. Polarimetric measurements instead are virtually independent of the atmospheric conditions, if obtained with the beam-swapping technique (see Sect. A.2.2). Polarisation spectra depend on the phase angle at which they are obtained, but once they are normalised to the value at a certain wavelength (e.g., 550 nm), their shape depends mainly on whether they were obtained in the negative or in the positive branch (Bagnulo et al. 2015). Overall, polarisation spectra offer a diagnostic complementary to that of reflectance spectra. The main limitation is due to the still small amount of available data, but this could be easily overcome by new observing programmes.

2.2 Polarimetry of near-Earth asteroids (NEAs)

Compared to main belt asteroids, NEAs have much closer approaches with the Earth, and observations at much higher values of phase angle are possible (up to more than 100° in some cases), although not all NEAs can be observed in any given apparition over a sufficiently wide range of phase angles to determine P_{\max} .

In principle, all the asteroids having aphelion distance larger than 0.983 AU (the perihelion distance of the Earth) can be observed (sooner or later) at, or very near to solar opposition. The only notable exception are the so-called Atira (also known as Apohela) objects, a rare class of NEAs (including only a handful of objects with well-determined orbits) with orbits completely interior to the one of the Earth. The maximum attainable phase angle depends also upon the orbital properties of the target asteroids, and increases as the asteroid's semi-major axis decreases.

Equation (2) is not adequate for objects observed at phase angles $\geq 50^\circ - 60^\circ$, and is often replaced by

$$P_r(\alpha) = A \sin^B(\alpha) \cos^C\left(\frac{\alpha}{2}\right) \sin(\alpha - \alpha_{\text{inv}}), \quad (7)$$

where A , B , C , and α_{inv} are parameters to be determined by means of best-fit techniques (see, e.g., Goidet-Devel et al. 1995, and references therein).

The fact that NEAs can attain large-phase angles is a noticeable advantage for polarimetric studies, because polarisation reaches high values, and differences between different bodies may be better appreciated. At large values of the phase angle, NEAs reach a maximum of positive polarisation P_{\max} . Based on extensive laboratory experiments using meteorite samples and relevant mineral assemblages of terrestrial origin, the value of this parameter and the corresponding phase angle of its occurrence have long been considered to be diagnostic of the geometric albedo and of the grain size of surface regolith (see, e.g., Geake and Dollfus 1986, and references therein). Unfortunately, polarimetric data of asteroids observed at very large-phase angles are rare and generally poorly sampled. As a consequence, it is difficult to derive in most cases an accurate determinations of P_{\max} , and the relation between the geometric albedo and P_{\max} is still subject to uncertainties, as discussed in recent articles, including Borisov et al. (2018), Ito et al. (2018), and Kiselev et al. (2022b), which are devoted to the NEA (3200) Phaethon. On the other hand, however, one or a few polarimetric measurements obtained in the positive polarisation branch, where the degree of linear polarisation tends to exhibit big changes for objects of different albedo, can be sufficient to assign a generic albedo class (low, intermediate or high) to any NEA, including newly discovered ones. As a consequence, NEA polarimetric studies are considered to be very important not only because NEAs reach the near-Earth region coming from a variety of dynamical routes starting at different heliocentric distances, but also based on considerations taking into account the mitigation of the danger posed by the existence of bodies which may have collisions with the Earth. In particular, the possibility to derive in a relatively short time an estimate of the albedo of an NEA (possibly including a recently discovered, potential impactor) by means of a few polarimetric measurements is very important for the determination of some of its basic physical properties. The recent NEOROCKS

project (Petropoulou et al. 2022), which received funding from the European Union's Horizon 2020 research and innovation programme, has been aimed at drastically improving our knowledge of the dynamical and physical properties of NEAs using extensive observations using a wide variety of techniques. This included also a polarimetric survey of NEAs using the 1-m telescope of Calern (France). More than 100 new single polarimetric measurements have been obtained for 24 NEAs, most of whom had never been observed before using a polarimeter. After a consolidation phase, the NEOROCKS web portal and database is currently planned to migrate within the Space Science Data Center of the Italian Space Agency (ASI-SSDC) to be hosted in a permanent infrastructure devoted to space-data management (<https://www.ssdsc.asi.it/>) and made accessible to external users.

2.2.1 The DART mission

The Double Asteroid Redirection Test (DART) mission has been conceived to study and demonstrate the effectiveness of the kinetic impact technique for deflecting potentially hazardous asteroids (e.g. Daly et al. 2023). As a consequence of the impact, there was the formation of a dust cloud of ejected material (Li et al. 2023; Opitom et al. 2023). Bagnulo et al. (2023) and Gray et al. (2024b) carried out a polarimetric study of the event in different visible bands. This was the first time that the polarimetric consequences of a collisional event involving a real asteroid were measured, allowing a direct comparison of the polarimetric state before the impact, a short time after it, and during several weeks of post-impact evolution (see Fig. 6). It was found that, just after impact, the fraction of linear polarisation dropped significantly in all the bands from *B* to *R* as a direct consequence of the impact (Bagnulo et al. 2023). Possibly, this decrease of polarisation was due to a decrease of the particle size (due to surface boulders fragmentation), or a change of its composition, because space weathered surface material was removed by the impact. The linear polarisation continued to linearly increase with increasing phase angle, with a slope similar to that measured before the impact, and the drop of polarisation persisted for at least 4 months, even after the majority of the dust cloud has dissipated (Gray et al. 2024b). The polarisation spectrum showed only very little or no change over the course of the observations executed before and after impact (Bagnulo et al. 2023). This lack of any remarkable change in the polarisation spectrum after impact suggests that the way in which polarisation varies with wavelength depends primarily on the composition of the scattering material, both on the asteroid surface and in a debris cloud. The observed polarisation was modelled in detail by Penttilä et al. (2024).

A better understanding of the consequences of the collision provoked on the Didymos satellite by the DART impactor could come soon from the Hera space mission. This is a planetary defence mission of the European Space Agency (ESA), launched in October 2024. Its objectives are to investigate the Didymos binary asteroid, and to make an accurate first assessment of the outcome of NASA's DART impactor test.

2.3 Investigations of unusual classes of objects

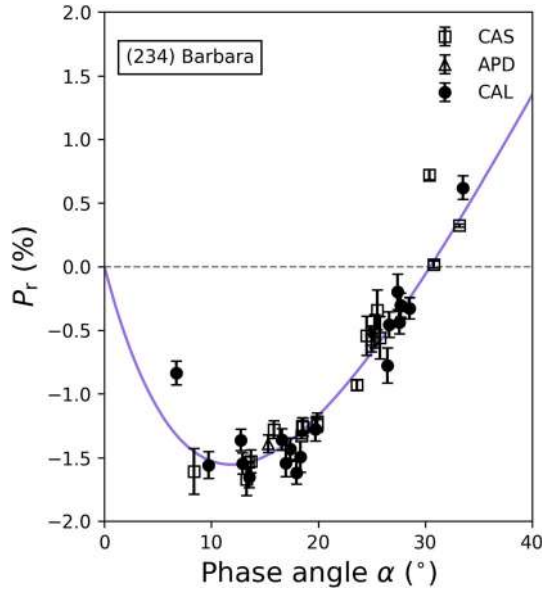
There are asteroids which are known to exhibit peculiar polarimetric properties. These include the class of the so-called Barbarians, as well as the *F* taxonomic class, including low-albedo asteroids which can be important for the possible identification of active asteroids. In addition, there are some single objects for which available polarimetric data do not fit the expectations based on the results of other observation techniques. Examples are given by (21) Lutetia, and by the so-called Vestoids located in the mid-to outer regions of the main belt (Oszkiewicz et al. 2023).

The so-called Barbarian asteroids are named after the name of the prototype of the class, asteroid (234) Barbara, whose unusual polarimetric behaviour was discovered by Cellino et al. (2006). The peculiarity of the phase-polarisation curve of this asteroid is the large width of its negative polarisation branch, the polarimetric inversion angle reaching a value around 30° (see Fig. 5). After this first discovery, there was a big effort to discover other asteroids exhibiting the same behaviour, looking specially at objects belonging to the same taxonomic class of Barbara. The current sample of Barbarians includes now more than 30 asteroids. In all cases in which a reflection spectrum is available, the Barbarians belong to the *L* taxonomic class according to the Bus-DeMeo classification (DeMeo et al. 2009), based on data collected at both visible and near-IR wavelengths. A general description of the current ideas about the properties of these objects can be found in Devogèle et al. (2018b). The peculiar polarimetric behaviour of these objects is interpreted as a consequence of the peculiar composition of their surface regolith. In particular, spectroscopic evidence strongly suggests that Barbarian surfaces have an anomalous overabundance of the spinel mineral. Spinel ($[\text{Fe}, \text{Mg}]\text{Al}_2\text{O}_4$) is an important component of the so-called Calcium Aluminium-rich inclusions (CAIs) found in meteorites. The spinel is a very refractory compound, and is thought to be one of the first minerals to solidify when the temperature of an originally melt planetary disc starts to decrease. For this reason, although there is not yet a general consensus about this, it is possible that Barbarians could be extremely ancient, the possible remnants of an early generation of planetesimals grown during the very early stages of the evolution of our Solar System.

An important discovery was that one of them, (729) Watsonia, is the largest member of a small dynamical family consisting of high-inclination asteroids (Cellino et al. 2014). Because the members of any dynamical family are fragments from the collisional disruption of an original parent body, the fact that all the observed members of the Watsonia family exhibit the typical polarimetric properties of the Barbarian class proves that the Barbarian behaviour is due to physical properties which are determined by the overall composition of these objects, not limited to their surface layers.

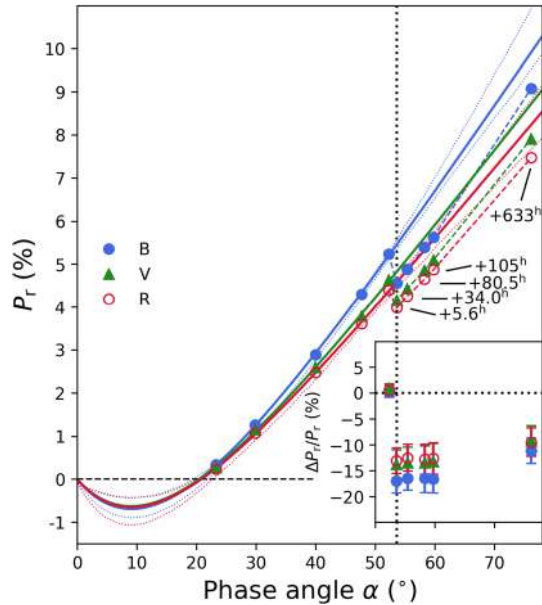
More recently, Bendjoya et al. (2022) carried out an updated analysis of the polarimetric properties of the Barbarians. According to these authors, there are reasons to believe that the Barbarians might consist of more than one sub-classes. Due to their interesting properties, Barbarians keep being high-priority targets for current programmes of polarimetric observations of asteroids.

Fig. 5 The phase-polarisation curve of asteroid (234) Barbara. Different symbols are used to distinguish between data listed in the Asteroid Polarimetric Database (APD) available at the NASA Planetary Data System, whilst other data have been obtained at the CASLEO observatory (CAS) in Argentina, and published in different papers (see, for a summary, Devogèle et al. 2018a) and at the Calern observatory (CAL), in the framework of the CAPS survey (see Sect. 2.5). The best-fit curve has been computed using the exponential-linear function of Eq. (2)



The F taxonomic class was first identified by Gradie and Tedesco (1982) and later included in Tholen’s taxonomy based on multi-band photometry (Tholen 1984). It is characterised by a very flat reflectance (F stands for “flat”), down to short wavelengths in the blue spectral region. In the more modern era of CCD detectors, the blue region is no longer adequately covered, and the old F class no longer exists. The objects originally classified as F are nowadays included as members of the larger B taxonomic class of the Bus-DeMeo taxonomy (DeMeo et al. 2009). According to Belskaya et al. (2005) and Belskaya et al. (2017), however, the members of the older F class are characterised by a peculiar polarimetric property and can be distinguished by other members of the modern B class. What makes the F class members special is their small values of the polarimetric inversion angle, generally $< 16^\circ$. A comparison between the largest member of the modern B class and the largest member of the old F class is shown in Fig. 7. As stressed by Devogèle et al. (2018a), amongst the asteroids originally classified as members of the F -class of the Tholen taxonomy (Tholen 1984), there is an object, (4015) Wilson-Harrington (Bowell et al. 1992) that at the epoch of its discovery and first photometric observations was classified as an F -class asteroid. However, it was later found to exhibit cometary activity. Because no further activity has been detected again in subsequent years, there are reasons to believe Wilson–Harrington might be a comet observed at epochs when it was becoming extinct. Another important fact is that polarimetric observations of two comets, 2P/Encke (Boehnhardt et al. 2008) and 133P/Elst-Pizarro (Bagnulo et al. 2010) showed that their nuclei exhibit a polarimetric behaviour characterised by low inversion angles, similar to those of F -class asteroids. In this respect, Kolokolova and Jockers (1997) proposed that a low inversion angle of polarisation could be diagnostic of a cometary surface.

Fig. 6 Phase-polarisation curves of the Didymos-Dimorphos binary system before and after the moon Dimorphos was hit by the DART probe. Phase angle was increasing with time and the dotted line shows the value at which the impact occurred. Observations obtained after impact are marked with the time elapsed after impact. The solid lines show the extrapolation of the polarisation curves using only the points obtained before impact. The inset shows the fractional variation of the polarisation with respect to the extrapolated curves



The possibility that asteroids originally classified as members of the old *F*-class display properties diagnostic of a cometary origin is exciting, due to the fact that, as discussed above, *F*-class asteroids can be identified based on their uncommon polarimetric properties. Interestingly, Cellino et al. (2018) found that the asteroid (101955) Bennu, the target of the OSIRIS-REx space mission, exhibits the polarimetric properties which characterise the *F* class. This result was obtained before the arrival of the space probe to its target. The results of the first data collected by OSIRIS-REx revealed a low-albedo asteroid having a surface rich in hydrated minerals, and showing a moderate surface activity (Hergenrother et al. 2020). Evidence of original flow of water within this asteroid has been found by Ishimaru and Lauretta (2024) based on analyses of the sample of surface material brought back to Earth by the OSIRIS-REx probe. This supports the idea of a possible cometary nature of this object, and provides another reason why the search for asteroids belonging to the *F* class is a high-priority task for present and future polarimetric observing programmes, at the same time emphasising the role of the study of polarimetric properties as an invaluable tool to understand the physical properties and previous history of small Solar System bodies.

We also mention an extensive investigation of an active main belt asteroid, (248370) 2005 QN₁₇₃, a low-albedo object generally classified as a *C*-class asteroid, that was published by Ivanova et al. (2023a). The polarimetric data shown in this paper do not suggest that it could belong to the old *F* taxonomic class, but, based mainly on broadband images and reflectance spectra, this object was found to exhibit a dust tail which was detectable for about half a year. Modelling of dust particles based on photometric and polarimetric results suggests that large particles are concentrated around the nucleus, whereas smaller ones dominate the tail. Finally,

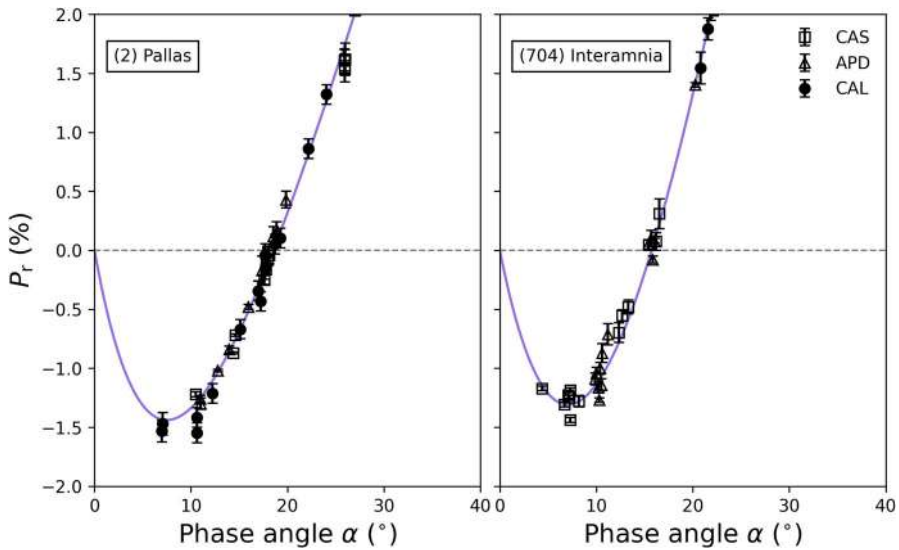


Fig. 7 Phase-polarisation curves of (2) Pallas (left panel), the largest *B* class asteroid, and (704) Interamnia (right panel), the largest asteroid belonging to the former *F* class. The best-fit curves have been computed using the exponential-linear function of Eq. (2)

Kiselev et al. (2024b) discusses polarimetric monitoring of active primitive asteroids, and further supports the idea that polarimetry can crucially contribute to taxonomic classification of asteroids.

2.3.1 Polarimetric studies of new taxonomic classes

A new taxonomic classification for a set of more than 2,000 asteroids has recently been developed by Mahlke et al. (2022). This classification is based on a new iterative method which takes into account the overall quality of input parameters coming from different sources, and reintroduces the geometric albedo amongst the data sources used for classification. One interesting result has been the definition of a new taxonomic class (named *Z* class) of asteroids characterised by very reddish reflection spectra. The existence of a peculiar object now classified as a member of the new *Z* class had been already noticed by Cellino et al. (2020). This asteroid, (269) Justitia, is known to exhibit an unusual phase-polarisation curve. In fact, the still few polarimetric measurements available for this object, suggest a fairly shallow value (around -0.6%) of P_{\min} , reached at a phase angle between 5° and 8° , whilst the inversion angle seems to occur at a phase angle between 14° and 16° , and the polarimetric slope is not very steep. If confirmed by new measurements, this behaviour is quite different with respect to that exhibited by other asteroids, including those belonging to the unusual *F* class (which share a small value of the inversion angle, but have much steeper polarimetric slopes and deeper P_{\min}). It might be possible that this is the beginning of the discovery of a new class of objects whose

spectroscopic and polarimetric properties are rare and interesting, like in the case of Barbarians.

2.4 Asteroid polarimetry at near-IR wavelengths

Very recently, Masiero et al. (2023) carried out a campaign of polarimetric measurements of six Barbarian asteroids in the near-IR *H* and *J* bands, using the Palomar 200-inch telescope. They found that the phase-polarisation curves in the near-IR change very much with respect to those obtained at visible wavelengths. Their preferred interpretation is that Barbarian surfaces consist of a mixing of a high-albedo component having high index of refraction inclusions, and a dark matrix material more similar to that of primitive, low-albedo asteroids belonging to the C taxonomic complex. According to the authors, these results are consistent with the interpretation of Barbarians as remnants of a population of primitive bodies that formed shortly after CAIs. For what concerns NEAs, which are extensively covered in Sect. 3, we mention the paper by Harris et al. (1998), which derived the sizes and thermal IR colours of (2100) Ra-Shalom and 1991 EE.

2.5 Future plans for asteroid polarimetry, and synergy with GAIA

The perspectives of the role played by polarimetric observations of the asteroids in the years to come is strictly dependent upon the availability of new dedicated instruments, both telescopes and polarimeters. So far, the role of polarimetric studies has been mostly limited by the relative lack of data, with respect to other classical techniques like imaging and spectroscopy.

The Calern Asteroid Polarimetric Survey (CAPS, Bendjoya et al. 2022) has become in recent years one of the major sources of asteroid polarimetric data (as an example, Fig. 3 shows with red symbols CAPS data). The older Topol polarimeter has been now replaced by a copy of the DiPol instrument (Piirola et al. 2021), which allows simultaneous observations in the three BVR filters. Polarimetric observations of asteroids have become routine also at larger telescopes.

It is not possible to overestimate the importance of polarimetric measurements as a useful input to complement the so-called “Gaia revolution”, namely the immense improvement in asteroid science produced by the growing wealth of astrometric, photometric, and spectroscopic data produced by the Gaia space mission of the European Space Agency (Spoto et al. 2018; Tanga et al. 2023). In particular, polarimetric data of even a relatively small number of well-measured objects will be of the highest importance for the development of a new Gaia-based asteroid taxonomy. Moreover, albedoes derived from polarimetric data will be of primary importance to calibrate the proposed relation (see Belskaya and Shevchenko 2000) between the albedo and some properties of the phase-magnitude relation, the latter being derived for thousands of objects by Gaia photometric measurements.

2.6 Conclusions

Polarimetry is an extremely useful technique to achieve a better understanding of the physical properties of asteroids, including but not limited to those orbiting in the main belt. In the past, the lack of sufficiently large datasets of polarimetric measurements has prevented or strongly delayed the exploitation of polarimetric data for important purposes, including the determination of physical parameters which are difficult to determine by means of other techniques, as in the case of the geometric albedo and the size distribution of surface regolith particles. Things are changing quickly, however, and it is reasonable to expect that in the years to come polarimetric and spectropolarimetric data will play a more important role in the physical studies of asteroids. Even in the case that the polarimetric database will not reach the size of those produced by photometry and spectroscopy, the simple availability of many more data than those we have today will be sufficient to calibrate important relations involving physical mechanisms in which the albedo and other polarimetric parameters play a fundamental role. The simple existence of classes of asteroids which can be identified based on the properties of their phase-polarisation curves ensures that the exploitation of asteroid polarimetric data is probably just at the beginning of a new era.

3 Jupiter Trojans, Centaurs, TNOs, and icy moons

Small Solar System bodies that have a perihelion close or beyond the Jupiter's orbit have rarely been observed with polarimetric techniques. The main reason is that they are faint, and even with 8-m class telescopes, it is difficult to obtain polarimetric measurements with sufficiently high signal-to-noise ratio (S/N). Another problem is that ground-based observations cover a small range of phase angles (up to $\sim 12^\circ$ for objects at the Jupiter's orbit, and up to 1.4° for trans-Neptunian objects, or TNOs), which is also difficult to model. Yet, surprisingly, the polarimetric observations of TNOs and Centaurs show a polarisation behaviour more diverse than that observed for main belt asteroids at small phase angles.

Here, we review the results of polarimetric measurements of various dynamical groups of objects, including Jupiter Trojans (Sect. 3.1), Centaurs (Sect. 3.2), TNOs (Sect. 3.3), and satellites of outer planets (Sect. 3.4, except Titan, considered in Sect. 5.8). In Sect. 3.5, we compare the polarimetric properties of these groups of objects.

3.1 Jupiter Trojans

The general definition of Trojan asteroids is based on their dynamical properties. They orbit the Sun being located in the stable L4 or L5 Lagrangian points, 60° ahead (L4) or behind (L5) the orbit of one of the major planets. The most numerous population is that of Jupiter Trojans, which includes more than 12 700 asteroids. A review of their dynamical and physical properties can be found in Bottke et al. (2023).

The first programme of polarimetric measurements of Jupiter Trojan asteroids was carried out only in 2013 (Bagnulo et al. 2016) using the FORS2 instrument (Appenzeller et al. 1998) of the ESO Very Large Telescope (VLT). Measurements of linear polarisation were obtained for six Trojans covering the phase angle range from 7 to 12°. The sample of the selected targets included Trojans with diameters 50–130 km from the L4 swarm, five of which belonging to low-albedo D-class (according to taxonomic classifications of the asteroid population). Each object was observed at 3 or 4 different phase angles in the R filter. These observations revealed negative polarisation branches having a minimum at phase angles around 8–10°. The phase-polarisation curves were found fairly similar to each other, but not identical, with P_{\min} values from -0.95% to -1.35% . The deepest negative polarisation minimum ($P_{\min} = -1.35\%$) was measured for (3548) Eurybates, the parent body of a large collisional family, and the only C-class object in the sample. The shallowest polarisation branch was observed for D-class Trojans (588) Achilles and (4543) Phoinix (Fig. 8). Up to now, all observed Trojans belong to the same L4 dynamical population.

In general, the polarisation phase curves of the observed Jupiter Trojans are rather similar to polarisation-phase curves of low albedo main belt asteroids (Belskaya et al. 2017, Sect. 2). The albedos of the Jupiter Trojans are extremely low ($\sim 0.04 - 0.05$), and their negative polarisation branch distinctly reveals the so-called “saturation effect”. This effect was found first in the laboratory (Zellner et al. 1977), and consists of a non-monotonic behaviour of P_{\min} with the albedo. For most of the albedo values, the absolute value of P_{\min} increases as the albedo decreases, but for very dark surfaces, the behaviour changes, and $|P_{\min}|$ decreases for extremely low values of albedo. Laboratory data show that the inverse correlation between the depth of negative polarisation and the albedo is valid for surfaces with albedo ≥ 0.06 , but is no longer valid for darker surfaces (Zellner et al. 1977; Shkuratov et al. 1992). This effect was observed for some dark main belt asteroids (Belskaya et al. 2005), and was found also for Jupiter Trojans (Bagnulo et al. 2016).

The reason why D-class Jupiter Trojans with similar albedo and spectral properties reveal a diverse polarisation behaviour is not understood, and a search for possible correlation of polarisation behaviours of the observed Trojans with their dynamical and surface properties did not reveal any trends (Bagnulo et al. 2016).

We note that one of the Jupiter Trojans observed in polarimetric mode, the C-class Trojan (3548) Eurybates, has been selected as a target of ongoing NASA Lucy mission (Levison et al. 2021) which will fly-by this object in 2027. In support of the space mission, Eurybates is being intensively studied by different methods. It was revealed that it has a small satellite (Noll et al. 2020). The satellite is faint and its possible contribution to the measured polarisation of Eurybates is negligible.

Further observations are needed to increase statistics and to understand the reasons of differences in the polarisation-phase curves of Trojans.

3.2 Polarimetry of Centaurs

The population of Centaurs includes objects in unstable orbits typically with a semi-major axis and perihelion in the range of 5–28 AU, i.e., between the orbit of Jupiter

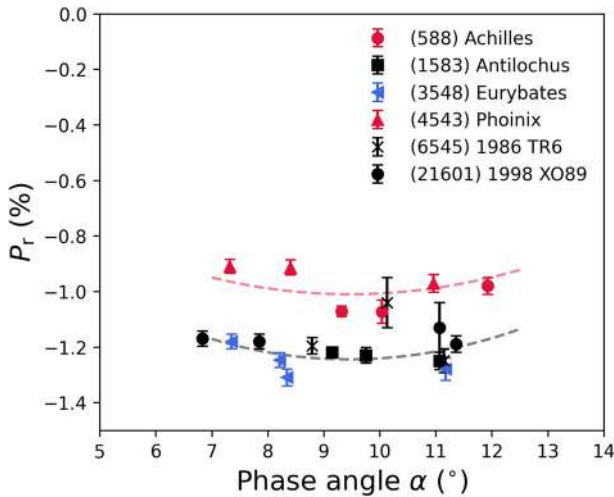


Fig. 8 Polarimetry of Jupiter Trojans

and that of Neptune. The definition of Centaurs from the dynamical point of view is ambiguous. The Minor Planet Center includes Centaurs in the same list with scattered disc trans-Neptunian objects that have high eccentricity orbits and a wide range of semi-major axes. Ground-based observations of Centaurs can be carried out at phase angles up to $\alpha \leq 7^{\circ}$.

The first polarimetric observations of the brightest Centaurs, Chiron, Chariklo, and Pholus, were obtained in 2004–2008 with the ESO VLT and the FORS instrument in the V and/or R filters. The most detailed polarisation phase dependence was measured for (2060) Chiron, one of the largest and brightest Centaurs. Observations were carried out at three apparitions in 2004 (Bagnulo et al. 2006), 2007, and 2008 (Belskaya et al. 2010). The observations in the phase angle range from 1.4 to 4.2° in 2004 revealed a pronounced branch of negative polarisation with $P_{\min} \sim -1.4\%$ at phase angles of $1.5 - 2^{\circ}$ (Bagnulo et al. 2006). Subsequent observations were aimed at determining more accurately the parameters of the polarisation minimum and to look for a possible variability. The resulting polarisation phase dependence in the phase angle range from 0.5 to 4.2° is shown in Fig. 9. All measurements are well consistent within error bars, and do not show any noticeable changes in the polarisation degree over Chiron's surface. The estimated polarisation parameters of Chiron have the following values: $P_{\min} = -1.4\%$, $\alpha_{\min} = 1.5^{\circ}$, $\alpha_{\text{inv}} \sim 7 - 9^{\circ}$ (Belskaya et al. 2010).

Since Chiron is known to exhibit sporadic cometary activity, all acquired polarimetric images were co-added and carefully checked for possible coma, but no cometary-like outburst activity was detected (Bagnulo et al. 2006).

The polarisation phase curves of two other large Centaurs (5145) Pholus and (10199) Chariklo were measured in less detail, but despite this, their diversity is well seen (Belskaya et al. 2010). The Pholus' surface is characterised by a deep negative polarisation branch with $P_{\min} = -2.1 \pm 0.2\%$, which occurs at the phase angle of

about 2.6° (Fig. 9). For Chariklo, the negative branch of polarisation degree has a depth of $\sim 1\%$ and only slightly changes in the phase angle range of $2.7 - 4.4^\circ$.

One more object, (29981) 1999 TD10, was measured in the phase angle range of $0.8 - 3.1^\circ$ by Rousselot et al. (2005). This object has an ambiguous dynamical classification with a perihelion at 12.3 au as a Centaur, but a semi-major axis of 98.7 au as a scattered disc object. The measurements revealed a negative polarisation branch with $P_{\min} \sim -1.2\%$ reached at the phase angle of $\alpha \geq 3^\circ$. A trend towards a deeper polarisation branch in R band compared to that in V band was found (Rousselot et al. 2005).

Centaurs revealed a remarkable diversity in their polarisation phase angle behaviours, although the observations covered a limited range of phase angles not exceeding 4.2° . The depth of negative polarisation varies from -1% to -2.1% and the position of minimum varies from 1.5° to $\geq 3^\circ$.

The pronounced negative polarisation at small phase angles was explained in terms of a two-component surface model consisting of dark and bright scatterers (Bagnulo et al. 2006; Belskaya et al. 2008b). The observed diversity in polarisation behaviour of Centaurs may occur due to varying amounts of icy frost on the top of their dark surfaces. It has not yet been investigated whether the ring systems discovered around Chariklo (Braga-Ribas et al. 2014) and Chiron (Ortiz et al. 2015) could influence the polarisation properties.

3.3 Polarimetry of trans-Neptunian objects

Most of the currently available polarimetric data for trans-Neptunian Objects were obtained between 2004 and 2012, for nine objects in total, again with the FORS instrument of the ESO VLT (Boehnhardt et al. 2004; Bagnulo et al. 2006, 2008; Belskaya et al. 2008a, 2012). In addition, several polarimetric measurements of the

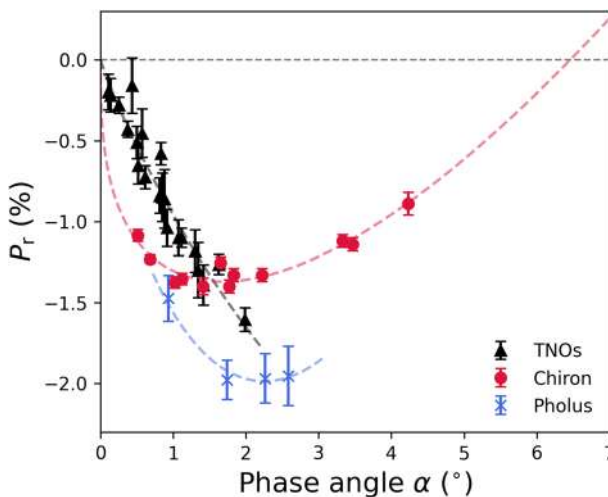


Fig. 9 Polarimetry of Centaurs (Chiron and Pholus) and TNOs (Huya, Ixion, Varuna and 1999 DE9)

Pluto-Charon system were obtained between 1972 and 1988 (Fix and Kelsey 1973; Breger and Cochran 1982; Avramchuk et al. 1992). Although ground-based observations of TNOs were made at phase angles not exceeding 2° , they revealed several very interesting features. First of all, Boehnhardt et al. (2004) found that the polarisation curve of TNO Ixion in the small range between 0 and 1.5° was much steeper than normally observed in the case of main belt asteroids, reaching $P_r \simeq -1.2$ at $\alpha \simeq 1^\circ$. Bagnulo et al. (2008) found that the larger TNOs exhibited distinctly different polarimetric behaviours compared to smaller-sized TNOs. Objects with a diameter > 1000 km show slow changes in the observed range of phase angles. For smaller TNOs, linear polarisation changes rapidly with phase angles and reaches $\sim -1\%$ at the phase angle as small as 1° (Fig. 9). Further observations of two more objects confirmed this trend (Belskaya et al. 2012). Moreover, the largest TNOs rich in methane and water ice have been found to exhibit different polarisation properties (Belskaya et al. 2012).

Polarisation-phase curves of four TNOs with diameters in the range of 310 – 670 km (Huya, Ixion, Varuna and 1999 DE9) are shown in Fig. 9. They exhibit similar polarisation phase-angle behaviour with a rapid increase (in absolute terms) of negative polarisation from almost zero up to 1.6 % when the phase angle increases to 2° . It is not possible to determine the exact position of the minimum due to the limited range of phase angles covered by the ground-based observations, but most likely, it occurs at $\alpha_{\min} \sim 2 - 3^\circ$. The largest methane-ice rich TNOs (Pluto, Eris, Makemake) and water-ice rich TNOs (Haumea, Quaoar) exhibit very slow changes in polarisation degree with phase angle with $P \simeq -0.3\%$ and $P \simeq -0.6\%$, respectively. It is interesting to note that ring systems were discovered around both above-mentioned water-ice rich TNOs Haumea (Ortiz et al. 2017) and Quaoar (Morgado et al. 2023; Pereira et al. 2023). As in the case of Centaurs, the possible influence of ring systems on polarisation properties has not yet been studied.

All published polarimetric observations on Centaurs and TNOs are available in the database of NASA Planetary Data System (Belskaya 2020).

3.4 Polarimetry of icy moons

Ground-based polarimetric observations of satellites of the distant planets, in addition to a limited phase angle range, are complicated due to their proximity to the parent planets. The observation requires very accurate measurements taking into account the illumination from the planet. One more problem is related to observations of satellite's different hemispheres at eastern and western elongations due to the synchronisation of satellite's axial and orbital rotations. Different polarisation properties of hemispheres seen at eastern and western elongations lead to the so-called longitude effect. Numerous observations are required to separate longitude dependence of polarisation degree from solar phase angle dependence (e.g., Rosenbush 2002).

At present, polarimetric measurements are available only for 14 satellites of the outer planets, which include 5 satellites of Jupiter, 5 Saturnian, and 4 Uranian satellites. Saturnian satellite Titan, which has a dense atmosphere, is considered in Sect. 5.8. The available polarimetric measurements of satellites were compiled in the

catalogue at NASA PDS (Zaitsev et al. 2020). Most of them were obtained with the telescopes up to 2.6 m in diameter. The ESO-VLT was used in 2009–2012 to study Saturn’s moon Iapetus (Ejeta et al. 2012, 2013). Observations of Uranian satellites were carried out at the 6-m BTA telescope (Afanasiev et al. 2014). A detailed review of the satellite polarimetric data was given by Rosenbush et al. (2015).

In the following, we briefly discuss the main observational features of the polarisation from largest satellites of Jupiter, Saturn, and Uranus.

3.4.1 Jovian satellites

The four large Galilean satellites of Jupiter (Io, Europa, Ganymede, and Callisto) have been observed with polarimetric techniques since the 1960s, and up to the present (see Veverka 1971b; Rosenbush et al. 2015; Kiselev et al. 2022a, 2024a). Their numerous ground-based observations covered the maximal possible range of phase angles for ground-based observations from $0.1 - 0.2^\circ$ to 11.5° . One more object, irregular satellite Himalia, was measured at three phase angles in the range of $2.3 - 9.5^\circ$ by Degewij et al. (1980).

The estimated main parameters of the negative branch of polarisation phase curves are presented in Table 1 together with the satellite’s albedos and diameters. There is a general trend for darker satellite to have deeper and wider negative branch of polarisation. Low albedo satellite Himalia revealed a deep negative polarisation, similar to what exhibited by C-type asteroids (Degewij et al. 1980).

The polarisation-phase behaviour of the moderate-albedo satellite Callisto resembles those of moderate-albedo asteroids and of the Moon. The brightest satellite Europa exhibits a branch of negative polarisation highly asymmetric about its minimum, with polarisation minimum shifted at very small phase angles. The inversion into positive branch is expected at phase angles as low as $6 - 7^\circ$. The phase curve of Ganymede is also highly asymmetric, but its shape is different from that of Europa, and the inversion angle reaches $8 - 9^\circ$ (Kiselev et al. 2024a). One more bright satellite, Io, is characterised by a shallow wide negative branch, with an inversion angle $\alpha_{inv} > 20^\circ$ (Kiselev et al. 2024a). Note that Io has exceptional surface composition coated with sulphur compounds (Trumbo et al. 2022), which is very distinct from other large moons that have icy surfaces.

The longitude variations of polarisation in the studied phase angle range can reach up to 0.8 % for Callisto (Rosenbush et al. 2002) and up to 0.2 % for Ganymede, whilst it is found to be very small for Io and Europa (Kiselev et al. 2022a, 2024a).

The wavelength dependence of negative polarisation parameters in the UBVR bands is not reliably established yet, because the differences between the measurements obtained in the various filters are within uncertainties.

Measurements at large-phase angles up to 130° of the largest Jovian satellites were obtained by the NASA’s Pioneer 10 and 11 space probes with the Galileo Photopolarimeter Radiometer. Only preliminary results of these data were reported (Martin et al. 2000) which suggested that Ganymede and Callisto have polarisation phase curves similar to that of the Moon, with $P_{max} \sim 4 - 5\%$ at $\alpha \simeq 100^\circ$. For the bright objects Io and Europa, the polarisation values are small and their uncertainties are too large to reach any conclusion.

3.4.2 Saturnian satellites

The brightest Saturnian satellites Enceladus and Rhea have rather similar negative branch of polarisation with $P_{\min} \sim -0.5\%$ at $\alpha \simeq 2^\circ$. The longitude variations of polarisation were small and not separated. For Dione, the measurements were obtained only for the darker trailing side at two phase angles. The polarisation measured at $\alpha = 2^\circ$ is $\sim -0.8\%$, which seems to indicate a deeper negative polarisation branch compared to that for Enceladus and Rhea. The above-mentioned measurements of Enceladus, Rhea, and Dione were obtained at the 2.6-m telescope of the Crimean Astrophysical Observatory in the WR spectral band (Zaitsev et al. 2015a, b; Rosenbush et al. 2015). The previous observations on Rhea and Dione carried out at the 1.56-m Catalina telescope (Bowell and Zellner 1974) generally agreed with the more recent results. Due to large instrumental polarisation, the observations of Rhea, Dione, and Tethys obtained at the 2-m Rozhen telescope (Kulyk 2012) have a large scatter and are not useful (Rosenbush et al. 2015).

The first polarimetric observations of Iapetus were obtained with the 1.56-m Catalina telescope (Zellner 1972), and revealed different polarisation of the leading and trailing hemispheres, consistently with the albedo dichotomy of this satellite. Further observations were made by Rosenbush et al. (2015, and references therein) at the Crimean Astrophysical Observatory, and by Ejeta et al. (2012), Ejeta et al. (2013) using the FORS2 instrument at ESO VLT. These data agree within uncertainties, and demonstrate a deep negative branch of polarisation for the dark leading side and highly asymmetric branch for bright trailing side (see Table 1). Spectropolarimetric measurements of the bright side of Iapetus shown a small spectral dependence in the 430-900 nm wavelength range (Ejeta et al. 2012).

3.4.3 Uranian satellites

Observations of four large Uranian satellites, Ariel, Umbriel, Titania, and Oberon, were carried out at the 6-m BTA telescope, in the V band, within the phase angle range of $0.1 - 2.4^\circ$ (Afanasiev et al. 2014). These observations covered the maximum possible phase angle range for ground-based observations of Uranian moons. All measured satellites revealed deep negative branches of polarisation with P_{\min} from -1.1% to -1.7% .

The position of the polarisation minimum is well determined for Ariel, and occurs at the phase angle as small as 1° . For Titania and Oberon, the minima occur at phase angles of $1.4 - 1.8^\circ$. For Umbriel, the darkest satellite of this group, the minimum occurs most likely at 2.4° , or even at a larger phase angle (not covered by the observations). There is a trend of shifting polarisation minima towards smaller phase angles as the albedo increases (Afanasiev et al. 2014).

3.5 Comparison of the polarimetric properties

Polarimetric observations were obtained mainly for the largest objects orbiting at Jupiter's heliocentric distance and beyond. Although these data covered limited phase angles close to opposition, they revealed some very interesting features. The

main finding is the surprising diversity in the polarisation behaviour at small phase angles.

A wide negative polarisation branch is observed for Jupiter's Trojans, the irregular dark Jovian satellite Himalia, and the dark carbon-rich leading hemisphere of Calisto. The polarisation minima of these objects occur at phase angles of $7 - 10^\circ$, and reach P_{\min} from -0.85% to -1.6% resembling the phase-polarisation curves of low-albedo asteroids and of the Moon. All other distant objects measured with polarimetry reveal a shift of polarisation minima towards smaller phase angles, with minimum angle $\alpha_{\min} \leq 5^\circ$.

The deep negative polarisation branch near opposition can be explained by the coherent back-scattering mechanism, which is effective for high-albedo surfaces (e.g., Muinonen et al. 2012, see also Sect. 6). According to theoretical modelling, the photometric opposition effect should be accompanied by a polarisation opposition effect of the same angular width (e.g., Mishchenko and Dlugach 1993). The pronounced negative polarisation measured at $\alpha \leq 1^\circ$ for the high-albedo Galilean satellites of Jupiter (Rosenbush et al. 1997) provided observational confirmation of the existence of a polarisation opposition effect for surfaces of Solar System bodies. The shape of the polarisation effect due to coherent back-scattering has long been the subject of debate. The question was whether the effect manifests itself as a sharp minimum of negative polarisation at small phase angles, superimposed on a regular wide negative polarisation branch (Rosenbush et al. 1997, 2015), or as a very asymmetric shape of the negative polarisation branch with P_{\min} shifted towards small phase angles. Recent detailed observations of Europa (Kiselev et al. 2022a) gave a definitive answer to this question. They did not confirm a bimodal phase-angle dependence of Europa, and revealed that its polarisation phase curve has a highly asymmetric shape with a minimum $P_{\min} = -0.3\%$ at sub-degree phase angle and an inversion angle at $6 - 7^\circ$ (Kiselev et al. 2022a).

An asymmetric shape of polarisation phase curves with a shift of α_{\min} towards small phase angles is inherent not only to bright distant objects, but also to moderate and low-albedo objects, such as Centaurs Chiron and Pholus, which have albedos of 0.16 and 0.07, respectively (Belskaya et al. 2010). These objects, as well as the observed moderate-albedo TNOs with diameters of less than 700 km, show a deep polarisation branch at small phase angles, reaching -1.5 to -2% at $\alpha \simeq 1.5 - 2^\circ$. The observed Uranian satellites have similar polarisation properties at small phase angles. Such polarisation phase angle behaviour can be reproduced by assuming two-component surface media consistent of dark and bright scatterers (e.g., Bagnulo et al. 2006). Laboratory measurements have shown that a mixture of two fine powders of different albedos sharply enhances the negative polarisation (Shkuratov 1987; Spadaccia et al. 2022). Moreover, in the negative polarisation branch, the mixing effect was found to dominate over contribution of particle size and porosity effects (Spadaccia et al. 2022). Thus, the mixture of various amounts of ices and carbon-rich dust on surfaces of TNOs, Centaurs, and satellites may be responsible for the observed diversity of their polarisation phase behaviours.

The dependence of the polarisation parameters of distant objects on albedo is rather weak. Figure 10 shows the dependence of P_{\min} on albedo for all objects considered in this Section. Note that for TNOs, we plotted the *measured* maximum of

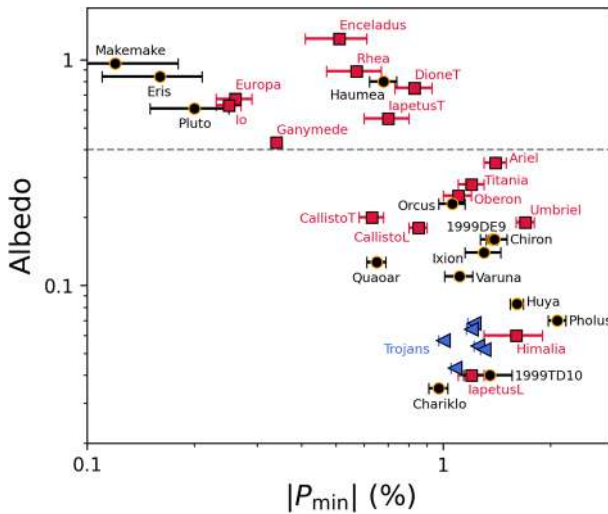


Fig. 10 Albedo dependence of polarisation minimum for distant objects. Trojans are shown by blue triangles

the absolute value of polarisation, $|P_{\min}|$, which may be smaller than the *actual* value of $|P_{\min}|$. The polarisation minima of objects with albedo > 0.4 vary from -0.2% to -0.8% . Different depths of negative polarisation were measured for methane-ice and water-ice rich TNOs despite their similar albedo (Belskaya et al. 2008c). The polarisation parameters of the icy Uranian satellites differ significantly from those of the icy Jovian and Saturnian satellites. For dark objects with albedo < 0.08 , an opposite trend is observed in the albedo- P_{\min} relationship, due to the saturation effect. All this demonstrates that, unlike for asteroids, albedo is not the main factor responsible for the polarimetric properties.

4 Comets

Comets, conglomerates of dust and ice particles, are one of the least-altered building blocks of planetesimals left over from the Solar System formation epoch. As comets travel towards the inner Solar System, ice particles sublimate and drag dust out, causing cometary activity. The activity is determined by the intrinsic properties of the nuclei that result from the nature of the environment to which individual comets have been exposed since formation. Therefore, comets provide us with an easy way to relate observations to early environmental conditions of our Solar System.

Sunlight incident on a comet is reflected either by its nucleus or by its coma (with a typical albedo of $\sim 4\%$ and $\sim 10\%$, respectively; Lamy et al. 2004; Kolokolova et al. 2004) and is observed as scattered light in the optical and near-infrared spectral domains (mostly $\sim 0.4 - 2.5\ \mu\text{m}$). This scattered light has been studied using a variety of techniques, depending on the properties of the electromagnetic field of interest, and this section focuses exclusively on linear polarimetric aspects of comets.

A key benefit of polarimetry is the ability to provide oscillatory information on the light, whose direction and magnitude are determined by the characteristics of the scattering medium. Comets can be theoretically modelled either assuming single scattering (by dust or gas particles from tails and comae) or multiple scattering (by nuclei). We will devote most of our attention to the first environment, specifically the scattering properties of dust particles forming comae and tails.

Since Arago (1820) introduced astronomical polarimetry, this technique has been used widely to explore the dust environments of comets. A comprehensive summary of polarimetric research conducted over 150 years can be found in the chapter on comets by Kiselev et al. (2015) in the book *Polarimetry of Stars and Planetary Systems* (Kolokolova et al. 2015). NASA Planetary Data System (PDS) Small Body Node² (Kiselev et al. 2017) archives data on ~ 65 comets from 1940 to 2017 (mostly to early 2010). More than 60 papers have been published on comet polarimetry since then, whilst in situ space missions as well as laboratory experiments and upgraded numerical modelling techniques have greatly advanced our understanding of comets. An upcoming European F-class mission, *Comet Interceptor* (Jones et al. 2024), will incorporate a polarimeter (Entire Visible Sky camera, EnVisS; Da Deppo et al. 2021) onboard to map and examine the entire coma environment of a dynamically new comet from the Oort cloud; hence, it is timely to revisit existing polarimetric observations of comets, in conjunction with new findings. The following subsections will present polarimetric observations (Sect. 4.2), discuss current interpretations (Sect. 4.3), and raise open questions that require independent evaluation (Sect. 4.4). For an overview of previous work in the field, we refer the readers to Kiselev et al. (2015).

4.1 Methodology

As with other Solar System bodies discussed in this review, the scattering plane defines a geometrical basis in comet polarimetry. Appendix A provides detailed descriptions of the observations, calibrations, and extraction of intrinsic polarimetric parameters.

Along with the fundamental differences in comets resulting from long-term differences in the environment during their formation and evolution, cometary activity and their ejecta properties vary over a relatively short, testable timescale as they orbit the Sun. This secular evolution of comets can be measured by polarisation P_r , which depends on the observation geometry, particularly the phase angle α (angle of the Sun–comet–Earth), and often on its location in the cometary coma. Polarisation also varies with wavelengths, reflecting the wavelength dependence on the dust's complex refractive index.

Each method of polarimetric measurement is suitable for studying a certain polarimetric dependence. Several widely used methodologies are listed here, along with their benefits and drawbacks. The most widely used method of polarimetry is *aperture polarimetry* as it integrates all the signals over a finite aperture, which alleviates inherent brightness limitations in polarimetry. P_r of comets are often

² <https://pdssbn.astro.umd.edu/holdings/ear-c-compil-5-db-comet-polarimetry-v1.0/dataset.shtml>

measured at a particular or restricted range of α (e.g., Fig. 11), and their collective dependence on α is characterised as the so-called polarisation-phase curves. This method is useful for quickly comparing bulk properties between different comets based on the curve shape, but it loses spatial information due to the averaging of signals across the coma. This limitation can be solved with *imaging polarimetry* by measuring local P_r values in the coma and mapping their variations as dust is ejected from the nucleus, correlating the observables to the distribution of distinct dust populations. This method provides visually compelling information about dust environments, whilst a special care must be taken to ensure that photocentres are aligned properly in building P_r maps to avoid any misleading results (Sects. 4.2.3 and 4.4). Finally, *spectropolarimetry* allows the measurement of the wavelength dependence of P_r , allowing simultaneous measurements of P_r at a given wavelength and spectral gradients of P_r and intensity. This observing technique has the advantage of providing multiple characteristics of the scattered light simultaneously, but it should be kept in mind that, due to the nature of the currently available spectropolarimeters, it is not efficient at providing spatial information.

4.2 Main observational results in linear polarisation

This section presents the main observations obtained by each observing method, focussing on the recent publications made since the review of Kiselev et al. (2015).

4.2.1 Polarisation-phase curve

Cometary dust particles with low albedo and porous, irregular aggregate structure exhibit a bell-shaped polarisation dependence on phase angle $P_r(\alpha)$, as shown in Fig. 11, whose shape can be depicted by six parameters (Fig. 2): minimum degree of polarisation P_{\min} , and its phase angle α_{\min} at $\approx 10 - 12^\circ$ marking the geometry of most negative polarisation, the so-called inversion angle α_{inv} at $\sim 22^\circ$ where P_r changes its sign from negative to positive and, thus, $P_r = 0\%$, the slope h over $\pm 5^\circ$ therearound, maximum degree of polarisation P_{\max} and its phase angle α_{\max} at $\sim 95^\circ$. Phases smaller or larger than α_{inv} are referred to as the negative polarisation-branch (NPB) and positive polarisation-branch (PPB), respectively. The polarisation-phase curve of a single comet represents the ensemble properties of the ejected dust particles averaged throughout its apparition, as detailed makeups of cometary dust at a given phase are likely to evolve as comets orbit the Sun.

We used an empirical trigonometric function (Lumme and Muinonen 1993) to parameterise polarisation-phase curves of cometary dust (Eq. 7), where A , B , C , and α_{inv} are wavelength-dependent parameters (Penttilä et al. 2005). A polarisation-phase curve is commonly created by combining observations of different comets conducted over a certain α range due to their limited observability from the Earth. For this reason, the relative excess of P_r at a given α compared to the average (interpolated) trend value of all available comets, fitted by Eq. (7), has been often used to quickly grasp a comet's relative dust environment.

Figure 11 illustrates dust polarisation-phase curves in the R (0.62–0.73 μm) and K (2.00–2.39 μm) filter regions, which were chosen for their large number of available

data points as representative optical and near-infrared bands. There is relatively less contamination from gas molecules in the R filter region than in the shorter wavelengths (e.g., C_2 at $\lambda < 0.6 \mu\text{m}$; Meech and Svoren 2004). However, as NH_2 would affect the R band significantly (Kiselev et al. 2004; Kwon et al. 2017), we here only considered 1) datasets acquired with narrow-to-intermediate continuum filters (full width half-maximum, FWHM, $\leq 0.05 \mu\text{m}$), 2) datasets showing a strong dust influence over gas, and/or 3) datasets obtained outside of the inner Solar System ($r_H \gtrsim 2 \text{ au}$) to minimise the gas influence. In the K-filter wavelength, thermal emission from dust possibly lowers intrinsic P_r signals by up to $\sim 30\%$ when observations are made at $r_H \lesssim 1 \text{ au}$ (Oishi et al. 1978a, b). Hence, we only took into account the datasets obtained outside of 1 au of the Sun.

There is a general similarity in the polarisation-phase curves of dust from comets of different dynamical groups, whose best-fit parameters are $A = 0.318 \pm 0.001$, $B = 0.742 \pm 0.003$, $C = 0.297 \pm 0.006$, and $\alpha_{\text{inv}} = 21.36^\circ \pm 0.03^\circ$ in the R filter and $A = 0.314 \pm 0.003$, $B = 0.968 \pm 0.033$, $C = 3.271 \pm 0.022$, and $\alpha_{\text{inv}} = 13.36^\circ \pm 0.26^\circ$ in the K filter. In both bands, 1P/Halley is observed throughout a wide α range, defining the overall shape of the curves. C/1995 O1 (Hale-Bopp) in the 1997 apparition still holds the throne in the R filter region (Fig. 11a) for its significantly higher P_r values compared to typical Solar System comets over $\alpha \sim 0\text{--}40^\circ$ (Hadamcik and Lvasseur-Regourd 2003a). The first active interstellar comet 2I/Borisov shows comparably high P_r at similar geometry (Bagnulo et al. 2021). Disintegrating comet C/2019 Y4 (ATLAS) appears to have similarly high P_r (Zubko et al. 2020). 2P/Encke at large phases exhibits abnormally high P_r , with its derived P_{max} being nearly 10% higher than most comets (Jockers et al. 2005; Kwon et al. 2018). With its large variation in P_r with aperture size, 2P/Encke at high α measures at its highest P_r near the nucleus and drops to the level of diatomic gas molecules at distant radial distances (Kiselev et al. 2015 and references therein). In contrast, 21P/Giacobini-Zinner consistently has a lower P_r than comets in similar phases (Chornaya et al. 2020). It appears that the K-domain curve exhibits a relatively shallower NPB and higher P_{max} , allowing C/1995 O1 (Hale-Bopp) to deviate from the average trend less than it shows at shorter wavelengths. However, the small number of data points in small and large α ($\lesssim 20^\circ$ and $\gtrsim 80^\circ$) and large scatter in the measurements require more observations for accurate estimation of the phase dependence in this wavelength.

Whilst comets as a whole exhibit broadly similar polarisation-phase patterns, some discernible differences are present, even after accounting for the instrumentation and aperture sizes used in different observations. We will discuss the possible causes of this dispersion of comet polarisation in Sect. 4.3.

4.2.2 Polarisation spectra

Spectropolarimetry or (quasi-)simultaneous multi-band aperture polarimetry measurements provide spectral gradients of polarisation $P_r(\lambda)$. Here, we introduce the so-called ‘polarimetric colour (PC)’ in units of % per micrometres (%pt. per μm), which is expressed as

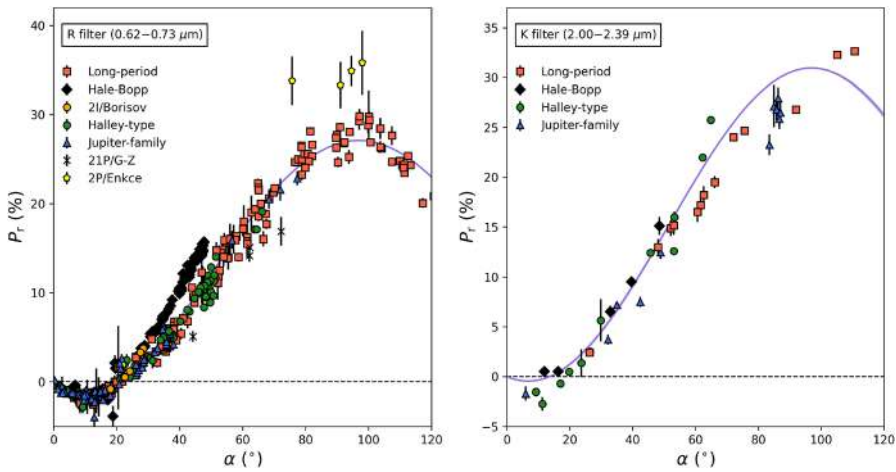


Fig. 11 Polarisation-phase curve of cometary dust in the R (left) and K (right) filter regions. The solid lines and coloured areas represent the trigonometric fit lines (Eq. (7)) with their 1σ uncertainties. Most data sets were from NASA/PDS comet polarimetry archives published in 2006 (Kiselev et al. 2005) and 2017 (Kiselev et al. 2017), but new measurements omitted or made after 2017 have also been included: 1P/Halley (Brooke et al. 1987), 2P/Encke (Kwon et al. 2018), 29P/Schwassmann-Wachmann (Kochergin et al. 2021), 67P/Churyumov-Gerasimenko (Stinson et al. 2016; Rosenbush et al. 2017; Kwon et al. 2022a), 78P/Gehrels (Roy Choudhury et al. 2014), 252P/LINEAR (Kwon et al. 2019), 290P/Jager (Roy Choudhury et al. 2015; Deb Roy et al. 2015b), C/2001 Q4 (NEAT) (Ganesh et al. 2009), C/2007 N3 (Lulin) (Woodward et al. 2011; Roy Choudhury et al. 2015), C/2011 L4 (PANSTARRS) (Roy Choudhury et al. 2015), C/2012 L2 (LINEAR) (Deb Roy et al. 2015a), C/2013 US10 (Catalina) (Kwon et al. 2017), C/2013 V1 (Boattini) (Deb Roy et al. 2015b), C/2017 K2 (PANSTARRS) (Kochergin et al. 2023; Kwon et al. 2024), and 2I/Borisov (Bagnulo et al. 2021)

$$PC \equiv \frac{|\Delta P_r|}{\Delta \lambda} = \frac{|P_r(\lambda_2) - P_r(\lambda_1)|}{\lambda_2 - \lambda_1}, \quad (8)$$

where $P_r(\lambda_x)$ is the polarisation in % measured at wavelength λ in micrometres ($\lambda_2 > \lambda_1$). Regardless of its sign, PC is labelled as positive (red PC) or negative (blue PC) when the absolute P_r increases or decreases with wavelength, respectively.

PC of cometary dust varies with α , shown as a colour gradient in Fig. 12. The measurements in the figure were obtained from the NASA/PDS comet polarimetry archives (Kiselev et al. 2005, 2017) as well as literature published afterwards, whose references are provided in the figure caption. Data selection was performed according to the same criteria as for polarisation-phase curves (Fig. 11), to minimise the depolarising effects of gas molecules below $0.7 \mu\text{m}$. We used K-band polarisation degrees of C/1975 V1 (West) corrected for thermal emission instead of the observed values (Fig. 3 in Oishi et al. 1978a).

Cometary dust polarisation slopes change to naught as the phase approaches the inversion angle in the NPB and turn back to red as the phase keeps increasing in the PPB, similar to the trend in asteroids (e.g., Bagnulo et al. 2015; Kwon et al. 2023). In general, cometary dust exhibits red, broadly linear PC in the visible (up to $\sim 0.9 \mu\text{m}$, equivalent to the I-filter wavelength) in the PPB. At wavelengths longward of $\sim 1 \mu\text{m}$, the red PC flattens or for some comets, which reverses its slope at $\sim 1.6 \mu\text{m}$

(equivalent to the J-filter wavelength) in the PPB as shown in C/1995 O1 (Hale-Bopp) (Brooke et al. 1987; Kikuchi et al. 1987; Hasegawa et al. 1997). This downturn can be attributed to external factors, such as thermal emission in the K band (at $\sim 2.2 \mu\text{m}$) when comets approach the Sun to $\lesssim 1$ au (e.g., Oishi et al. 1978a), and/or reflect dust's intrinsic properties involving the packing density, causing multiple scattering and thus depolarisation at longer wavelengths (Kolokolova and Kimura 2010). In the latter case, individual comets may experience slope inversion at different wavelengths, whose implications on dust particle properties are discussed in Sect. 4.3. In addition to typical comets having a largely similar PC trend and its dependence on α , there are some comets with neutral (or grey) PC in comparison to the expected values at the given phase, particularly 2P/Encke (Kwon et al. 2018), or comets with abnormal blue PC in the PPB, such as fragments of 73P/Schwassmann-Wachmann 3 and 21P/Giacobini-Zinner (Fig. 22.5 in Kiselev et al. (2015) and references therein).

4.2.3 Polarisation mapping

Dust particles in the coma interact with external forces such as gas drag force from sublimated ice, solar radiation pressure, and solar gravity (Fulle 2004; Agarwal et al. 2024), drawing a unique trajectory based on their intrinsic properties. Imaging polarimetry allows us to observe dust moving away from the nucleus, with its observed level of polarimetric homogeneity of the coma providing insight into the dust environment on the nucleus surface as well as the ensemble properties of dust ejecta.

Approximately three dozen comets have been observed using imaging polarimetry. Some active comets show anisotropic coma features with different P_r from the background coma, such as jets, spirals, fans, and circumnucleus halos (e.g., Renard et al. 1996; Hadamcik and Levasseur-Regourd 2003b). A prime example is C/1995 O1 (Hale-Bopp), which displayed all the above coma features due to its all-time high activity throughout the apparition (Jones and Gehrz 2000; Hadamcik and Levasseur-Regourd 2003a). Such variations in P_r have been discussed in relation to colour to suggest dust properties are sorted along the tail of comets (Borisov et al. 2015; Roy Choudhury et al. 2015; Rosenbush et al. 2017; Ivanova et al. 2017; Kiselev et al. 2020). Meanwhile, comets occasionally lack distinctive polarimetric features, allowing one characteristic value to describe their polarimetric state. The first active interstellar comet 2I/Borisov, whose activity properties are consistent with Solar System comets (Opitom et al. 2019; Guzik et al. 2020), has a homogeneous coma in its dust continuum P_r (Bagnulo et al. 2021). Polarimetric maps of hyperactive Oort-cloud comet C/2017 K2 also show a homogeneous coma over a wide range of its inbound legs (Zhang et al. 2022; Kwon et al. 2024). Likewise, comet 67P/Churyumov-Gerasimenko has shown constant polarisation degrees in the dust coma region (Kwon et al. 2022a; Gray et al. 2024a), though a discrepancy between research groups needs to be verified (Sect. 4.4). Such spatial-invariant polarisation degrees in the coma can be explained by the ejection of highly mobile dust particles (either due to their small size or equivalently high porosity), which implies that the

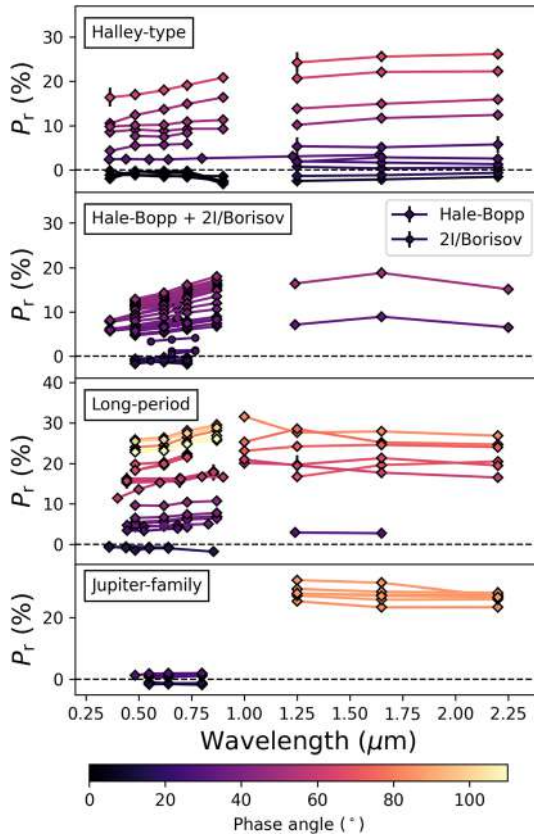


Fig. 12 Spectral gradient of polarisation degree of coma dust particles coloured in a gradient of phase angle. Measurements of Halley-type comets include 1P/Halley (Brooke et al. 1987; Kikuchi et al. 1987) and 109P/Swift-Tuttle (Kikuchi 2006). Measurements of C/1995 O1 (Hale-Bopp) came from Hasegawa et al. (1997), Kikuchi (2006), whilst 2I/Borisov data were from Bagnulo et al. (2021). Measurements of Long-period comets include C/1975 V1 (West) (Oishi et al. 1978a), C/1985 R1 (Hartley-Good) (Brooke et al. 1987), C/1987 P1 (Bradfield) (Kikuchi et al. 1989), C/1990 K1 (Levy) (Rosenbush et al. 1994), C/1996 B2 (Hyakutake) (Kikuchi 2006), C/2000 WM1 (LINEAR) (Joshi et al. 2003; Jockers et al. Unpublished), C/2009 P1 (Garradd) (Ivanova et al. 2017), C/2013 R1 (Lovejoy) (Borisov et al. 2015), and C/2020 T2 (Palomar) (Kwon et al. 2022b). Measurements of Jupiter-family comets include 22P/Kopff (Myers 1985; Chernova et al. 1993) and 252P/LINEAR (Kwon et al. 2019)

nucleus surface (or at least the source region) is relatively primitive (Kolokolova et al. 2007; Kwon et al. 2021; Bagnulo et al. 2021).

4.2.4 Polarisation by gas molecules

As the nucleus releases complex molecules, they interact with solar photons and become photo-dissociated. The photo-dissociated products, generally known as secondary or daughter molecules (e.g., C_2 , NH_2 , and CN ; Feldman et al. 2004), produce emission features in the optical domain, particularly foresting at wavelengths

shorter than $0.65 \mu\text{m}$, where most comet studies have been conducted because of its high S/N (Swamy 2010).

Gas and dust coma species exhibit markedly different polarisation-phase curves (Öhman 1941; Le Borgne and Crovisier 1987). The major gas species that contribute to the observed flux in the optical are the Swan system ($d^3\Pi - a^3\Pi$) for C_2 at $\sim 0.51 \mu\text{m}$ (in the V filter), NH_2 ($\tilde{A}_2 A_1 - \tilde{X}_2 B_1$) over $0.56\text{--}0.74 \mu\text{m}$ (in the R filter), and CN-red band ($A^2\Pi - X^2\Sigma^+$) at ~ 0.80 and $0.92 \mu\text{m}$ (in the I filter). The polarisation-phase curve of excitation-induced fluorescence anisotropy (or fluorescence polarisation) is similar to Rayleigh scattering as

$$P_{\text{gas}} = \frac{p_{\text{max}} \sin^2(\alpha)}{1 + p_{\text{max}} \cos^2(\alpha)}, \quad (9)$$

scaled by p_{max} , the maximum polarisation value at $\alpha = 90^\circ$. In the above list of optically dominant molecules, C_2 and C_3 are the species whose polarisation-phase curves fairly follow the curve with a theoretical p_{max} value of $\approx 7.7\%$ (Mrozowski 1936). Figure 13 illustrates the P_r distribution of gas molecules as a function of α , overlaid with a theoretical phase curve for diatomic molecules (Feofilov 1961). There appears to be significant dispersion in the P_r values of the NH_2 α and CN-red bands with respect to the theoretical curve (Rosenbush et al. 2002; Kwon et al. 2018), with each transition displaying distinct P_r values depending on the type of transition involved (i.e., P and R branches induced by fluorescent excitation of $\Delta J = \pm 1$, respectively, and Q branch induced by resonant transitions of $\Delta J = 0$, where J denotes a rotational quantum number; Feofilov 1961; Le Borgne and Crovisier 1987).

Gas contamination might have negligible effects on observed signals in dust-rich comets and those made around nuclei (e.g., Zubko et al. 2020; Zheltobryukhov et al. 2020). However, when it comes to observations of active comets with fresh surfaces having relatively abundant ice particles near the surface layers as *Comet Interceptor* mission aims to observe near perihelion (i.e., at large α), the leakage correction becomes vital as gas flux possibly accounts for up to a few tens of percent of observed signals at moderate distances from the nucleus (e.g., Kwon et al. 2017; Kiselev et al. 2020).

4.2.5 Polarisation by comet nuclei

There has been evidence over the past decade that comet nuclei and carbon-rich primitive asteroids are not distinct populations but rather a continuum. The European Space Agency's *Rosetta* spacecraft on comet 67P/Churyumov-Gerasimenko detected a clear band of N–H absorption at $3.1 \mu\text{m}$ (Poch et al. 2020) and a forest of C–H bands at $\sim 3.4 \mu\text{m}$ on its surface (Raponi et al. 2020). Those bands have also been observed for several low-albedo asteroids, including (1) Ceres (De Sanctis et al. 2019; Raponi et al. 2019) and Jupiter Trojans (Brown 2016). The observations strongly suggest that similar ingredients might have been available during the accretion phases, and hence, that their origins overlapped to some degree. Furthermore, the *James Webb Space Telescope* detected water vapour on 238P/

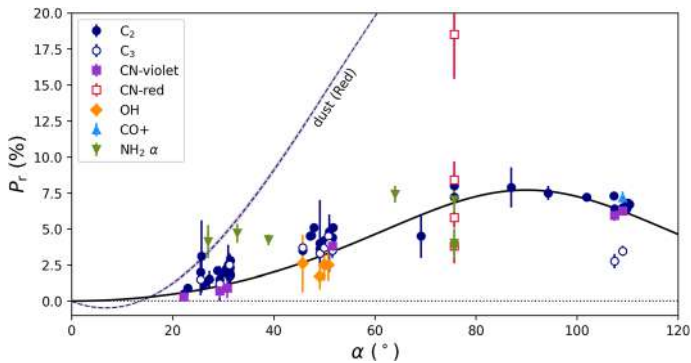


Fig. 13 Phase-angle dependence of the polarisation degree of gas molecules dominant in the optical wavelength. Polarisation-phase curves of cometary dust in the R domain (Fig. 11a) and of theoretically predicted diatomic molecules (Mrozowski 1936; Feofilov 1961) are overlaid for comparison. The following measurements were used in this plot: C_2 of 1P/Halley (Le Borgne et al. 1987a, b; Chernova et al. 1993), 2P/Encke (Kwon et al. 2018), 23P/Brorsen-Metcalf, 27P/Crommelin, 67P/Churyumov-Gerasimenko (Chernova et al. 1993), C/1985 R1 (Hartley-Good) (Le Borgne et al. 1987b), C/1988 A1 (Liller) (Chernova et al. 1993), and C/1989 X1 (Austin) (Joshi et al. 1992; Chernova et al. 1993; Kikuchi 2006); CN of 1P/Halley (Le Borgne et al. 1987b; Chernova et al. 1993), C/1989 X1 (Austin) (Joshi et al. 1992), and 2P/Encke (Kwon et al. 2018); C_3 of 1P/Halley (Le Borgne et al. 1987a), C/1985 R1 (Hartley-Good) (Le Borgne et al. 1987b), and C/1989 X1 (Austin) (Joshi et al. 1992); OH of 1P/Halley (Le Borgne et al. 1987a); CO^+ of C/1989 X1 (Austin) (Joshi et al. 1992); and $NH_2 \alpha$ bands of 2P/Encke (Kwon et al. 2018) and C/2001 A2 (LINEAR) (Rosenbush et al. 2002)

Read, a main belt comet that displays comet-like dust ejection activity but in asteroidal orbits, supporting today's widespread presence of volatile similar to comets (Kelley et al. 2023).

Comet nuclei scatter in the same way as asteroids' regolith. However, observing comet nuclei with polarimetry is often challenging, since they are almost always surrounded by diffuse, optically sensitive coma dust, and their signal rapidly dims as comets get further from the Sun. There have been some polarimetric measurements of primitive small bodies that indicate an affinity between their dust and that found on comets: the nuclei of comet 2P/Encke and main belt comet 133P/Elst-Pizarro (Bagnulo et al. 2010) share a similar polarisation-phase curve with each other and also with those of F or B asteroids, whose thermal properties well match with the presence of abundant ice mixed with fine-grained dust (e.g., Jiang et al. 2023), in both the NPB (Belskaya et al. 2005; Cellino et al. 2018; Kwon et al. 2023) and the PPB (Hadamcik et al. 2023). Further polarimetric observations of comet nuclei are required for a systematic quantitative analysis of the light-scattering characteristics of primitive small bodies.

4.3 Insights provided by comet polarimetry

Measurements of the polarimetric behaviour of cometary dust can be related to the particles' microscale physical makeups and compositions. The following sections summarise three key insights gained from polarimetry into comet evolution.

4.3.1 Phase-angle dependence of linear polarisation

Although dust ejected by different comet populations exhibits similar polarisation-phase curves in a broad sense (Fig. 11), some comets have large variations in P_r with aperture size (radial P_r gradients). This prevents one characteristic P_r value from describing their dust coma environment. Kolokolova et al. (2007) showed a correlation between the intensity of the silicate emission bands at thermal infrared (an emission band plateau at $\sim 10 \mu\text{m}$) and the perihelion distance of comets. Based on this result, the authors proposed that dust distribution across the coma, primarily determined by dust mobility related to its porosity, would contribute to the aperture-size dependence of P_r values in cometary dust. Considering that dust of high porosity can explain prominent 10- μm silicate emission (Wooden 2002), Kolokolova et al. (2007) found that comets orbiting the Sun closer and for longer times that show relatively low maximum P_r likely accommodate lower porosity, more consolidated coma dust, and thus tend to show weaker silicate features. Kwon et al. (2021) elaborated on this idea by showing that relative P_r excesses from the average trend line in the K band (e.g., Fig. 11) would effectively distinguish such dust structural differences.

Dust having large light-scattering efficiencies (due to higher porosity and/or small size) is more susceptible to solar radiation pressure pushing them away from the Sun (Burns et al. 1979; Fulle 2004). A difference in dust mobility leads dust to be sorted across a coma, affecting local dust-to-gas flux ratios. As a consequence, polarimetry covering $>10^3$ km from the photocentre of comets would be influenced by relatively low (high) contamination by depolarising gas molecules and characterised by high (low) porosity dust. The dichotomy in dust environments would be further linked to the classification of comets as Type I or Type II (Gehrz and Ney 1992): a relatively steep P_r radial dependence is observed in Type I comets due to the dominance of low-porosity dust particles (i.e., higher gas contamination impacts), whereas Type II comets exhibit a relatively constant P_r across the coma due to the high-porosity and thus highly mobile dust particles. Accordingly, Type I and Type II comets are diagnosed as gas-rich and dust-rich in optical wavelengths (Swamy 2010).

It is not always true that a higher P_r corresponds to a smaller/higher-porosity coma dust. For instance, coma dust particles from C/1995 O1 (Hale-Bopp) and 2P/Encke both show significant P_r excess compared to other comets' coma dust particles at similar geometries (Fig. 11a). The 2P/Encke dust environment, however, shows rather opposite characteristics to C/1995 O1 (Hale-Bopp), with decimetre-sized chunks dominating the inner coma region and negligible 10- μm silicate emission features (Gehrz et al. 1989; Kelley et al. 2006; Kwon et al. 2018; Kiselev et al. 2020). These low-albedo large dust chunks ($\gtrsim 100 \mu\text{m}$ in size) display optical properties more similar to comet nuclei than diffuse dust particles and are characterised by high P_r values on account of enhanced single surface scattering (Hadamcik and Levasseur-Regourd 2009).

Besides the physical aspects, dust may also have various compositions, such as an abundance of carbon-chain molecules or silicates (A'Hearn et al. 1995; Hanner and Bradley 2004). Primary elements of cometary dust are silicates (mostly olivine and

pyroxene with varying Mg and Fe ratios), carbonaceous materials, sulphides, and ice (Levasseur-Regourd et al. 2018). Each material has a different total absorptivity of distinct imaginary parts m_i of the complex refractive index m and thus affects the observed polarimetric properties (Kolokolova and Jockers 1997; Gustafson and Kolokolova 1999; Zubko et al. 2016). If the observed P_r distributions of dust from different comets purely result from their compositional diversity, transparent (smaller m_i) particles like water ice and silicates enhance multiple scattering, causing the angles of scattered light to be randomised (depolarisation). In contrast, absorbing (larger m_i) particles like carbonaceous materials increase P_r by suppressing multiple scattering and enhancing single scattering at the surface. Water ice embedded in dust particles has yet to be detected directly by comet polarimetry, but indirect evidence of ice sublimation has been proposed based on changes in P_r with cometocentric distance (Jones et al. 2008; Rosenbush et al. 2017).

It must be noted that the polarisation-phase curve alone cannot pinpoint a unique solution to dust nature. Even though it is possible to reproduce measured P_r at a certain α quite easily by adjusting only one aspect of dust (e.g., varying compositions with fixed physical properties or vice versa), often multiple solutions exist that can explain the observations. Finding a scenario compatible with polarimetric results as well as non-polarimetric observations (e.g., albedo or dust colour) can alleviate the degeneration.

4.3.2 Wavelength dependence of linear polarisation

Polarisation provides the most sensitive information about scattering media over a dust scale with sizes similar to or several times the wavelength of light. The widely accepted structure of cometary dust — hierarchical structure made up of different scales of dust clusters (Levasseur-Regourd et al. 2018; Güttler et al. 2019)—enables polarisation in optical and near-infrared wavelengths to examine different scales of dust units likely having different properties. Near-infrared light (e.g., the K domain at $\sim 2.2 \mu\text{m}$ and longer) covers multiple dust grains, where polarimetric colour in this wavelength can reflect *ensemble* properties of dust aggregates resulting from the interaction between the dust constituents, such as the aggregation status (i.e., structure and porosity) and bulk composition. Comparatively, dust grains or the so-called monomers on the order of $\sim 0.1\text{--}1 \mu\text{m}$ (Mannel et al. 2019) are the dust units optical polarimetry most sensitively explores, thereby polarimetric colour at this wavelength represents more of the characteristics of *individual* scattering units. As a consequence, infrared wavelengths can exhibit more electromagnetic interactions between the monomers compared to shorter wavelengths.

The interaction strength between dipole-like monomers decreases as r^{-3} , where r is the distance between the two dipoles (Eq. (1.56) from Jackson 1998), and dust aggregate geometry is directly influenced by the mechanical properties of dust (such as its structure and porosity). Compact dust aggregates exhibit stronger interactions between monomers than less compact dust, since a greater number of monomers are present at a given wavelength. It is therefore useful to compare wavelength dependence of P_r of dust from various comets to diagnose their relative bulk

structural differences. Both observations and modelling have corroborated this idea (Gustafson and Kolokolova 1999; Kolokolova and Kimura 2010; Kwon et al. 2019, 2022b).

Dust composition can also effectively affect the interaction distance. Increasing (decreasing) dust's total absorption would suppress (enhance) multiple scattering, which has an equivalent effect to diminishing (increasing) mutual interactions and results in redder (bluer) polarimetric colours (Rouleau and Martin 1991; Warren 2019). A depletion of organic molecules in fine-scale dust has been proposed as a plausible explanation for several comets with blue polarimetric colours in the optical wavelength (Kiselev et al. 2015 and references therein).

4.3.3 Plausible relationship with comet dynamics

With an increasing number of comet observations, researchers are searching for macroscopic trends in dust properties between comets with different dynamics. Comets are classified into two primary groups based on their dynamical properties (Dones et al. 2015 for a review): Jupiter-family comets (JFCs) and Oort-cloud comets (OCCs). As a class of short-period ($\lesssim 20$ yrs) comets, including Encke types, JFCs originate from the Scattered disc beyond Neptune, and Jupiter's motion largely influences their dynamics (Duncan and Levison 1997; Nesvorný et al. 2017). Conversely, OCCs, or long-period comets (>200 yrs) that are further divided into dynamically new and old comets from the Oort cloud, spend most of their time on the cryogenic ($T \sim 10$ K) outskirts of the Solar System and pass by the Sun once every million years or in their lifetime (Vokrouhlický et al. 2019).

In comets orbiting towards the inner Solar System, grain properties may vary as a function of nucleus depth, since solar radiation and heating tend to deplete volatiles near the surface (Priyalnik et al. 2004). A frequent visit to the Sun naturally leads JFCs to develop relatively more altered surface layers compared to OCCs. Accordingly, OCCs tend to display higher levels of activity (e.g., Garcia et al. 2020) and peacock various coma features, such as jets, spirals, and circumnucleus haloes, implying that more abundant fresh particles may reside on the surface or in the near-surface layer of their nuclei (Hines and Levasseur-Regourd 2016). Dust particles ejected from the subsurface by active JFCs near the Sun (Gundlach et al. 2020) and shortly after the Deep Impact experiment on 9P/Tempel 1 are found to have polarimetric properties similar to those characteristic of OCCs (Hadamcik and Levasseur-Regourd 2009). Supporting evidence indicates that comets with a small perihelion distance have a smaller P_r at the given phase, ensuring that solar radiation is the primary source of dust modification (Kolokolova et al. 2007; Kwon et al. 2021).

Recent research has focussed on the diversity of a dynamic population, especially amongst OCCs. OCCs exhibit a broad range of activity as evidenced by their brightness, coma morphology, and their evolution as a function of heliocentric distance (Meech et al. 2016; Licandro et al. 2019; Garcia et al. 2020). A census-wise systematic approach to linking dust characteristics with comet dynamics in comet polarimetry is still in its infancy; Nonetheless, recent polarimetric studies have shown that sub-populations of OCCs may possess distinct dust properties, suggesting a potential heterogeneity of OCCs that comprise the present-day Oort cloud in their

formation and/or evolution (e.g., Ivanova et al. 2021; Kwon et al. 2022b; Ivanova et al. 2023b). In this respect, polarimetry on distant comets (comets with perihelion distances beyond the sublimation region) is a relatively new field that has revealed differences from the majority of comet populations in aperture polarimetry (Sect. 4.2.1). In particular, distant comets tend to exhibit sharp radial dependences in P_r and colour, which, combined with the much redder nucleus colour and prominent jets, suggests the active fragmentation of icy, organic-rich dust particles in the coma (e.g., Ivanova et al. 2015; Dlugach et al. 2018; Ivanova et al. 2019, 2023b). Distant comets are thought to undergo rapid changes in their perihelion as they journey towards the inner Solar System from the inner Oort cloud (Fouchard et al. 2017). The use of comet polarimetry to link dust characteristics with comet dynamics in a census-wise systematic approach will provide a deeper understanding of the evolution of the Solar System.

4.4 Open questions

Several findings in comet polarimetry require further confirmation by independent research groups before a consensus can be reached.

One example of an open question is measuring circular polarisation (CP) of coma dust. CP observations have been carried out on a dozen active comets in imaging polarimetric mode. Most comets show left-handed (negative) circular polarisation at diverse observing geometries (Kiselev et al. 2015 for a review). In attempts to explain left-handed CP dominance, several mechanisms (e.g., dust grain alignments) have been proposed, all with their own limitations. The origin of comet CP is unknown at the moment. A concern has been raised about the magnitude and uncertainty of the measurements, often on the order of 0.01 %, which might be potentially instrumental. Any optical element that precedes the polarimetric optics can induce cross-talk from linear to circular polarisation, and its intensity appears to increase with distance from the field of view centre (Keller 2002; Bagnulo et al. 2002). Figures 10 and 11 of Bagnulo et al. (2009) and Fig. 9 of Siebenmorgen et al. (2014) show examples of the effect of cross-talk from linear to circular polarisation in the FORS instrument, and propose the observational strategies to minimise its impact. Admittedly, whilst instrumental effects can explain the observed CP values, they cannot explain why the majority of comets show negative CP.

Detection of anisotropic coma features in imaging polarimetry is another discrepancy. Constructing polarimetry maps for dust coma requires meticulous data reduction handling. In particular, an incorrect photocentre alignment between the images used for construction can lead to spurious features near the photocenter, often seen as exceptionally peaked polarised regions (either negative or positive; Fig. 14). Imperfect corrections for atmospheric effects or tracking errors can produce misleading features in the extended coma signal (Zhang et al. 2022; Gray et al. 2024a). This issue is more likely to occur in polarimetric optics without a beam splitter, since atmospheric variations would be introduced during successive exposures with varying retarder angles.

Independent cross-checks and open discussions between different research groups, including determining the future direction of collaborations, are needed to resolve

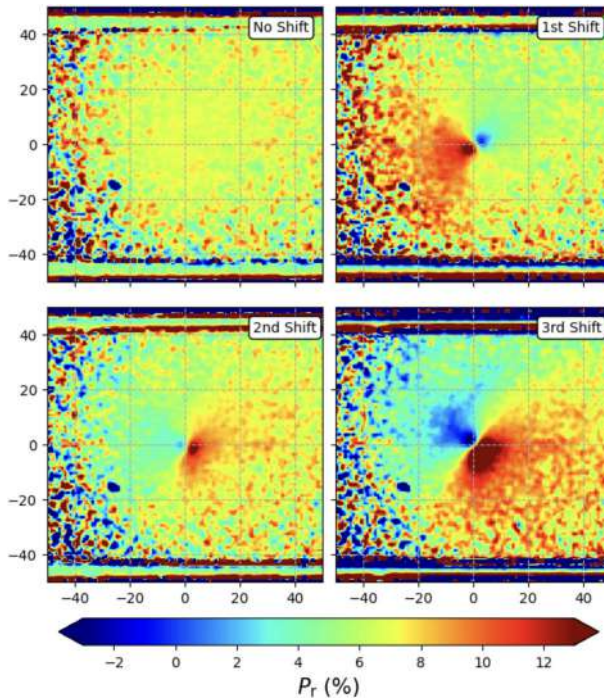


Fig. 14 Photocentre misalignment experiment performed with VLT/R-filter data (central wavelength: $0.655 \mu\text{m}$) of comet 67P/Churyumov-Gerasimenko. The “No Shift” panel (top left) shows the original data without deliberate misalignment, whilst the remaining panels show the randomly generated three iterations of the shift experiment. High-contrast regions are found close to the photocentre in misaligned cases. Image reproduced with permission from Gray et al. (2024a), copyright by the author(s)

several conflicting issues, which is a crucial first step towards a deeper understanding of comets.

5 Solar System planets, the Moon, and Titan

Sunlight that is reflected by a planet gets polarised, because it is scattered by gas and aerosol and cloud particles in the atmosphere (see e.g. Hansen and Travis 1974), if there is any, and/or because it is reflected by the surface, if there is any. The degree of polarisation of this reflected light (i.e., the polarised flux divided by the total flux) and its direction are very sensitive to the microphysical properties of the scattering particles, such as their size distribution, composition (i.e., their refractive index), shape, and, for non-symmetric particles, their orientation. The polarisation is also very sensitive to the packing density of the particles on regolith-like surfaces, and to the refractive index and macroscopic roughness of other types of surfaces, such as ice caps or liquids.

Through the wavelength dependence of the optical properties of scattering particles, the polarisation depends on the wavelength λ of the light, also because light

of different wavelengths reaches different regions in a planetary atmosphere and hence different scatterers. Note that thermal radiation that planets emit can also become polarised when it is scattered by particles in the atmosphere and/or on the surface. The degree of polarisation of this radiation is, however, usually small because of symmetry in the emission and scattering processes (for numerical examples, see Stolker et al. 2017; de Kok et al. 2011, and references therein). The few available observations of polarised thermal radiation will be discussed below.

Sunlight that is reflected by a planet is predominantly linearly polarised. The circularly polarised flux is usually very small as it mostly arises when light is scattered at least once by particles that are large compared to the wavelength of the light, such as aerosol or cloud particles (Rayleigh scattering alone does not give rise to circularly polarised light, as can be deduced from the shape of the single-scattering matrix, see Eqs. (2.14) and (2.15) in Hansen and Travis (1974)). Because circular polarisation usually only arises upon multiple scattering, it holds less information about the scattering particles than the linear polarisation, as the latter is mostly due to singly scattered light. In Eq. (1), the degree of linear polarisation, P_r , is defined as $(F_{\perp} - F_{\parallel}) / (F_{\perp} + F_{\parallel})$, with F_{\perp} and F_{\parallel} the fluxes polarised, respectively, perpendicular and parallel to the scattering plane. Regarding light that is scattered by planets, there can also be a flux component that is polarised under an angle of 45° or 135° with respect to the scattering plane (Stokes parameter U in Eq. A1). However, when the reflecting atmosphere and/or surface are relatively mirror symmetric with respect to the reference plane, this latter component is usually small enough to ignore. We will thus use P_r when referring to the degree of polarisation unless stated otherwise.

The linear polarisation is mostly due to singly scattered light. In particular, the angular variation of P_r , such as where the polarisation reaches a maximum and where it is zero (the 'neutral points'), holds the information on the properties of the scatterers or reflecting materials as it can be related to the characteristic phase curve of the singly scattered light. Multiple scattered light usually has a low degree of polarisation, because the polarisation directions have been randomised. This light dilutes the absolute degree of polarisation of the reflected light without affecting the relative angular variation.

We will first discuss the illumination and viewing geometries of planets and their relation with the phase angle and the single scattering angle (Sect. 5.1). Then, we cover polarimetric data of all Solar System planets, and Titan (Sects. 5.3–5.10), but, like Lyot almost a century ago (Lyot 1929), starting with the Moon in Sect. 5.2.

5.1 Phase angles and scattering angles

The polarisation of light that has been reflected by a planet is very sensitive to the local illumination and viewing geometries as these determine the local single-scattering angle. When observing the planet from afar, such as with an Earth-based telescope, these geometries across the planet are determined by phase angle α : the angle between the directions to the Sun and the observer, measured from the centre of

the planet, see Fig. 1. Given phase angle α , the single scattering angle Θ is then equal to $180^\circ - \alpha$.

Whilst Θ is the same across the planetary disc, the polarisation signal across the disc will not be the same because of horizontal and vertical variations in the types of particles that scatter the light (depending on the local illumination and/or viewing directions, the incident light will reach different layers of scatterers and/or the light that emerges from the atmosphere has been scattered in different layers). The contribution of multiple scattered light, with usually a low degree of polarisation, will also vary across the disc: the smaller the local solar zenith angle (i.e., the higher the Sun is above the local horizon) and/or the smaller the local viewing angle (i.e., the higher the observer is above the local horizon), the larger the fraction of observed light that has been multiply scattered in the denser lower layers of the atmosphere or, in the absence of a significant atmosphere, by the particles in the deeper regions of the surface layer.

When a planet is observed from close-by, from a spacecraft that performs a fly-by or that is in orbit around the planet, the single scattering angle Θ of the observations varies along the orbit (whilst traditionally the term 'phase angle' has been used for planets as a whole, it is sometimes also used for local, spatially resolved observations).

With an Earth-based telescope (on the ground or in space), Mercury and Venus can be observed at phase angles close to 0° (at 0° , they are precisely behind the Sun) to 180° (at precisely 180° , they are transiting the Sun), see Fig. 1. For these planets, and also for the Moon, we can thus measure (almost) complete flux and polarisation phase curves. Measuring the polarisation of these planets at the smallest and largest phase angles is, however, extremely challenging because of the Sun's proximity and the very small values of P_r at these angles. Indeed, at $\alpha = 0^\circ$ P_r of a horizontally homogeneous planet is zero because of symmetry. Near $\alpha = 180^\circ$, when the planet's dark night side is in view, P_r also tends to zero.

From the Earth, the outer planets (and any moons and rings) can only be observed at α 's ranging from close to 0° to a maximum phase angle $\alpha_{\max} \approx \arcsin 1/D$, with D the distance between the planet and the Sun (in au). For example, $\alpha_{\max} \approx 46^\circ$ for Mars, and $\alpha_{\max} \approx 11^\circ$ for Jupiter. Only small parts of their phase curves can thus be measured. For rough surfaces, the branch of negative polarisation at small phase angles is very sensitive to the surface properties, but for planetary atmospheres, intermediate phase angles, where the polarisation is usually larger and where there is a clear distinction between scattering by gas molecules and scattering by aerosol or cloud particles, are more informative. For the outer planets, polarimetry is thus best done from an orbiter or a fly-by spacecraft that offer access to a wide range of phase angles. Below, we will discuss polarimetric data of the various planets, Titan, and the Moon as obtained using Earth-based telescopes and, when available, spacecraft.

5.2 The Moon

Lyot (1929) presented polarisation curves of the Moon for phase angles ranging from 1° (this lower limit is determined by lunar eclipses) to 160° (the higher limit is determined by the light of the Earth's sky when the Moon is visible at those phase

angles). An important discovery of Lyot was the branch of negative polarisation for α smaller than approximately 23° , with a minimum value of P_r (for the lunar disc as a whole) of about -1.2% at $\alpha = 11^\circ$. For $\alpha > 23^\circ$, the lunar polarisation is positive, steadily increasing with α until a maximum P_{\max} is reached, and then decreasing again. An example of a phase curve with such a shape is shown in Fig. 2. Lyot's phase curves measured before the full Moon differed from those measured after the full Moon, with in particular a P_{\max} of almost 8.8% near $\alpha = 110^\circ$ before full Moon, and a maximum of 6.6% at $\alpha = 100^\circ$ after full Moon. Lyot inferred that this difference was due to the fact that the lunar surface that is illuminated before full Moon has a larger coverage by the darker 'seas', which he found to have a higher polarisation than the brighter 'highlands'. From a comparison with measurements of various samples in the laboratory, he concluded that the lunar surface is covered by powder-like material with a composition that would resemble that of terrestrial volcanic ashes.

An excellent review of lunar observations including polarimetry since Lyot (1929) is given by Shkuratov et al. (2011). They also discuss the apparent inverse relationship between in particular the polarisation, P_r , and the surface albedo A , known as Umov's law, which is given by $P_r \propto 1/A$. Thus, the brighter the surface, the lower P_r . This is rather straightforward to understand qualitatively: the brighter the surface, the more multiple scattering between the particles on the surface, and because multiple scattering randomises the direction of polarisation, multiple scattered light usually has a low degree of polarisation. The relation between P_r and A can clearly be seen in Fig. 15.

The precise relation between P_r and A depends on the characteristic size of the particles, the definition of which is not very strict, because the lunar surface particles have very irregular shapes. The typical particle size is $50\text{--}100\ \mu\text{m}$, with the particles across the highlands having smaller sizes (for a detailed discussion, see Jeong et al. 2015). Figure 16 shows the maximum degree of polarisation P_{\max} as a function of the wavelength λ as measured by Dollfus and Bowell (1971) for two regions on the Moon: a sea and a highland. Note that the phase angle at which the polarisation is maximum increases with decreasing albedo A (for details, see Shkuratov et al. 2011; Dollfus and Bowell 1971).

The relation between P_r and A provides a sensitive tool to detect weak absorption bands in lunar reflection spectra: the identification of such bands using standard spectroscopy requires normalising the measured reflected flux spectra by the incident solar spectrum, a procedure that is prone to introducing uncertainties. The degree of polarisation, however, is independent of the incident flux as it is a relative measure, and an absorption band will show up as an 'emission feature' in a polarisation spectrum. A detailed description of this method can be found in Wöhler et al. (2024).

The Moon's circular polarisation is negligible (see e.g. Shkuratov et al. 2011, and references therein) and is mostly due to multiple scattering in the regolith, with the degree and direction of circular polarisation mostly being determined by geometrical effects, similar to those on Mercury (Sect. 5.3), rather than by the properties of the scattering particles.

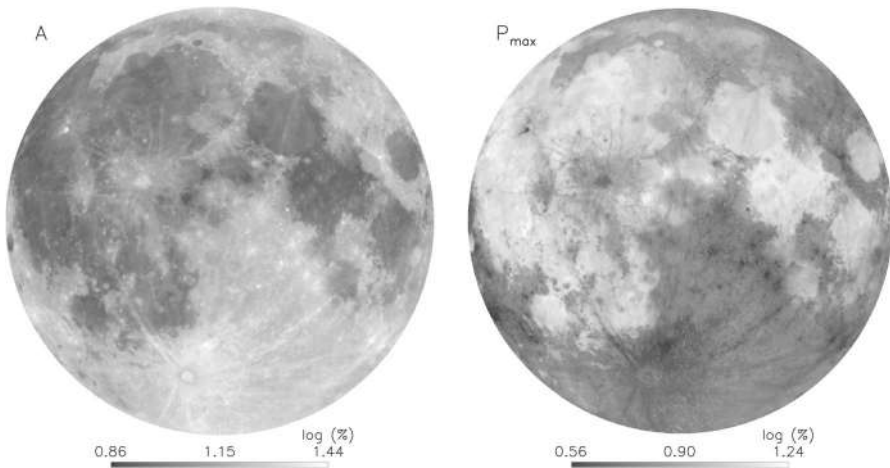
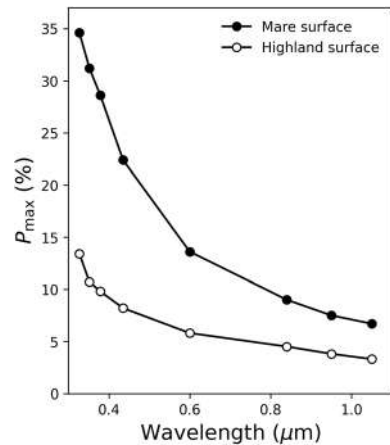


Fig. 15 Maps of the lunar albedo A (on the left), and the maximum degree of polarisation P_{\max} (in %, on the right) at $0.650 \mu\text{m}$, illustrating the Umov-effect. Albedo map from Velikodsky et al. (2011), reprinted with permission from Elsevier, and P_{\max} map from Jeong et al. (2015), reprinted with permission from the author

Fig. 16 The maximum degree of polarisation P_{\max} (in %) measured for a lunar sea ('Mare surface') and a highland as functions of the wavelength λ (in microns). Figure after Shkuratov et al. (2011) using data from Dollfus and Bowell (1971)



5.3 Mercury

The apparent diameter of Mercury is only between 4.5 and 11 arcsec and this tiny planet is only observable close to the Sun, which makes accurate polarimetric observations very hard. Various attempts were made to use polarimetry to detect an atmosphere around Mercury (see, e.g., Lyot 1929; Dollfus 1955) but only an upper limit of 0.2 mbar could be determined (see also Dollfus and Auriere 1974; O'Leary and Rea 1967), whilst UV measurements during the 1974 fly-by of NASA's Mariner 10 spacecraft yielded an upper limit of 2×10^{-9} mbar (Broadfoot et al. 1974). Mercury's polarisation signal is thus virtually only due to the reflection of sunlight by its surface.

Dollfus (1955) presented spatially resolved polarimetric data of Mercury at phase angles α ranging from 20° to 140° at 540 and 650 nm. It was found that P_r had a very similar smooth phase angle dependence at the two wavelengths with negative polarisation for $\alpha < 25^\circ$, with a minimum of polarisation equal to -1.4% around $\alpha = 10^\circ$, and the highest polarisation (of about 8% , slightly higher at green wavelengths) around quadrature ($\alpha = 90^\circ$). From this, it was concluded that Mercury's surface should be similarly to that of the Moon, i.e., covered by a regolith-like, fine material. Dollfus also measured variations in P_r that were attributed to surface spots that rotated in and out of view, with darker spots associated with higher polarisation, as expected from Umov's Law. Indeed, using a ground-based telescope, Kiselev and Lupishko (2004) measured variations in Mercury's disc-integrated P_r of about 1.5% across the planetocentric longitude range between 265° and 330° .

A comprehensive overview of Mercury polarimetry was presented by Dollfus and Auriere (1974), including spatially resolved and disc-integrated data at wavelengths from 330 to 580 nm, and data from Lyot (1929) and Ingersoll (1971). This collection of data clearly showed that P_{\max} occurs around $\alpha = 110^\circ$, and that the value of P_{\max} polarisation decreases with λ , from 12.3% at 350 nm, to 6.8% at 630 nm. Dollfus and Auriere (1974) compared the Mercury data against the polarisation of lunar analogue samples, and concluded that 'the surface material on Mercury is optically identical to lunar samples of fines from amongst the lightest mare regolith material.'

Kemp and Wolstencroft (1971) presented circular polarisation observations of Mercury at 680 nm, with a disc-integrated degree of polarisation of 0.012% and with a remarkable asymmetry between the northern and the southern hemispheres, which could be explained by second-order scattering by crystal grains on the surface (Bandermann et al. 1972). Landau (1975) performed observations of Mercury's thermal polarisation, at $3.5 \mu\text{m}$, which shows dependence on α , as that angle determines which part of the surface and thus which surface temperatures are in view. A typical value is 13% near quadrature. Model simulations linked the observations to a surface material that is loosely packed on cm- and m-scales but compact on μm -scales (Bandermann et al. 1972; Meierhenrich et al. 2002).

5.4 Venus

Venus is the archetypal planet to study with polarimetry as, from the Earth, it can be observed at a wide range of phase angles, namely from about 5° to about 174° , and its maximum elongation is about 46° , which enables observations when the planet is high in the sky compared to Mercury, and when the sky is relatively dark. Its apparent diameter reaches $21''$ which also allows spatially resolved observations. As Lyot (1929) already remarked: the degree and direction of polarisation of Venus is very different from that of the Moon, Mercury, or Mars. The polarisation changes sign a few times across the whole phase angle range, and depends strongly on the wavelength. Because of Venus's horizontally homogeneous cloud deck, its degree of polarisation depends mostly on α , and much less on which part of the clouds is visible to the observer. Figure 17 shows P_r of Venus' whole disc as a function of the planet's phase angle α as measured over almost a decade at a range of wavelengths between 0.34 and $0.9 \mu\text{m}$ (Coffeen and Gehrels 1969). The measurements show a

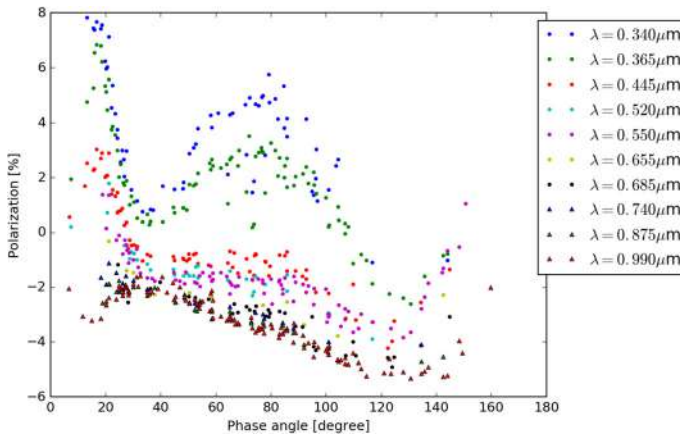


Fig. 17 The degree of polarisation P_r (in %) of Venus (disc-integrated) as function of the phase angle α for a range of wavelengths λ as measured between April 1959 and January 1968. Positive (negative) values indicate that the direction of polarisation is perpendicular (parallel) to the plane through the Sun and the planet. Data from Coffeen and Gehrels (1969)

strong wavelength dependence and a strong phase angle dependence. The scatter is largest at the shortest wavelengths and could indicate a variability in the haze optical thickness. At the longer wavelengths, P_r is mostly determined by the scattering properties of the particles in the upper cloud layer, which apparently show less variability over time.

Hansen and Arking (1971) concluded from comparing the data of Lyot (1929) and Coffeen and Gehrels (1969) with their computations that the cloud particles are spherical with radii of about $1 \mu\text{m}$, and that the refractive index is 1.45 at $\lambda = 0.55 \mu\text{m}$. The clouds could thus not be made of water, which was a very important insight that could not have been derived from data of the reflected solar flux. Kattawar et al. (1971) arrived at similar conclusions using the same data whilst refining the refractive index as being between 1.45 and 1.6. Hansen and Hovenier (1974) used an extended data set by combining Earth-based polarisation observations of Venus from Lyot (1929), Coffeen and Gehrels (1969), Dollfus and Coffeen (1970), and Veverka (1971a), across all phase angles, at wavelengths of $0.365 \mu\text{m}$, $0.445 \mu\text{m}$, $0.55 \mu\text{m}$, $0.655 \mu\text{m}$, and $0.99 \mu\text{m}$ (not all combinations of phase angles and wavelengths were available). From their comparison against numerical simulations, Hansen and Hovenier (1974) concluded that the cloud particles have a refractive index of 1.44 at $\lambda = 0.55 \mu\text{m}$ to 1.43 at $0.99 \mu\text{m}$, which is consistent with 75% sulfuric acid solution (H_2SO_4). The effective radius of the cloud particles is $1.05 \mu\text{m}$ and the effective variance of their size distribution is only 0.07. By modelling the amount of Rayleigh scattering above the clouds, they derived that the clouds reside high in the atmosphere: a cloud optical thickness of 1.0 is reached at an altitude of about 50 mbars.

The above-mentioned data all pertained to Venus's whole disc or a large region on the disc. Venus has also been observed by polarimeters in close-up, from a spacecraft. The Pioneer Venus spacecraft carried the Orbiter Cloud Photopolarimeter (OCPP)

(Colin and Hunten 1977) that performed polarimetry from 1978 to 1990. Detailed analyses of the data have been presented by Kawabata et al. (1980), Knibbe et al. (1997), and Knibbe et al. (1998). They confirmed the sizes and compositions of the cloud particles derived from Earth-based observations, but from the orbiter data, they also found that the clouds were overlaid by an extensive haze layer that consists of particles with an effective radius of $0.23 \mu\text{m}$, and a size distribution with an effective variance of 0.18. These haze particles have a refractive index of 1.45 at $\lambda = 0.55 \mu\text{m}$, indicative of a sulfuric acid solution. Another finding was that the haze optical thickness was largest at latitudes above about 55° , with typical values of 0.8 at $\lambda = 365 \mu\text{m}$, whilst at lower latitudes the optical thickness was as small as 0.06. These values pertained to data from January 1979, and the haze optical thickness appeared to be highly variable across the planet and in time. A later analysis of the OCPP data by Braak et al. (2002b) concluded that the haze particle column density decreased gradually during the Pioneer Venus Orbiter mission, whereas the cloud top pressure showed little variation.

In 2006, ESA's Venus Express spacecraft entered its orbit around Venus. SPICAV, one of the spectrometers onboard, had some polarimetric capabilities (Bertaux et al. 2007), however, without having been calibrated for such measurements, as polarimetry was not its main goal. This made it difficult to establish the measurement errors. Rossi et al. (2015) present the available data, obtained between 2006 and 2010, from 0.56 to $1.7 \mu\text{m}$, mostly across the northern hemisphere. At single scattering angles Θ between 180° and 160° , P_r shows a characteristic glory-signature with negative polarisation. With decreasing Θ , P_r increases strongly, reaching values of 0.10 for slant geometries with Θ close to 90° at the highest latitudes, due to the small polar haze particles.

EnVision, ESA's upcoming Venus spacecraft (launch planned for 2032) carries the Venspec-H spectrometer that will be outfitted with two linear polarisation filters covering two near-infrared spectral bands. Besides giving information about the microscopic properties of atmospheric clouds and hazes, Venspec-H's future spectropolarimetric observations of Venus might also be used to study atmospheric waves that are known to 'roam' in Venus's atmosphere (see, e.g., Silva et al. 2024; Fukuhara et al. 2017, and references therein), as suggested with numerical simulations by Mahapatra et al. (2021).

5.5 Earth

Despite the obvious advantages of spectropolarimetry for remote sensing of the Earth, there have been very few polarimetric observations of our planet from space. Apart from some polarisation observations performed from a space shuttle (Egan et al. 1991), the POLarisation and Directionality of Earth's Reflectances (POLDER) instrument (Deschamps et al. 1994) onboard JAXA's ADEOS satellites has so far provided the only data, albeit in a single broadband and with a rather low accuracy of about 2%. NASA's recently (February 2024) launched PACE satellite does carry two polarimeters that will allow us to better study the Earth's polarisation signal as seen from space.

There have been many ground-based polarimetric observations of the Earth's sky that show the typical contributions of Rayleigh scattering at short wavelengths, in particular the high polarisation band at 90° from the Sun, and aerosol scattering at longer wavelengths. Examples of high-spectral polarisation spectra from the UV to the near-infrared are presented by Aben et al. (1999) and Aben et al. (2001); a sample spectrum from their data is shown in Fig. 18, taken with a telescope on the roof of a building surrounded by greenery. Note that the solar zenith angle for these observations was about 79° , and as the viewing direction was towards the zenith, the single-scattering angle was about 100° . The shape of this polarisation spectrum is determined by: Rayleigh scattering, aerosol scattering and absorption, absorption by trace gases, and reflection by the surface. Rayleigh scattering contributes most at the shorter wavelengths: around 320 nm, P_r is low because of multiple scattering, and it increases with increasing wavelength, because multiple Rayleigh scattering decreases. As the single-scattering angle is close to 90° , P_r reaches high values (up to 65% in the continuum). At longer wavelengths, aerosol scattering becomes more important (the sky was relatively clear on that day: the aerosol optical thickness was small), causing P_r to decrease. Above about 700 nm, P_r sharply decreases, because at these wavelengths, the surface albedo is high (the so-called 'green edge' of vegetation), and sunlight that has been reflected upwards by the surface is scattered back downwards by the atmosphere into the telescope. The polarisation shows various high-spectral resolution features that are due to absorption by trace gases: at the shortest wavelengths, ozone absorbs strongly, effectively removing multiple scattered light and increasing P_r to its singly scattered value, and similarly, absorption by water vapour and oxygen lead to increases in P_r across the spectrum (see Aben et al. 1999; Stam et al. 1999, and references therein). Finally, the sharp dips in P_r at the shorter wavelengths are due to rotational Raman scattering, an inelastic scattering process that leaves Fraunhofer-line shaped features in the spectrum (see Aben et al. 2001; Stam et al. 2002, for numerical simulations of these lines, and for references).

Whilst we do not yet have polarisation data that cover the Earth seen from space, there have been observations of the polarisation of Earthshine: sunlight that has first been reflected by the Earth and then by the Moon. Measuring this light allows one to get a view of the polarisation of the Earth from afar, albeit with the depolarising reflection by the lunar surface in between. The first polarimetric observations were obtained (in a broadband filter) by Dollfus (1957), who measured a fraction of polarisation of about 10% at a phase angle of the Earth of $\sim 90^\circ$. With modern instruments, polarised Earthshine measurements were obtained by, e.g., Sterzik et al. (2012), Takahashi et al. (2013), Miles-Páez et al. (2014), Sterzik et al. (2019). An application of these Earthshine observations, and one that has driven the modern observations, is for Earth-like exoplanet characterisation: because starlight can be considered to be unpolarised, whilst the starlight that is reflected by a planet is usually linearly polarised, polarimetry can help to enhance the contrast between the weak planet signal and the background of light of the parent star, and thus to detect an exoplanet. In addition, the exoplanet's polarisation signal could be used to characterise the planet (see Vaughan et al. 2023, and references therein). Depending on the planet's size and albedo, and on the star's luminosity, the planet's polarisation

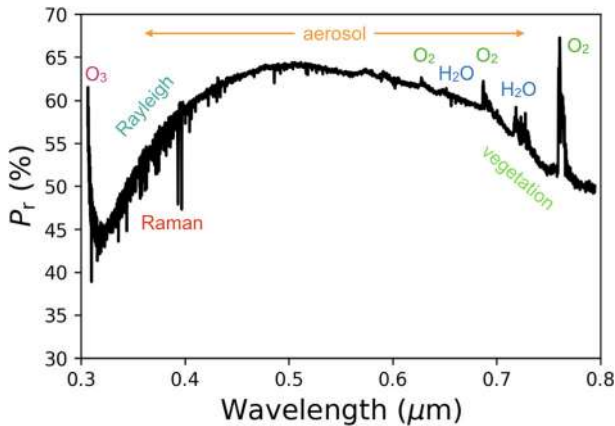


Fig. 18 The degree of linear polarisation of the cloud-free zenith sky as measured using the breadboard model (BBM) of the GOME instrument (Burrows et al. 1999) that was onboard ESA's ERS-2 satellite. Whilst GOME was sensitive to the polarisation of the incoming light, it could only measure the polarisation in one direction and in broad bands. For the purpose of these measurements, the GOME BBM was outfitted with rotating polarisation filters. The measurements were performed on April 7th, 1997. The solar zenith angle was about 79° . The precision is on the order of 10^{-3} . See the text for an explanation of the spectral features. From the dataset of Aben et al. (1999)

fraction could be anything between 10^{-12} and 10^{-6} . Practically, polarimetry of Earth-like exoplanets is being investigated for future instruments and telescopes. In the meantime, Earth itself is being used as a benchmark to test how well imaging and spectropolarimetric measurements may constrain a planet surface, its atmospheric composition, including bio-signatures, by comparing observations to modelling results such as those of Stam (2008), Emde et al. (2017), and Trees and Stam (2022).

Dollfus (1957) assumed that the reflection from lunar surface would cause a depolarisation of a factor $\sim 3.3\%$, leading to the conclusion that the linear polarisation of the light scattered by Earth was about 30 – 35%. The interpretation of all recent spectropolarimetric Earthshine research obviously still suffers from the difficulty of not knowing the depolarisation of the lunar surface (some empirical considerations are given by Bazzon et al. 2013). Furthermore, it is very difficult to separate the weak Earthshine signal from the bright background of scattered moonlight. Nevertheless, Earthshine spectropolarimetry has detected the presence of oxygen and water in the Earth's atmosphere (Sterzik et al. 2012), and it has been shown that its modelling can even constrain the mean water droplet sizes, the mean cloud fraction of liquid water clouds, and the mean optical depth of the water clouds (Sterzik et al. 2020; Vaughan et al. 2023).

Following a previous attempt with observations of Mars by Sparks et al. (2005, see Sect. 5.6), Earthshine has been also been targeted for circular polarisation measurements, with the idea that it could be a benchmark for future attempts to detect biotic material on other astronomical objects (Sterzik and Bagnulo 2009). The outcome of these FORS1+VLT observations was, however, that the signal was highly contaminated by cross-talk from linear polarisation (see Sect. A.2.4). Attempts to measure circular polarisation of Earthshine with the ISIS instrument on

the William Herschel Telescope (WHT) led to a null result (Bagnulo & Sterzik, unpublished).

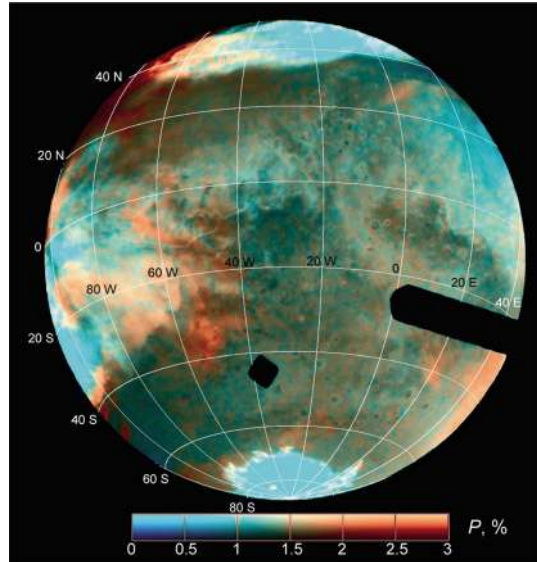
5.6 Mars

From Earth, Mars can be observed at phase angles α up to about 46° . The polarisation of Mars is determined by the surface reflection, the thin Rayleigh scattering atmosphere, dust aerosol particles in the atmosphere, the ice caps (when in view), and the water and carbon dioxide ice clouds. The amount of atmospheric dust and cloud coverage varies strongly throughout the year. The surface shows both bright and dark regions that can change their appearance depending on the dust storm activity. Mars has been observed extensively with polarimetry, starting with Lyot (1929), who discovered a negative polarisation branch at small phase angles, which is indicative for regolith-like surfaces covered by small particles. Other observations were performed by for example Dollfus (1955), Dollfus and Focas (1969), Dollfus et al. (1969), and Ingersoll (1971). Ebisawa and Dollfus (1993) give an overview of data gathered over 14 years at Tokyo observatory, and identify the atmospheric dust particles that contribute to Mars' polarisation signal: the thin layer of sub- μm sized background dust with a smallest optical thickness of about 0.1, denser layers of similar particles with typical optical thicknesses of about 0.4 that can persist for a few weeks, and really dense storms in which larger particles with sizes of up to a few μm are lifted into the atmosphere.

Shkuratov et al. (2005) give an overview of earlier work and present spatially resolved polarisation images taken with the High-Resolution Camera (HRC) of the Advanced Camera for Surveys (ACS) (Pavlovsky et al. 2002) on the Hubble Space Telescope in three wide band filters with effective wavelengths of 250, 330, and 435 nm. The polarisation images (see Fig. 19 for an example) agree generally well with those presented by Ebisawa and Dollfus (1993), albeit that they have a much higher spatial resolution. Interestingly, Shkuratov et al. (2005) also measure large negative polarisation values (of up to -2%) at ultraviolet wavelengths that they suggest could be due to thin ice clouds.

The Mars-5 spacecraft of the USSR has performed the only polarimetric measurements of Mars at intermediate phase angles, namely at about 90° , with two polarimeters set under different angles (Ksanfomaliti et al. 1975) measuring in nine bands from 342 to 749 nm. Unfortunately, the mission survived for only 22 orbits and the phase angle coverage is very limited, thus limiting the amount of information that can be retrieved from the polarimetry. An analysis of available data is presented by Santer et al. (1985) and Santer et al. (1986). They concluded that during the short Mars-5 mission, the atmosphere was very clear, although in the polarisation signals, occasional dust veils consisting of irregularly shaped particles, and ice clouds consisting of non-spherical and, from a comparison with laboratory data, potentially crystalline particles with sizes of 10–100 μm , showed up. From the observations across the terminator and limb of the planet, thus without the surface below and capturing a long path through the atmosphere, a polarisation signal of a few percent indicated the presence of a thin layer of high-altitude (40–60 km) aerosol with a

Fig. 19 A colour map of the degree of polarisation (in %) in filter F435W overlaid on a brightness picture of Mars, as both observed with HST on September 7, 2003. The black strip and dot on the planet are instrument artefacts. The bright region on the north polar region is a cloud. The polarisation indicates that especially on the western side of the disc, there are several ice clouds. Image reproduced with permission from Shkuratov et al. (2005), copyright by Elsevier



refractive index of about 1.55, which was distributed in size according to a power law distribution.

A circular polarisation signal could possibly identify homochiral, organic molecules (see, e.g., Patty et al. 2019, and references therein), and Sparks et al. (2005) describe circular polarisation measurements of Mars with an Earth-based telescope to search for traces of life. Laboratory measurements of the circular polarisation of light that is scattered by organic materials such as photosynthetic cyanobacteria show wavelength-dependent polarisation features up to 0.05%, whilst no such signals appear when non-organic materials are illuminated. It has to be kept in mind that these laboratory measurements were performed on samples consisting of only bacteria, whilst under natural circumstances, the signal can be expected to be diluted when the bacteria (or other organisms) are mixed with non-organic materials. When observing Mars itself, no circular polarisation was detected. However, as also remarked by Sparks et al. (2012), such a detection or indeed a non-detection requires a very precise instrument with a high spatial resolution, for example, on a spacecraft orbiting Mars or on a lander or rover.

5.7 Jupiter

From the Earth, the maximum phase angle under which Jupiter can be observed is about 11° , which severely limits capturing the phase angle variation of its degree of polarisation. However, even this small phase angle range offers the possibility to identify the different contributors to the polarisation signal in spatially resolved observations. The polarisation signal of Jupiter is due to the scattering of the incident sunlight by the gaseous atmosphere, by the clouds forming the relatively low-lying belts and the higher zones, by the clouds in the hurricane-like storms, the most

famous of which is the Great Red Spot (GRS), by the hazes overlying the clouds, and by the photochemical hazes covering the polar regions. There are also linearly polarised auroral emissions by H_3^+ of up to 7% near $4\mu\text{m}$ and circular polarisation up to about 10%, as reported by Barthelemy et al. (2011).

Early observers like Lyot (Lyot 1929) could already distinguish low polarisation in the middle of Jupiter's disc, and high polarisation (5%–7%) over the polar regions. This was confirmed by later observers, such as Dollfus (1955), Gehrels et al. (1969), Morozhenko and Yanovitskii (1973), and by Shalygina et al. (2008) and Schmid et al. (2011). Recent spatially resolved polarimetric observations in the B, V, and R filters at phase angles from 4° to 10.5° were presented by McLean et al. (2017), an example of which is shown, together with the mapped total flux, in Fig. 20. Their observations also show a generally low degree of polarisation near the centre of the disc, and a significant increase of the polarisation with increasing latitude, up to 20% near the southern pole and a few percent lower near the northern pole, which can be attributed to seasonal variations in the polar haze optical thickness (see below). Note that the measured degree of polarisation will depend strongly on the spatial resolution of the observations, with a lower resolution (larger pixels) generally leading to a lower degree of polarisation.

The low polarisation in the centre of Jupiter's disc compared to the poles is due to the small phase angle and to the fact that the main scatterers are cloud particles that are relatively large compared to the wavelength and have a low degree of polarisation of their singly scattered light at such small phase angles. What can also be seen in the polarimetric images of McLean et al. (2017), that in the B-filter, thus at the shortest wavelengths, the belts and zones show up clearly, with lower polarisation in the belts and higher polarisation in the zones: the lower the clouds, the more gas above them and the higher P_r , as at these angles, Rayleigh scattering yields higher polarisation than the cloud particles. With increasing wavelength, the difference in P_r decreases, because the contribution of Rayleigh scattering decreases with wavelength. Interestingly, in the B-band, the Great Red Spot (GRS) shows up as a low polarisation zone with a higher polarisation region just south of its centre. It is unlikely that this higher polarisation is due to Rayleigh scattering, because, as described by Anguiano-Arteaga et al. (2021) and references therein, the GRS has a higher altitude than its surroundings, and there should thus be less gas above it. In this case, the high polarisation can however be explained by the absorption of light with short wavelengths and thus less multiple scattered light, which usually has a relatively low degree of polarisation. The effect of absorption increasing the polarisation due to the decrease of multiple scattered light is also observed in the spectropolarimetric observations by, e.g., Anguiano-Arteaga et al. (2021) and McLean et al. (2017): P_r is generally higher in the methane absorption bands.

As mentioned above, the polarisation of Jupiter has been observed to increase with increasing latitude, with especially sharp increases at latitudes (north and south) above 60° at small phase angles. This increase has been attributed to the scattering by the small, photochemically produced particles that form the polar hazes. A peculiar polarisation effect, however, is the north–south asymmetry in this increased polarisation of 1–2%, which was already found by Gehrels et al. (1969). Shalygina

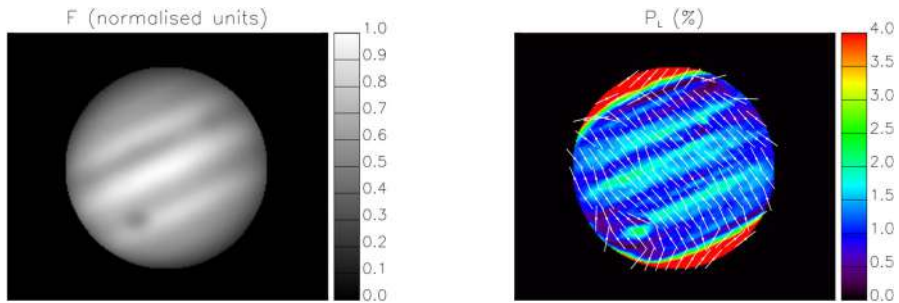


Fig. 20 Maps of the (normalised) flux (left) and degree of polarisation (right) of Jupiter observed at $\alpha = 10.5^\circ$. The spot on the lower left part of the disc (dark in flux and light blue in polarisation) is the Great Red Spot (GRS). The thin white lines on the polarisation map indicate the local direction of the polarisation. Image reproduced with permission from McLean et al. (2017), copyright by ESO

et al. (2008) provide an overview of historic data with their own measurements and analysis. Indeed, they conclude that the asymmetry is a seasonal effect with the polarisation being higher in the local winter: even though Jupiter's obliquity is very small (only about 3°) combined with the ellipticity of Jupiter's orbit (0.05), the seasonal variations in the local insolation can influence the local formation of stratospheric aerosol, with an increase in solar flux leading to a decrease in aerosol and a decrease in the degree of polarisation. Note that the observations by McLean et al. (2017) were obtained between the end of 2014 and the end of 2015, whilst the Sun crossed Jupiter's equator from the northern to the southern hemisphere in the beginning of February 2015. These observations thus took place during the end of the northern summer, and the lower polarisation near the northern pole thus agrees with the analysis by Shalygina et al. (2008). The polarimetric images taken in March 2003, thus about one Jupiter-year earlier, by Schmid et al. (2011) also show a lower degree of polarisation near the north polar region than near the south polar region (6% versus 8%).

There are some polarimetric data at intermediate phase angles as there were instruments with (linear) polarimetric capabilities on NASA's Pioneer 10 and 11 spacecraft that performed fly-bys of Jupiter, and on the Galileo orbiter (there was also a polarimeter on the Voyager spacecraft, see Lillie et al. 1977, but there appears to be no published analysis of polarimetric data of Jupiter). Coffeen (1974) discussed observations at $\alpha = 103^\circ$, from which they derived that the cloud particles in the upper layers should be non-spherical. Assuming Rayleigh scattering above a Lambertian reflecting surface, they derived that the tops of the north tropical zone, parts of the equatorial zone, and the GRS are approximately 15 kms higher than the surrounding areas. The lowest parts are the north and south temperate regions. The main results of Smith and Tomasko (1984) are the strong increase of the polarisation with increasing latitude above 40° north and below 48° south. These increases are attributed to an increasingly thick polar haze. The lack of rainbow-like scattering features leads to the conclusion that the cloud and haze particles are non-spherical, similar to what was concluded by Coffeen (1974). Tomasko and Doose (1984) find a thin haze, of probably photochemical origin, over all latitudes, that is mostly visible

at red wavelengths. They also derive altitude variations in the cloud top altitudes, with pressures of 150 ± 50 mb in the zones and 270 ± 80 mb in the belts. An overview of the analysis of the Pioneer data has been presented by Braak et al. (2002a), who also analysed Galileo data. From comparing the data against model computations, they conclude that the cloud particles should exhibit negative polarisation (i.e., parallel to the scattering plane) at intermediate scattering angles, such as has been measured in laboratory set-ups for ammonia ice particles.

Wolstencroft (1976) provides an overview of the circular polarisation measurements of Jupiter, pointing out the observed sign change of the polarisation between the northern and the southern hemisphere, which according to Hansen (1971) is a geometrical effect.

5.8 Saturn

The maximum phase angle under which Saturn can be observed from the Earth is only about 6° . Saturn's polarisation signal is determined by similar processes at that of Jupiter, except that the scattering by the ring particles adds a separate signal. Santer and Dollfus (1981) analysed linear polarisation measurements of Saturn between 350 and 580 nm, taken over a period of almost 20 years, and explained the data with a cloud layer of spherical particles with a refractive index of 1.44 that is covered across the whole planet by a haze layer with submicron-sized, oriented, non-spherical particles. The optical thickness of this layer was found to vary over time. Schmid et al. (2011) presented spectropolarimetric data of Saturn and its ring taken in 2003, at $\alpha = 3.7^\circ$, when the rings were close to their maximum opening angle, and with the planet's south pole in view (the rings covered the north polar region). A striking feature in Saturn's polarisation is a region of high positive polarisation (almost 2%) around the equator. North and south of this region, P_T approaches zero before increasing steeply at northern latitudes that are just visible below the ring. The polarisation also increases towards the southern pole, but only up to about 1%, thus not as prominently as on Jupiter, which could be due to Saturn's more homogeneous haze coverage. As noted by Schmid et al. (2011), they had observed this equatorial polarisation feature before, in 2002 and in 2003. However, it was not detected by, e. g., Hall and Riley (1974).

From space, Saturn has been observed using polarimetry by the Voyagers, Pioneer, and Cassini. West et al. (1983b) discuss the polarimetric data of the Voyager 2 photopolarimetry experiment at 264 nm and 750 nm concluding that above the clouds, there is a significant amount of UV-absorbing haze particles. In Gehrels et al. (1980), the results of polarimetric observations by the imaging photopolarimeter (IPP) aboard the Pioneer 11 are discussed: at a phase angle close to 90° , the polarisation from the centre of the disc to the limb at blue wavelengths indicates that the cloud particle density decreases with altitude. A more in-depth study of Pioneer 11 data was provided by Tomasko and Doose (1984): at blue wavelengths, the polarisation on the disc rises from close to zero at small phase angles to more than 10% near $\alpha = 100^\circ$ just south of the equatorial region ($7^\circ - 11^\circ$ S) and to more than 20% between 15° and 17° S. At large-phase angles, the polarisation decreases to

zero, similar as for Rayleigh scattering. At red wavelengths, the polarisation is negative (parallel to the scattering plane) at intermediate α in the regions mentioned above, which suggests the presence of relatively large cloud particles. At all latitudes, and in both colours, the polarisation increases steeply towards the terminator and limb at $\alpha = 90^\circ$.

Swedlund et al. (1972) performed circular polarisation measurements of Saturn close to the 1971 opposition, and measured values of P_r on the order of several times 10^{-4} , with the expected geometrical sign changes. There appeared to be a correlation between higher circular polarisation in the presence of absorption in the atmosphere between 400 and 900 nm.

5.9 Titan

Saturn's largest moon, Titan, is unique, because it has an atmosphere that is thicker than the Earth's. Earth-based polarimetry of Titan suffers from the same small phase angle range as that of Saturn; the maximum phase angle is only about 6° . However, polarimetry in a broadband from 0.3 to 0.8 μm led Veverka (1973) to suggest that Saturn's largest moon had a cloudy atmosphere overlaid by a Rayleigh scattering layer, because of the positive polarisation (i.e., perpendicular to Titan's light equator) across the (small) phase angle range at which the observations took place.

Tomasko (1980) reached a similar conclusion from polarimetric disc-integrated measurements at blue and red wavelengths by the Imaging Photopolarimeter (IPP) aboard Pioneer 11 at a phase angle range from 15° to 97° : the high polarisation in the blue and the lower values in the red suggest very small haze particles above an effectively depolarizing lower layer. The size of the haze particles appears to increase with decreasing altitude. A refinement of the data reduction and analysis was presented by Tomasko and Smith (1982), and they found that the degree of polarisation of Titan at $\alpha = 96^\circ$ and at blue wavelengths was 56.1% in the blue and 48.5% in the red IPP channel. They report problems fitting both the high single scattering polarisation and the strong forward scattering that the particles in the upper atmosphere should exhibit to fit both the polarimetric and the photometric data, and suggest that including bimodal size distributions or non-spherical particles in the model atmospheres might improve the fitting. Lane et al. (1982) report on polarimetry during Voyager 2's fly-by: Titan's polarisation was measured as positive along a broad phase angle range that could not be fitted with a single size haze particle. West et al. (1983a) also analysed Voyager 2 data and stumbled onto the same problem as that identified from the Pioneer 11 data (Tomasko and Smith 1982), and they conclude that non-spherical particles are needed to fit the data. West and Smith (1991) were able to explain the observations by the presence of aggregate particles with a mean projected area equal to that of a sphere with a radius of 0.14 μm , consisting of monomers with mean radii near 0.06 μm . They note that aggregate particles could also account for the observed optical properties of Jupiter's high-altitude haze.

Bazzon et al. (2014), finally, analysed polarimetric imaging data of Titan by ACS HRC and the NICMOS instruments on HST, in seven filters covering wavelengths

from 0.25 and 2 μm . The accompanying intensity images had already been analysed by Lorenz et al. (2004), Lorenz et al. (2006), who found a hemispherical asymmetry that was indicative of a seasonal effect in the thickness of the stratospheric haze. The polarimetric images do not show such an asymmetry. Whilst the polarisation at the centre of Titan's disc is virtually zero, it increases towards the limb, with the degree of polarisation reaching about 10% in the NIC1 band, around 1 μm . The limb polarisation is due to second-order Rayleigh scattered light (the direction is perpendicular to the limb).

5.10 Uranus and Neptune

There are little polarimetric data on the ice giants Uranus and Neptune. Seen from Earth, they span only, respectively, about 3.5 and 2 arcsec on the sky and reach maximum phase angles α of only about 3° and 2° , respectively, severely limiting the use of polarimetry for atmospheric characterisation. NASA's Voyager 2 has been the only spacecraft to visit them and that thus allowed for a better spatial resolution and access to larger phase angles. It appears, however, that Voyager 2's photopolarimeter PPS (Lillie et al. 1977) acquired only photometric data during its 1985 Uranus fly-by (see, e.g., Lane et al. 1986; Pryor et al. 1997; Pryor and Hord 1991), although there are some polarimetric data from its 1989 Neptune fly-by (Pryor et al. 1992). We will first discuss this fly-by data of Neptune and then the available Earth-based polarimetric observations of these two planets.

Voyager 2's PPS measured only the total flux and the linearly polarised fluxes [see Eq. (1)]. The spacecraft's orientation precluded the acquisition of polarimetric data at intermediate phase angles: only the data in the range of 13° – 14° could be used. The polarimetric data pertain to scans across latitudes from -80° to $+30^\circ$ in spectral bands with effective wavelengths of 265 nm and 750 nm. At 265 nm, the highest values of P_r [see Eq. (1)], of about 5%, are found near the South pole, and P_r decreases towards zero with increasing latitude (recall that α is only between 13° and 14°). According to the analysis by Pryor et al. (1992), this is consistent with Rayleigh scattering in the gas above the hazes and clouds. At 750 nm, deeper atmospheric layers are being probed, and Q/I shows more variation with latitude, yet mostly between 0% and 2.5%, which would indicate scattering by aerosol particles with low single-scattering polarisation signatures at these phase angles. Pryor et al. (1992) provide no further analysis of this data.

There has been some Earth-based polarimetry of Uranus and Neptune. Michalsky and Stokes (1977) presented disc-integrated polarimetry (Q/I) of Uranus at effective wavelengths of 450 nm, 645 and 665 nm (with half-maximum bandwidths of about 100 nm), taken at subsolar latitudes of about -45° to -50° (Uranus' south pole was thus in view), at α 's up to about 3° . At $\alpha \approx 0^\circ$, the polarisation at all wavelengths is zero within the errors, indicating a mostly horizontally homogeneous atmosphere. At larger α 's and the red wavelengths, the polarisation remained consistent with zero, except at $\alpha \approx 3^\circ$, where it increased slightly to about 3×10^{-4} . At the blue wavelength, P_r showed negative values up till $-1.5 \cdot 10^{-4}$ around $\alpha = 0.6^\circ$ and increased to about $6 \cdot 10^{-4}$ at $\alpha \approx 3^\circ$. From a comparison with numerical simulations

of Rayleigh scattering atmospheres by Kattawar and Adams (1971), Michalsky and Stokes (1977) conclude that their observations are not consistent with a Rayleigh scattering atmosphere, but instead indicate the presence of high altitude hazes or thin clouds.

Schmid et al. (2006) obtained disc-resolved polarimetric measurements of Uranus (at $\alpha = 2.8^\circ$) and Neptune (at $\alpha = 1.7^\circ$) in spectral bands around 650, 800, and 900 nm (disc-integrated, Uranus' 650 nm data agree well with those of Michalsky and Stokes (1977)). As expected, both Uranus and Neptune show virtually zero polarisation in the central regions of their discs, and the polarisation increases towards the limb, with a maximum P_r of about 1.3% for Uranus at 800 nm, and about 1.6% for Neptune at 650 nm (at 800 nm, Neptune's P_r is about 1.2%). The polarisation across the discs is strongly symmetric around the centres of the discs, indicating an absence of horizontal inhomogeneities. At the time of these observations, in 2003, the subsolar latitudes on Uranus and Neptune were about -20° and -30° : polar hazes would thus have revealed their presence in the polarisation along the limbs, like they do at Jupiter and Saturn. The direction of polarisation is perpendicular to the limbs which is indicative of second-order Rayleigh scattering. Indeed, the disc-resolved pattern of polarisation as measured by Schmid et al. (2006) can be explained by scattering by gas or small particles above deep cloud decks.

Joos and Schmid (2007) show spectropolarimetric data from 530 to 930 nm for specific regions on Uranus' and Neptune's discs. This spectral region includes several absorption bands of methane, which show up as emission features in the polarisation (up to about 3%) mostly because of the increased contribution of low-order scattering, with generally higher polarisation, in the presence of absorption (see, e.g., Stam et al. 2004). At the time of these observations, in 2007, Uranus was close to equinox; thus, both hemispheres were into view. Indeed, whilst the polarisation spectra of the various regions on the planets' discs have very similar behaviours, i.e., decreasing continuum polarisation with increasing wavelength with superimposed methane bands in emission, the bands are less pronounced in Uranus' northern limb polarisation spectra, which could indicate larger amounts of aerosol particles in the northern polar region, which had just started to being illuminated again after the long polar night.

6 Dusty laboratory measurements and modelling

Characterisation of dust particles in the Solar System is a crucial aspect of planetary science and astrophysics. They can be found in the atmospheres of planets and satellites (Sect. 5), comets (Sect. 4), or covering the surfaces of planets, satellites, and asteroids (Sects. 5, 2, and 3). These particles not only provide insights into the history and composition of Solar System bodies but also have practical implications for space exploration and the design of spacecraft and equipment. Furthermore, dust particles by scattering and absorbing solar radiation may play a key role in the radiative balance of planetary atmospheres.

Dust particles in the Solar System consist of irregular refractory materials spanning over a broad range of composition and morphologies (compact and/or porous). Further, they are distributed in size from the submicron region up to tens of microns in planetary/cometary atmospheres or even mm-cm-sizes if they are covering solid surfaces. The analysis of the morphology of the observed polarisation phase curves provides information on the physical characteristics of the scattering dust particles.

The development of advanced numerical algorithms for computing electromagnetic scattering by irregular particles has made significant progress in recent decades (see, e.g., Draine and Flatau 1994; Muinonen and Saarinen 2000; Mishchenko et al. 1996; Mackowski and Mishchenko 2011; Petrov et al. 2011, 2012; Mackowski 2022). Despite this, simulating the scattering of light by realistic dust particles remains challenging, due to the diverse range of shapes and sizes observed in Solar System objects. An interesting approach is to use available databases that provide pre-calculated single-scattering properties for a broad range of dust sizes and refractive indices. Those databases have been developed to provide reliable optical properties for terrestrial aerosol particles. It is widely known that the accurate estimation of aerosol impact on the atmospheric radiative balance requests for aerosol optical properties based on realistic model particles (see, e.g., Kahn et al. 1997; Mishchenko et al. 2003; Dubovik et al. 2006), and references therein). Even when the databases are devoted to terrestrial atmospheric studies, they might be extremely useful for astronomical applications. We refer to Meng et al. (2010) for a database consisting of tri-axial ellipsoidal particles and Saito et al. (2021) for hexahedral dust particles.

The case of atmosphere-less Solar System objects is even more complicated. That is the case of Mercury, the Moon, most of the satellites of planets and asteroids. These bodies are characterised by their regolith-covered surfaces, which are composed of touching solid particles and ice. Regolith surfaces belong to the class of closely packed media. Scattering by such macroscopic particulate medium is not fully solved yet. We refer to Stankevich et al. (1999), Mackowski and Mishchenko (2011), Tishkovets and Jockers (2006), Tishkovets and Petrova (2020), Muinonen et al. (2015), Grynko et al. (2020), Grynko et al. (2022), Väisänen et al. (2020), and Mackowski (2022) for recent developments of multiple light scattering by discrete particulate media.

All in all, experimental polarisation phase curves for well-characterised dust particles in air or covering a surface remain a valuable tool for proper interpretation of polarisation observations of dusty objects in the Solar System. Additionally, they can be used for validating advanced computational techniques developed to simulate scattering by clouds of particles under single scattering conditions or dense scattering media. In this section, we review experimental data aimed at disentangling the effect of dust physical parameters—size, composition, and morphology—on the main features of the polarisation curve, specifically $(P_{\min}, \alpha_{\min}, \alpha_{\text{inv}}, h, P_{\max}, \alpha_{\max})$.

It should be noted that the dust scattering properties and consequently the polarisation-phase curves do not depend on particle size, but on the ratio of the size to the wavelength, i.e., on the so-called size parameter ($x = 2\pi r/\lambda$), where r denotes the particle radius and λ is the wavelength of the incident radiation. This relationship

underscores a fundamental principle of electromagnetic light scattering known as the scale invariance rule (SIR), as outlined in Mishchenko (2006). According to the size relative to the wavelength, the following size scattering regimes are defined: *Rayleigh* regime ($|mx| \ll 1$, where m is the complex refractive index) e.g., scattering of visible light off gas molecules; *resonance* regime ($r \approx \lambda$); and *geometric-optics* regime ($r \gg \lambda$). Note that the resonance regime is often known also as *Mie* regime. However, Lorenz–Mie theory refers to scattering by spherical particles regardless of their size. To avoid confusion, we refer to the resonance scattering regime when throughout the manuscript dealing with sizes of particles of the order of the wavelength of the illuminating source.

Further, when characterising a cloud of dust particles, its size distribution is typically described by two parameters: the effective radius (r_{eff}), and the effective variance (v_{eff}) defined as Hansen and Travis (1974)

$$r_{\text{eff}} = \frac{\int_0^\infty r \pi r^2 n(r) dr}{\int_0^\infty \pi r^2 n(r) dr}, \quad (10)$$

$$v_{\text{eff}} = \frac{\int_0^\infty (r - r_{\text{eff}})^2 \pi r^2 n(r) dr}{r_{\text{eff}}^2 \int_0^\infty \pi r^2 n(r) dr}. \quad (11)$$

The effective radius is an area weighted mean radius of the dust size distribution, whereas the effective variance provides a measure of the width of the size distribution. From the effective radius value, we can obtain the corresponding effective size parameter ($x_{\text{eff}} = 2\pi r_{\text{eff}}/\lambda$), at the experiments/observations wavelengths.

Dust composition is characterised by its complex refractive index ($m = n + ik$) as a function of wavelength. The complex refractive index is a measure of how light is refracted and absorbed as it propagates within the material. The real component (n) is the ratio of the speed of light in a vacuum to the phase speed of the light in the material. The imaginary component (k) describes the attenuation of the light as it propagates within the material.

In Sect. 6.1, we present a brief summary of laboratory techniques dedicated to producing polarisation curves of cosmic dust particles. Section 6.2 introduces the scattering matrix formalism. Experimental polarisation curves for (clouds of) dust grains in air and regoliths are presented in Sects. 6.3 and 6.4, respectively.

6.1 Light-scattering techniques

Several approaches can be considered for obtaining the polarisation phase curves for clouds of small dust particles. For instance, the microwave analogue experiment is based on the SIR rule. For microwave analogue measurements, a millimetre- or centimetre-sized scattering target with the desired refractive index and shape is manufactured. Microwave radiation scatters off this object, and the results are extrapolated to other wavelengths by maintaining a fixed ratio of size to wavelength (Zerull et al. 1993; Gustafson 1996; Vaillon et al. 2011). New developments in 3D printing open new vistas for manufacturing dust analogue particles with full control over particle shape and refractive index (Vaillon and Geffrin 2014).

Measurements on a single small dust particle can also be conducted at shorter wavelengths by combining light-scattering measurements with electrostatic, acoustic, and optical techniques to capture and levitate particles (see, e.g., Weiss-Wrana 1983; Maconi et al. 2020; Arnold et al. 2022). An interesting review on particle levitation and laboratory scattering is provided by Reid (2009). The main advantage of measuring isolated particles lies in the precise control over the shape, size, and refractive index of the particle of interest. However, a notable drawback is that these measurements can only be carried out for one particle with a specific size, shape, and orientation at a time.

An alternative approach involves using visible light scattered by an ensemble of randomly oriented particles. This method allows for working with realistic cosmic dust analogue samples with sizes ranging from submicron up to several hundreds of microns (e.g., Pope et al. 1992; Volten et al. 2001; Lévassieur-Regourd et al. 1998; Muñoz et al. 2011). In those cases, the scattered light is collected by either a detector located on a moving arm or a set of detectors spanning over a fixed phase angle range. Whilst measurements of the degree of linear polarisation phase curve are a valuable tool for characterising dust particles in the Solar System, the full scattering matrix is needed to perform multiple scattering calculations in scattering media such as planetary atmospheres (see Sect. 5). It has been proved that neglecting the polarised nature of light in radiative modelling of planetary atmospheres leads to significant errors in the determination of the scattered contribution to the measured flux and atmospheric optical thickness with direct impact in the retrieved atmospheric gaseous mixing ratio (Stam and Hovenier 2005; Moreno et al. 2007). The Amsterdam (Volten et al. 2001), IAA-CODULAB (Muñoz et al. 2011), and Fresnel laboratories (Vaillon et al. 2011) provide complete experimental scattering matrices at visible and microwave wavelengths, respectively. Section 6.2 provides a brief summary of the scattering matrix formalism.

As in the case of light-scattering simulations, open access to experimental scattering databases provides an interesting tool for, e.g., direct comparison with astronomical observations or for testing light-scattering numerical techniques. We refer to the Granada-Amsterdam Light Scattering database (Muñoz et al. 2025) and PROGRA2 database Renard et al. (2024) for the full or one or two elements of the scattering matrix at visible wavelengths, respectively, and Geffrin and Sabouroux (2009) for the Fresnel ElectroMagnetic Scattering with COntrolled Particules (EMSCOP) Database based on the microwave analogue experiment.

As mentioned in previous sections, ground-based polarimetric observations of small Solar System objects are in many cases limited to a narrow phase angle range in the backward direction, i.e., the so-called negative polarisation branch (NPB). This characteristic has been extensively explored through laboratory experiments (Shkuratov et al. 2006; Hadamcik et al. 2006; Nelson et al. 2018; Muñoz et al. 2021; Spadaccia et al. 2022, 2023; Martikainen et al. 2023) and theoretical simulations (Petrova et al. 2007; Muinonen et al. 2012; Tishkovets and Petrova 2013; Escobar-Cerezo et al. 2017). The NPB is produced by the spatial asymmetry of the internal fields of an irregular wavelength-scale single particle (the single-particle mechanism) (Muinonen et al. 2011) and by the coherent back-scattering mechanism (CBM). The CBM is a phenomenon where radiation attains a maximum in the

backward direction due to the interference of scattered light beams produced by the individual particles of a cloud (Muinonen et al. 1989; Shkuratov 1989; Muinonen 1990; Muinonen et al. 2012). In a dense scattering media as is the case of planetary regoliths, the back-scattering response is a combination of single scattering from individual particles and multiple coherent and incoherent scattering in the bulk medium. We refer to Shkuratov (1989), Muinonen et al. (1989, 2015), Grynko et al. (2020, 2022) for a comprehensive description of the back-scattering phenomena.

A traditional limitation of laboratory polarimeters is the lack of data at very small phase angles. When approaching the backward direction, the detector blocks the light source. Several experimental devices have been specially designed for measuring the NPB of particulate surfaces up to near exact backward direction ($\alpha = 0$). In those cases, either the detector is located at a long distance from the sample, or the back-scattered light is collected by a mirror (Gautam and Sorensen 2021) or lenses (Ovcharenko and Shkuratov 2000) and sent to the detector located at a fixed position. Such is the case of the Minipol Instrument ($0.05^\circ \leq \alpha \leq 5^\circ$) at the Lunar and Planetary Laboratory at the University of Arizona, USA (Geake and Geake 1990), the goniometric photopolarimeter (GPP) formerly located at the Jet Propulsion Laboratory, Pasadena CA ($0.05^\circ \leq \alpha \leq 5^\circ$, Nelson et al. 2000) and updated and re-located at Mount San Antonio College, Walnut CA, USA ($0.05^\circ \leq \alpha \leq 15^\circ$, Nelson et al. 2018), the Kharkov's short- ($0.2^\circ \leq \alpha \leq 17^\circ$ Shkuratov et al. 2002) and large-phase angle ($2^\circ \leq \alpha \leq 160^\circ$, Ovcharenko et al. 2006) photopolarimeters located at the Astronomical Institute of Kharkov National University, Ukraine, or the polarimeter POLICES ($0.8^\circ \leq \alpha \leq 30^\circ$, Poch et al. 2018) at the University of Bern, Switzerland. In these cases, the powder of interest is located in a sufficiently large and deep sample holder, so that the semi-infinite medium approximation can be assumed.

6.2 Scattering matrix formalism

Solar light scattered by a dust particle (or cloud of dust particles) can be fully described by the 4×4 scattering matrix, \mathbf{S} (Hovenier et al. 2004). The scattering matrix transforms the Stokes parameters of the incident light ($\{I_i, Q_i, U_i, V_i\}$) into those of the scattered light ($\{I_s, Q_s, U_s, V_s\}$). Here, we assume the scattering plane (the plane containing the incident and scattering beams) as the plane of reference for the Stokes parameters. The elements of the scattering matrix, S_{ij} , are dimensionless and depend on the wavelength, dust physical properties, and direction of scattering defined by the angle between the directions of propagation of the incident and scattered beams, i.e., the phase angle ($0^\circ \leq \alpha \leq \pi$), and an azimuth angle, ϕ , that ranges from 0 to 2π . If the cloud of interest consists of particles in random orientation, all scattering planes are equivalent and the scattering direction is fully described by means of the phase angle. Further, if the number of particles is high enough so that mirror symmetry in the particle ensemble can be safely assumed, we have

$$\begin{pmatrix} I_s \\ Q_s \\ U_s \\ V_s \end{pmatrix} \propto \begin{pmatrix} S_{11} & S_{12} & 0 & 0 \\ S_{12} & S_{22} & 0 & 0 \\ 0 & 0 & S_{33} & S_{34} \\ 0 & 0 & -S_{34} & S_{33} \end{pmatrix} \begin{pmatrix} I_i \\ Q_i \\ U_i \\ V_i \end{pmatrix}. \quad (12)$$

We refer to van de Hulst (1957), Bohren and Huffman (1998), Mishchenko et al. (2000), and Hovenier et al. (2004) for a comprehensive description of the scattering matrix formalism.

In general, the incident light may be considered unpolarised (e.g., the Sun that illuminates Solar System bodies, or a star with exoplanets) ($\{I_i, Q_i, U_i, V_i\} = \{1, 0, 0, 0\}$). In that case, Eq. (2) can be defined in terms of the scattering matrix elements as follows:

$$P_r = -\frac{Q_s}{I_s} = -\frac{S_{12}}{S_{11}}. \quad (13)$$

Note that the sign difference as compared to Eq. (2) is simply due to a different frame of reference for defining the Stokes vector.

6.3 Experimental polarisation curves under single-scattering conditions

In this section, we present experimental polarisation phase curves of clouds of randomly oriented dust particles under single scattering conditions. The goal is to disentangle the effect of dust particle size, composition and morphology (porosity/compactness) on the polarisation phase curve features in the regions of maximum (P_{\max}, α_{\max}), inversion, (h, α_{inv}), and minimum polarisation (P_{\min}, α_{\min}).

6.3.1 Size effect

Figure 21 displays the experimental polarisation curves for four magnesium-rich olivine samples (Muñoz et al. 2021; Frattin et al. 2022) representative of low-absorbing dust particles. The experimental data have been obtained at the IAA Cosmic Dust Laboratory (Muñoz et al. 2011). The top panels and bottom left panel present the polarisation curve for three forsterite powders consisting of particle-size distributions belonging to the transition region Rayleigh-resonance, resonance, and geometric optics domains, respectively. The bottom right panel shows the polarisation curve of a mm-sized forsterite pebble.

Table 2 displays the r_{eff} , v_{eff} , and corresponding x_{eff} at the measurements wavelength along with information on the complex refractive index for the forsterite samples. We refer to Muñoz et al. (2021) and Frattin et al. (2022) for detailed sample characterisation.

The $P_r(\alpha)$ for the four low-absorbing samples presents a bell shape with a maximum in the $[75^\circ\text{--}95^\circ]$ phase angle range. Further, the three powdered samples show a negative branch at small phase angles. Table 3 lists the main parameters of the $P_r(\alpha)$ curves in the region of minimum and maximum polarisation, and polarimetric slope at inversion angle. As shown in Fig. 21, the trends for the maximum value of

the polarisation curve are highly dependent on the size scattering regime. For very small particles (sizes smaller than or of the order of the wavelength of the incident light), P_{\max} tends to decrease as the particle size increases into the resonance regime (Mishchenko et al. 2000). That is the case of the forsterite XS and S samples. Forsterite XS, the sample consisting of particles with sizes in the Rayleigh–resonance transition regime shows a maximum value of 20.3 %. P_{\max} decreases as particle size increases with a value of 12.9% for forsterite S. However, the tendency of decreasing values of P_{\max} when increasing the size parameter is reversed as the size parameter increases into the geometric-optics domain (Muinonen et al. 1996). In the case of $r \gg \lambda$, P_{\max} increases with particle size. As presented in Table 3, P_{\max} for forsterite XL is equal to 15.9 % increasing up to 28.2% for the millimetre-sized olivine pebble. Further, as particle size increases into the geometric-optics regime, the position of the maximum value of P_r is shifted towards larger phase angles (see, e.g., Muinonen et al. 1996; Liu et al. 2015; Escobar-Cerezo et al. 2017).

The behaviour of particles of different sizes differs also in the NPB, as clearly shown in Fig. 21. Its magnitude and the inversion angle location are highly dependent on particle size. The deepest NPB (−4.4 %) is observed for sample S, consisting of particles with sizes of the order of the wavelength of the incident light ($x_{\text{eff}} = 17$). As the dust grain size parameter increases (forsterite M), the NPB becomes shallower. Remarkably, the NPB vanishes within the error bars for the powder sample containing particles within the geometric-optics domain (forsterite XL and pebble). The dependence of the NPB on particle size parameter is also supported by the results presented by Escobar-Cerezo et al. (2018). In that work, it was shown that the removal of particles with sizes of the order of wavelength ($x_{\text{eff}} < 12$) from a cloud of micron-sized lunar dust analogue sample results in a decrease (in absolute values) of the measured NPB.

It is worth mentioning that mm-sized grains can also generate NPB at visible wavelengths. Figure 22, left panel, illustrates $P_r(\alpha)$ for three mm-sized pebbles: charcoal, spinel, and MgFeAlSi (Muñoz et al. 2020; Frattin et al. 2019). The right panel depicts the back-scattering region. Both MgFeAlSi and spinel pebbles exhibit shallow NPBs, whilst charcoal tends towards negative values at phase angles smaller than 10° . The main physical characteristics and polarisation features for the pebbles are provided in Tables 2 and 3, respectively. In this case, macroscopic grain structure, micron-sized surface roughness, and/or internal structures are likely responsible for the observed negative branch.

6.3.2 Composition effect

To test the effect of dust composition on the polarisation phase curve, we have selected two sets of samples with similar effective size parameters and particle morphology but significant differences in their refractive index at the measurements wavelength. Figures 23 and 24 display the polarisation phase curves for three sets of powdered samples with sizes in the Rayleigh-resonance, resonance, and geometric-optics regimes (Martikainen et al. 2023), and 2 mm-sized pebbles, respectively (Muñoz et al. 2020). As presented in Table 2, the imaginary part of the refractive index for the JSC Mars 1 sample is nearly two orders of magnitude higher than the

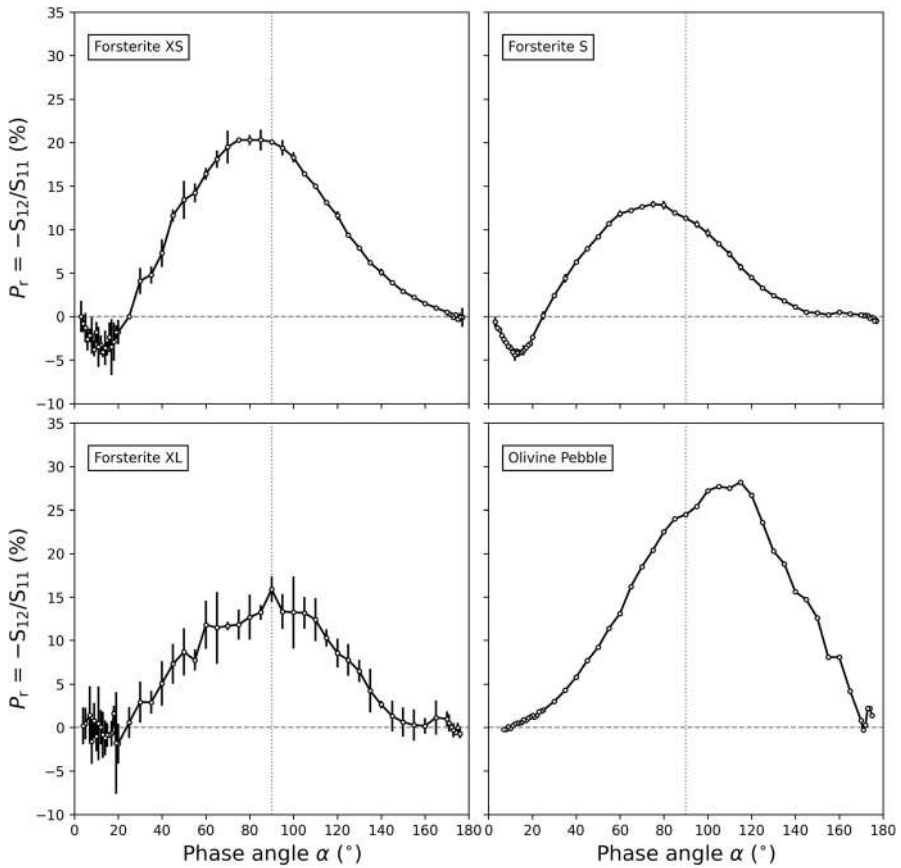


Fig. 21 Measured degree of linear polarisation curves in percentage as functions of the phase angle for samples forsterite XS (top left), S (top right), forsterite XL (bottom left), and mm-sized olivine (forsterite) pebble (bottom right)

value for the forsterite samples at the measured wavelengths. In the case of samples with sizes belonging to the resonance and geometric-optics regimes (Fig. 23, right panel, and Fig. 24, left and right panels), a higher absorption increases the value of P_{\max} . Indeed, the larger the particle size parameter, the stronger the differences in P_{\max} between low- and high-absorbing samples (Fig. 24, right panel). We do not find significant differences in the maximum of the P_r -curve for the samples consisting of particles in the Rayleigh–resonance transition size regime (Fig. 23, left panel). In all three size scattering regimes, for similar particle sizes, a higher absorption produces deeper negative polarisation branches.

As mentioned in Sect. 4.3.2, multi-wavelength aperture polarimetry is a widely observational technique for cometary characterisation. As shown in Fig. 25, dust polarisation colour is highly dependent on particle composition. The olivine sample (Muñoz et al. (2000), Frattin et al. (2019)) that shows a flat dependence of the refractive index at the measurement wavelengths shows a red polarisation colour, i.e.,

Table 2 Main physical properties of the dust samples presented in Figs. 21–22. Refractive index data from ⁽¹⁾ Henning et al. (1999), ⁽²⁾ Martikainen et al. (2023), ⁽³⁾ Trof and Thomas (1998), and ⁽⁴⁾ Duley (1984)

Sample	$r_{\text{eff}} (\mu\text{m})$	v_{eff}	x_{eff}	$m = n + ik$	Reference
Forsterite XS	0.36	0.42	4 (640 nm)	$1.65 + i1E-05$ ¹	Muñoz et al. (2021)
JSC1 S	0.4	0.03	5 (480 nm)	$1.6 + i9.5E-04$ ²	Martikainen et al. (2023)
Forsterite S	1.4	1.06	14 (640 nm)	$1.65 + i1E-05$ ¹	Muñoz et al. (2021)
Forsterite M	2.6	0.55	26 (640 nm)	$1.65 + i1E-05$ ¹	Muñoz et al. (2021)
JSC1 M	2.7	0.27	35 (480 nm)	$1.6 + i9.5E-04$ ²	Martikainen et al. (2023)
JSC1 L	16.5	0.1	216 (480 nm)	$1.6 + i9.5E-04$ ²	Martikainen et al. (2023)
Forsterite XL	47	0.12	461 (640 nm)	$1.65 + i1E-05$ ¹	Muñoz et al. (2021)
Olivine Pebble	3.8	–	46×10^4	$1.65 + i1E-05$ ¹	Frattin et al. (2022)
Charcoal Pebble	2.2	–	26×10^4	$[1.8-2.3] + i[0.5-0.9]$ ₃	Muñoz et al. (2020)
Spinel Pebble	3.4	–	41×10^4	$1.72 + i3E-03$ ⁴	Frattin et al. (2022)
Sample	r (mm)	–	x_{eff}	$m = n + ik$	

Table 3 Measured main parameters of the degree of linear polarisation curves. Data from ⁽¹⁾ Muñoz et al. (2021), ⁽²⁾ Martikainen et al. (2023), ⁽³⁾ Frattin et al. (2022), ⁽⁴⁾ Muñoz et al. (2020)

Sample	x_{eff}	P_{min} (%)	α_{min} (°)	α_{inv} (°)	P_{max} (%)	α_{max} (°)	h (%/deg)
Forsterite XS ¹	4	-4.1 ± 0.6	13 ± 1	25 ± 1	20.3 ± 0.6	80 ± 5	0.53
JSC1 S ²	5	-6 ± 4	11 ± 1	27 ± 1	21 ± 6	75 ± 5	0.67
Forsterite S ¹	14	-4.4 ± 0.7	12 ± 1	25 ± 1	12.9 ± 0.4	75 ± 5	0.62
Forsterite M ¹	26	-2.6 ± 1.3	10 ± 1	20 ± 2	12.4 ± 2.1	90 ± 5	0.37
JSC1 M ²	35	-3.3 ± 0.2	11 ± 2	23 ± 3	15.4 ± 0.3	80 ± 5	
JSC1 L ²	216	-3.2 ± 1.2	9 ± 2	21 ± 1	24.4 ± 0.4	95 ± 5	
Forsterite XL ¹	461	-1.2 ± 2.0	14 ± 1	17 ± 1	15.9 ± 1.5	90 ± 5	0.28
Olivine Pebble ³	$\sim 46 \times 10^4$	–	–	24 ± 1	33.4	115 ± 5	–
Charcoal Pebble ⁴	$\sim 26 \times 10^4$	–	–	10 ± 1	79.6	90 ± 5	0.76
Spinel Pebble ³	$\sim 41 \times 10^4$	–	–	24 ± 1	33.4	115 ± 5	–

the measured differences in the polarisation phase curves are mainly due to the decreasing effective size parameter with wavelength ($x_{\text{eff}} = 42$ at 488 nm, $x_{\text{eff}} = 33$ at 633 nm). By contrast in the case of the JSC Mars 1 sample (Fig. 25, right panel), the effect of decreasing size parameter at 640 nm is compensated by a higher absorption at 488 nm producing a blue polarisation colour (Table 4).

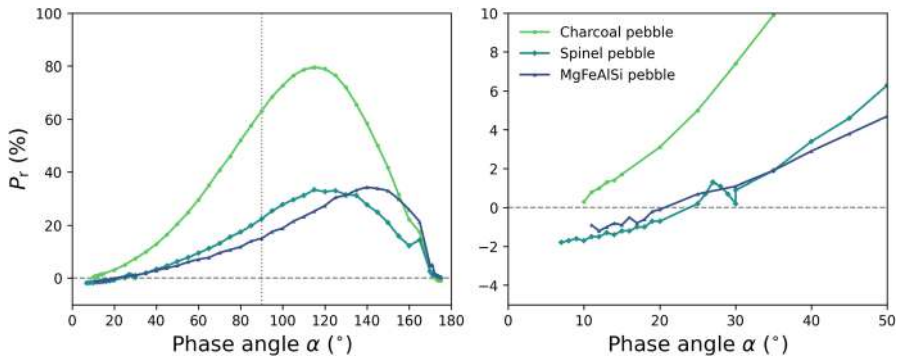


Fig. 22 Measured degree of linear polarisation phase curves at a wavelength of 520 nm for mm-sized pebbles (left pane). The right panel displays the negative polarisation branch region

6.3.3 Morphology effect

Porous dust particles (aggregates/agglomerates) are present in, e.g., cometary dust tails (Güttler et al. 2019) or the atmospheres of planets and satellites (West and Smith 1991). An aggregate particle is described by its fractal dimension, D_f , and the number, N , and size of the constituent particles (monomers) as follows:

$$N \propto (R_g/r)^{D_f}, \quad (14)$$

where R_g is the gyration radius (mean-squared of the distance from the aggregate centre of mass and each of the constituent particles centre), and r is the monomer radius. D_f takes values from 1 (chain-like) to 3 (porous spheroidal shape) (Blum 2006). In Eq. (14), we assume the same radius r for all constituent particles. The aggregate size parameter is defined as $X_{\text{agg}} = 2\pi R_m/\lambda$ where R_m is the radius of the sphere enclosing the aggregate. Vaillon and Geffrin (2014) presented a novel technique for aggregate production with full control over the aggregate parameters, the so-called stereolithography 3D printing method. This technique has been successfully used by Tobon Valencia et al. (2022) to produce a set of well-characterised mm-sized aggregate particles devoted to studying the effect of D_f , R_g , and monomer size on the measured polarisation phase curve at microwave wavelengths. The experimental data have been obtained at the microwave scattering facility in Marseille at wavelengths spanning from 100 mm (3 GHz) to 16 mm (18 GHz) (Geffrin et al. 2012). The complex refractive index of the resin used for printing the aggregates ($m = 1.7 + i0.03$) is similar to the values for astronomical silicates in the wavelength range from 0.2 to 3 μm (Draine and Lee 1984). As an example Fig. 26, left panel, displays the degree of linear polarisation curve for an aggregate with $D_f = 2$, $R_g = 17.03$ and $R_m = 26$ as a function of monomer size. As suggested by the previous computations (e.g., West and Smith 1991; Liu and Mishchenko 2018; Tazaki and Dominik 2022), in the case of porous aggregates, the maximum degree of linear polarisation is dependent on the monomers size parameter. As shown in Fig. 26, the polarisation phase curve displays a Rayleigh-like behaviour, i.e., for incident

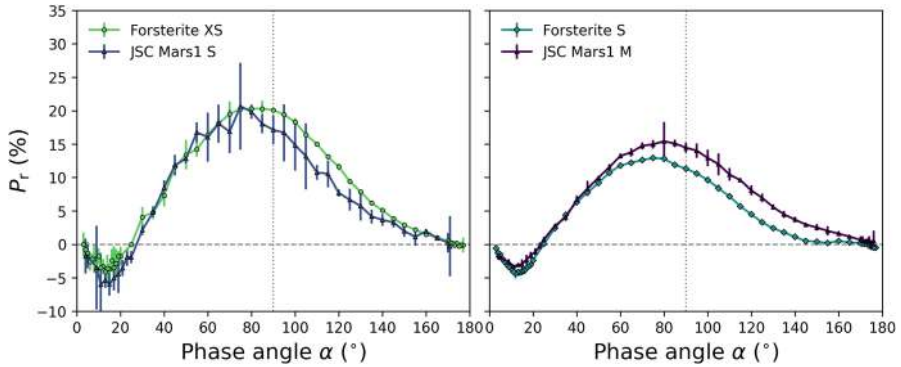


Fig. 23 Measured degree of linear polarisation curves in percentage as functions of the phase angle for forsterite XS and JSC Mars1S (left), and forsterite S and JSC Mars1 M (right)

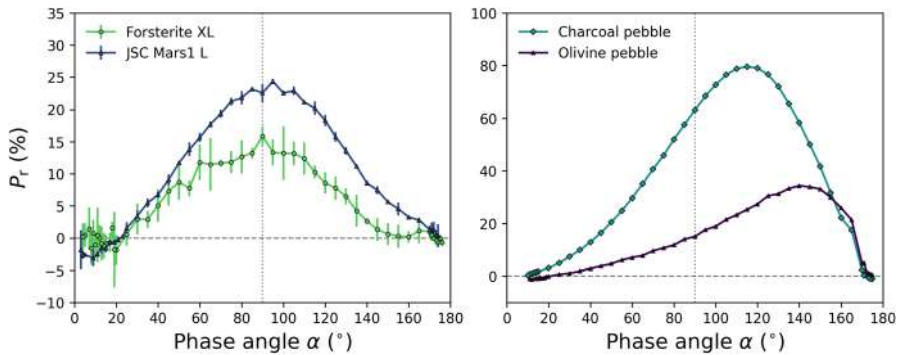


Fig. 24 Measured degree of linear polarisation curves in percentage as functions of the phase angle for samples forsterite XL and JSC Mars1 L (left) and Olivine and Charcoal pebbles (right)

unpolarised light, the scattered light is 100 % polarised at 90 degrees. As the monomer size parameter increases, the maximum P_r decreases (Volten et al. 2001; Hadamcik et al. 2006; Gómez Martín et al. 2024). Further, an increasing value of the fractal dimension (i.e., decreasing porosity) has a significant effect on the maximum value of the degree of linear polarisation. As shown in Fig. 27, P_{\max} decreases for an increasing value of D_f and the maximum value location is shifted towards smaller phase angles. Light multiple scattered within the particle serves to decrease polarisation (see, e.g., Mishchenko et al. 2006). An extreme case was studied by Muñoz et al. (2020) with a mm-size cotton ball. Light scattered many times within the porous low-absorbing ball becomes largely unpolarised. However, adding internal inhomogeneities on large ($x \gg \lambda$) low-absorbing host particles results in an increase in polarisation (Escobar-Cerezo et al. 2017).

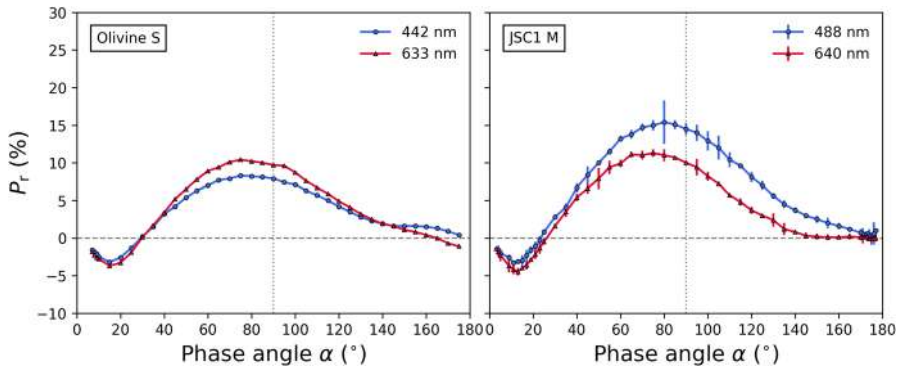


Fig. 25 Measured degree of linear polarisation curves in percentage as functions of the phase angle for Olivine S (left panel) and JSC1 (right panel) at 422 nm, 633 nm, and 488 nm, and 640 nm, respectively

Table 4 Measured main parameters of the P_r curves for fractal aggregates as function of monomer size parameter (x_{mon}), fractal dimension D_f , gyration radius (R_g), and radius of the sphere enclosing the aggregate R_m and aggregate size parameter X_{agg} . In all cases, the number of monomer particles (N) is equal to 74. (Tobon Valencia et al. 2022)

Sample	x_{mon}	D_f	R_g	R_m (mm)	X_{agg}	P_{max} (%)	α_{max} (°)
Ag_DLA_Df2.0_N74_3	0.15	2.0	17.03	26.00	1.63	96	88
Ag_DLA_Df2.0_N74_3	0.31	2.0	17.03	26.00	3.27	97	94
Ag_DLA_Df2.0_N74_3	0.46	2.0	17.03	26.00	4.74	97	92
Ag_DLA_Df2.0_N74_3	0.63	2.0	17.03	26.00	6.53	89	9f2
Ag_DLA_Df2.0_N74_3	0.94	2.0	17.03	26.00	9.81	73	90
Ag_DLA_Df2.5_N74	0.63	2.5	11.60	18.19	4.57	59	90
Ag_DLA_Df2.8_N74	0.63	2.8	9.83	15.49	3.89	58	78

6.4 Experimental polarisation curves under multiple scattering effects: negative polarisation branch of regoliths

In this section, we review experimental data devoted to studying the effect of the physical properties of the constituent particles of the reflecting surface (grain composition, size, and compactness) on the measured NPB. In a dense scattering media, the back-scattering response is a combination of single scattering from individual particles and multiple coherent and incoherent scattering in the bulk medium. We refer to Shkuratov (1989), Muinonen et al. (1989, 2015), Grynko et al. (2020, 2022) for a comprehensive description of the back-scattering phenomena.

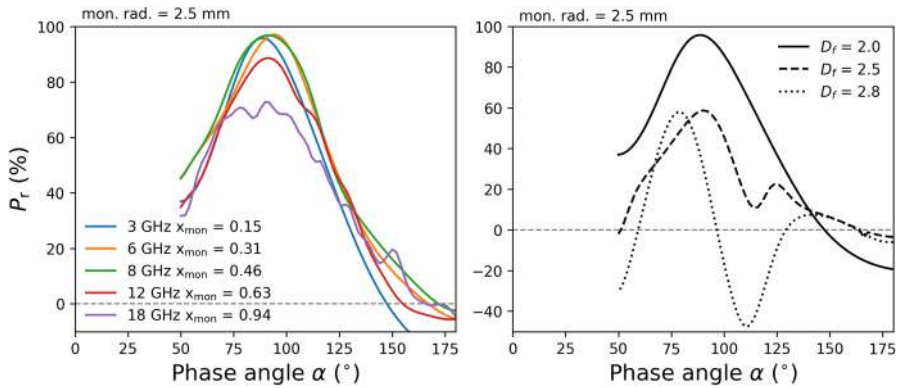


Fig. 26 Left: effect of monomer size (X_{MON} spanning from 0.15 to 0.94) on the polarisation phase curve for a single aggregate $D_f = 2$, $R_g = 17.03$ and $R_m = 26$. Right panel: effect of fractal dimension for $x_{\text{mon}} = 0.63$ (after Tobon Valencia et al. (2022))

6.4.1 Regolith grains' composition effect

Figure 28, left panel, displays the measured NPBs of particulate surfaces consisting of micron-size fayalite, forsterite, and spinel dust grains. The experimental data are obtained at the POLarimeter and ICE samples (POLICES) at the University of Bern (Spadaccia et al. 2022). Table 5 displays the main characteristics of the constituent particles and DLP features. As shown, the NPB becomes shallower as particulate reflectance increases as is the case for the spinel surface. By contrast, fayalite, the surface consisting of darker grains at the experiment wavelength, shows a deeper and narrower NPB. Multiple scattering by a surface consisting of large absorbing grains is limited to the first few orders. In that case, the NPB is mainly produced by the coherent double-scattering mechanism (see, e.g., Shkuratov 1989; Muinonen et al. 1989; Videen 2002; Grynko et al. 2022). Low-absorbing particulate surfaces produce a shallower NPB and higher inversion angle. Incoherent multiple scattering within the high-albedo media suppresses features of single scattering. The effect of surface reflectance is also presented by Shkuratov et al. (2004), as shown in Fig. 28, right panel. The particulate surface consisting of red clay particles produces a deeper negative polarisation branch as the albedo gets lower values (blue light).

6.4.2 Regolith grains size effect

It is known that the polarisation phase curve of particulate surfaces is up to some extent a remnant of the NPB produced by the constituent particles under single-scattering conditions (Shkuratov et al. 2006; Lvasseur-Regourd et al. 2015). As presented in the previous sections, the polarisation phase curve under single-scattering conditions is highly dependent on the scattering size regime. Ovcharenko et al. (2006) and Nelson et al. (2018) present a detailed study on the grain size effect on the negative polarisation branch of particulate surfaces. They use powder samples



Fig. 27 3D-printed aggregates with $N = 74$ monomers, each with radius $r = 2.5$ mm. Fractal dimension values equal to 2, 2.5, and 2.8 in the left, centre, and right panels, respectively

spanning over a broad size range. In Fig. 29, we present the $P_r(\alpha)$ curves for particulate surfaces consisting of very absorbing (boron carbide) and very bright (alumina) dust grains. The experimental data were obtained with the small phase angle and large phase-angle photopolarimeters located at the Astronomical Institute of Kharkov National University. They used an incandescent light with a wide-band filter centred at $0.63 \mu\text{m}$ as a light source. Left, middle, and right panels display three-grain size ranges. In the case of bright powders with size parameter $2\pi\lambda \sim 10$ (alumina, left panel), the NPB is broad and shallow ($P_{\min} \sim 0.15\%$). The dark boron carbide exhibits a deeper NPB ($P_{\min} \sim 0.7\%$) and a smaller inversion angle. As powder particle size increases (middle and right panels), the NPB for the dark Boron Carbide surface becomes narrower and deeper, whereas the corresponding NPB for the alumina powder becomes shallower. As explained in the previous section, in the case of large absorbing constituent particles, the CBM plays an important role, whilst in the case of bright large particles, incoherent multiple (diffuse) scattering dominates.

6.4.3 Particulate media morphology effect: compact vs porous regoliths

The effect of various degrees on compression of the particulate surface is studied by Shkuratov et al. (2006). The powder samples are located on free fall on a 20 mm-diameter sample cup. The sample thickness (3–4 mm) must be high enough to consider the sample as a semi-infinite layer. In the second step, the samples are compacted with a glass plate decreasing the sample porosity by a factor of two. The measured polarisation curves for the uncompressed and compressed surfaces are compared with those of the same samples in aerosol form obtained at the Amsterdam light-scattering instrument (Hovenier 2000; Volten et al. 2001). The polarisation phase curves for uncompressed surfaces (open symbols) show similar shapes as the corresponding samples under single-scattering conditions (filled symbols). This seems to indicate that P_{\max} for uncompressed particulate surfaces could be dominated by single-particle scattering. The bright uncompressed surface (Fig. 30, left panel) shows a nearly zero P_{\max} . Light that is multiply scattered within the porous surface becomes nearly unpolarized. After compression, P_{\max} significantly increases and it is shifted towards larger phase angles. The effect is even stronger in the case of the dark surface (Fig. 30, right panel). Powder compression produces smooth surfaces. Under some conditions, the compressed surface may scatter light as a nearly plane surface

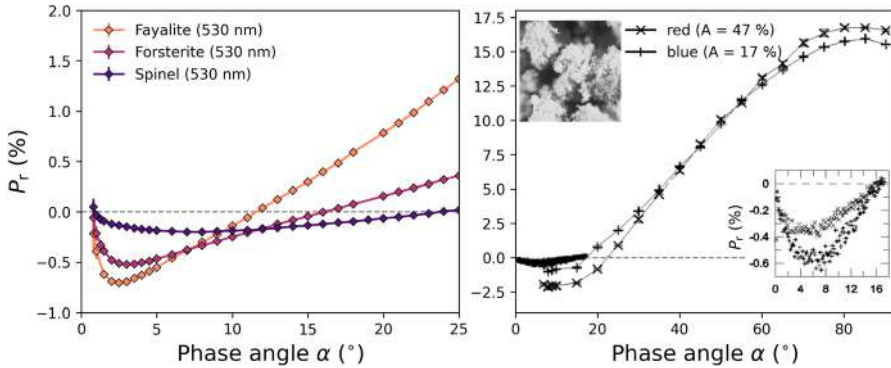


Fig. 28 Left panel: experimental negative polarisation branch for three particulate surfaces consisting of fayalite, forsterite, and spinel at 530 nm (Spadaccia et al. 2022). Right panel: degree of linear polarisation curves for red clay at blue and red wavelengths. Large and small symbols correspond to experimental data under single scattering conditions and particulate surfaces, respectively. A small figure at the bottom right corner zooms in on the measured NPB for the particulate surface shown in the SEM image (top left corner). Figure adapted from Shkuratov et al. (2004)

Table 5 Measured main parameters of the P_r curves for fractal particulate surfaces as a function of particulate size, colour, and packing density. Data from Shkuratov et al. (2004), Ovcharenko et al. (2006), Shkuratov et al. (2006), and Spadaccia et al. (2022)

Sample	Grain Size	Reflectance/albedo	P_{min} (%)	α_{min} (°)	α_{inv} (°)
Fayalite	< 15 μm	0.158 ± 0.004	-0.70	2.5	12
Forsterite	< 15 μm	0.758 ± 0.014	-0.53	3	17
Spinel	< 15 μm	0.822 ± 0.03	-0.20	8	24
Boron Carbide	1.5 μm	A = 6.8%	-0.7	4	14
Boron Carbide	8.5 μm	A = 6.6%	-1.0	1	8
Boron Carbide	15 μm	A = 7.1%	-1.3	0.5	8
Alumina	1.5 μm	A = 99%	-0.15	10	19
Alumina	6 μm	A = 95%	-0.15	10	19
Alumina	11.5 μm	A = 91%	-0.15	2	13
Red clay (blue)	1.5 μm	A = 17%	-0.7	6	16
Red clay (red)	1.5 μm	A = 47%	-0.4	7	16

(Shkuratov et al. 2007). If that is the case, the polarised reflected light is described by the Fresnel equations for reflection.

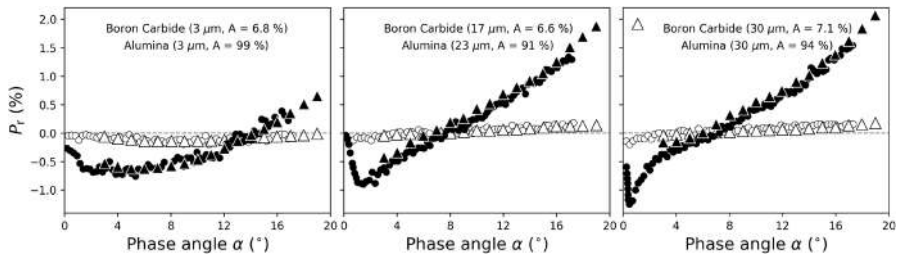


Fig. 29 Polarisation-phase curves for three particle-size ranges: left: 3 μm ; middle 17 μm –23 μm , and right: 30 μm . Open symbols correspond to Alumina and filled symbols to Boron Carbide. The corresponding sample Albedo is included in the figures. Figures adapted from Ovcharenko et al. (2006)

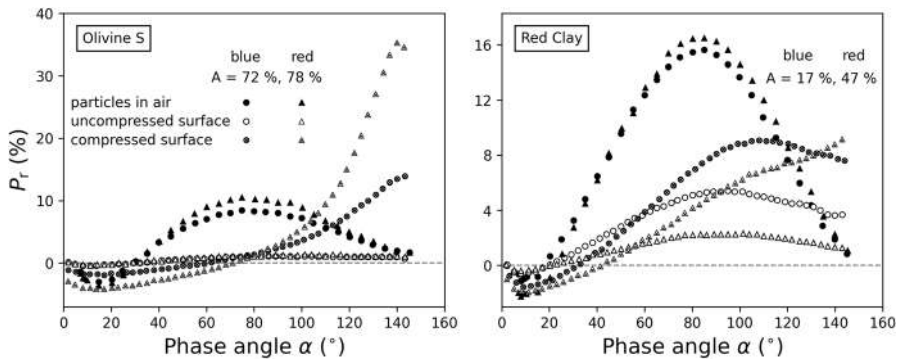


Fig. 30 Polarisation-phase curves for aerosol particles (filled symbols) and particulate surfaces uncompressed (open symbols) and compressed (crossed symbols). Triangles and circles correspond to the measured data at 442 nm and 633 nm, respectively. Figures adapted from Shkuratov et al. (2007)

Appendix A: Observing techniques

In Sect. 1, we highlighted that understanding the significance of observational data simply requires keeping in mind the definition of the quantity P_r given by Eq. (1). However, to carry out polarimetric observations, to estimate their associated errors, or simply to critically evaluate the reliability of a result, one needs a more in-depth understanding of the observation and data reduction techniques. In this section, we provide some basic concepts.

A.1: Definitions

The definition of the Stokes parameters requires the choice of a reference direction in the plane perpendicular to the direction of propagation of the radiation. Figure 31 illustrates the operational definitions that we adopt in this paper, according to which (e.g., Landi Degl’Innocenti et al. 2007)

$$\begin{aligned}
 I &= k(S_0 + S_{90}) \\
 Q &= k(S_0 - S_{90}) \\
 U &= k(S_{45} - S_{135}) \\
 V &= k(S_{RH} - S_{LH}),
 \end{aligned}
 \tag{A1}$$

where k is a constant, S_β is the flux measured behind a linear polariser rotated over an angle β with respect to the reference direction; β is measured positive counterclockwise from the reference direction to the acceptance axis of the polariser, looking towards the source. S_{RH} (S_{LH}) is the flux measured by a detector behind a filter transparent only to the right-handed (left-handed) circularly polarised light. Light is called right-handed (left-handed) circularly polarised when the tip of the radiation's electric field vector rotates clockwise (counterclockwise), looking towards the source. We nearly always use the relative quantities

$$P_X = X/I \tag{A2}$$

($X = Q, U, V$), so that the calibration of the constant k becomes irrelevant. The quantities P_X are often called 'reduced Stokes parameters'. As an alternative to P_Q and P_U , linear polarisation can also be described in terms of the fraction of linear polarisation P_L and the angle of maximum polarisation Θ , such that

$$\begin{aligned}
 P_L &= \left(P_Q^2 + P_U^2 \right)^{1/2} \\
 P_Q &= P_L \cos(2\Theta) \\
 P_U &= P_L \sin(2\Theta),
 \end{aligned}
 \tag{A3}$$

where Θ is measured positive rotating counterclockwise from the reference direction to the direction of maximum polarisation, looking towards the source. We note that the definitions of Stokes parameters, including the sign convention as defined above, are not universal; comments on this confusing situation can be found in various articles (e.g., Clarke 1974; Landi Degl'Innocenti et al. 2007; di Serego Alighieri 2019; Bagnulo and Landstreet 2020), but at least the definition of P_r given by Eq. (1) is widely accepted.

Stellar astronomers generally adopt the great circle through the observed object and the North Celestial Pole as the reference direction. However, for observations of Solar System objects (except the Sun), the adopted reference direction is usually the one perpendicular to the scattering plane. The position angle Φ of the scattering plane (measured by rotating counterclockwise from the great circle passing through the object and the North Celestial Pole to the great circle passing through the object and the Sun) can be found from the ephemeris, or obtained from the relation

$$\sin \delta_T \cos(\alpha_\odot - \alpha_T) = \cos \delta_T \tan \delta_\odot - \sin(\alpha_\odot - \alpha_T) \frac{1}{\tan \Phi}, \tag{A4}$$

where (α_T, δ_T) are the object (target) RA and DEC coordinates in the equatorial

system, and $(\alpha_{\odot}, \delta_{\odot})$ the Sun coordinates in the same system. When the polarisation is measured with an instrument that is not aligned with the direction perpendicular to the scattering plane, one can rotate the measured Stokes parameters to that direction using

$$\begin{aligned} P_Q &= P'_Q \cos(2\theta) + P'_U \sin(2\theta) \\ P_U &= -P'_Q \sin(2\theta) + P'_U \cos(2\theta), \end{aligned} \quad (\text{A5})$$

where P'_Q and P'_U are measured in the instrument reference system, and θ is the angle by which the old reference system must rotate (counterclockwise looking at the source) to coincide with the new reference system; hence, $\theta = -\chi + \Phi + \pi/2$; where χ is the angle of the instrument reference direction measured rotating counterclockwise from the great circle through the target and the north celestial pole.³

After this rotation, $P_r = P_Q$ represents the flux perpendicular to the scattering plane minus the flux parallel to that plane, divided by the sum of the two fluxes (see Eq. 1), and, for symmetry reasons, for a point source $P_U = 0$. In the new reference system, we also have

$$\begin{aligned} P_L &= P'_L \\ \Theta &= \Theta' - \theta, \end{aligned} \quad (\text{A6})$$

where P'_L and Θ' are, respectively, the fraction of linear polarisation and its position angle measured in the instrument reference system. If $P_U = 0$, then we expect $P_r = \pm P'_L$, depending on the value of Θ : the sign is positive when $\Theta = 0^\circ$, and negative when $\Theta = 90^\circ$. When using P_L instead of P_Q , one should bear in mind that the distribution of its estimate is not Gaussian, and that a bias is introduced unless $\sigma_p \ll P_L$. There are formulas that can be used to correct for this bias, for instance (Wardle and Kronberg 1974)

$$P_L = P \left[1 - \left(\frac{\sigma_P}{P} \right)^2 \right]^{\frac{1}{2}}, \quad (\text{A7})$$

where P is the measured value of the fraction of linear polarisation.

A.2: How polarisation is measured

Comprehensive reviews of various instrument configurations and hardware solutions can be found in, e.g., Serkowski (1974) and Keller et al. (2015). Here, we will only discuss the basic concepts and explain how instrumental effects can be minimised.

A.2.1: Polarimetry with linear polarisers only

The signal received by a detector behind a polarising filter with acceptance axis rotated by an angle β with respect to the reference direction is given by

³ The instrument position angle is usually recorded in the image fits-headers, but not necessarily following this sign convention.

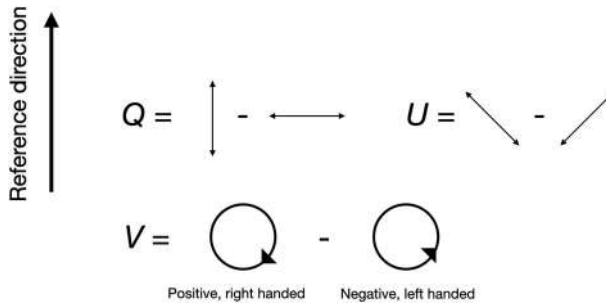


Fig. 31 The operational definitions of the Stokes parameters. The observer is looking towards the source of the radiation. Image adapted from Landi Degl’Innocenti et al. (2007)

$$S_{\beta} = \frac{1}{2}k[I + Q \cos(2\beta) + U \sin(2\beta)] \quad (\text{A8})$$

(e.g., Serkowski 1974; Hansen and Travis 1974). A simple method for performing astronomical polarimetry is to obtain a series of observations using a linear polariser with its acceptance axis set at four different position angles β as per definition of Eq. (A3). If it is necessary to minimise the number of exposures, or the number of rotations of optical elements, three position angles can be used instead. Maximum efficiency is achieved by separating these positions by 60° . The reduced Stokes parameters are then derived from

$$I = \frac{2}{3k}(S_0 + S_{60} + S_{120}) \quad (\text{A9})$$

$$P_Q = \frac{2S_0 - S_{60} - S_{120}}{S_0 + S_{60} + S_{120}} \quad (\text{A10})$$

$$P_U = \sqrt{3} \frac{S_{60} - S_{120}}{S_0 + S_{60} + S_{120}}. \quad (\text{A11})$$

This optical scheme is employed on the Hubble Space Telescope, and discussed in detail by Sparks and Axon (1999). From ground-based measurements, the major drawback of using a temporal sequence with a rotating polariser is that even small changes in sky transparency between subsequent observations may create a spurious polarisation signal. This problem can be minimised only if the instrument field of view is sufficiently wide to capture a number of nearby (and presumably unpolarised) stars, which can be used as calibrators.

An alternative, and most commonly adopted solution, is to employ a beam-splitting device, such as a Wollaston prism, which is capable of splitting the incoming radiation into two beams that are polarised perpendicularly to each other. With such a device, the fluxes that one has to measure to determine a Stokes parameter are captured simultaneously, and changes in the sky transparency can be

removed from the polarisation measurement. For instance, an instrument can record simultaneously $S(\beta = 0) = I + Q$ and $S(\beta = 90^\circ) = I - Q$. Then, after a 45° rotation, it can measure $S(\beta = 45^\circ) = I + U$ and $S(\beta = 135^\circ) = I - U$. Instrument rotation may be avoided by adopting a double-wedged Wollaston (Oliva 1997), a device made of two Wollaston prisms glued together that splits the incoming radiation into four beams, containing the light polarised at 0° , 45° , 90° , and 135° with respect to its principal axis. The possibility to measure simultaneously P_Q and P_U is useful for polarimetry of rapidly transient phenomena, or whenever it is preferable to avoid rotations of the instrument, or of parts of it.

We note that when a beam-splitting device is used for polarimetry of spatially extended objects, it is necessary to employ a mask to prevent the two beams from overlapping, as proposed, for instance, by Scarrott et al. (1983), and adopted in the FORS instrument (Appenzeller et al. 1998) on the VLT/ESO.

A.2.2: The beam-swapping technique

The optical designs described above require that observations come with accurate flat-fielding calibrations; experience shows that, because accurate flat-fielding calibration is difficult to achieve, it is generally not possible to reach an accuracy better than $\sim 0.1\%$ on objects that are intrinsically polarised at about 1–2% level (e.g. Bendjoya et al. 2022). The measurement accuracy may be substantially improved by adopting the so-called *beam-swapping technique*. Using the same part of a detector to measure opposite polarisation signals, this technique eliminates various potential systematic effects arising from the detector and the polarimetric optics. What is needed for its implementation is a modulator placed in front of a beam-splitting device. A modulator, such as a retarder waveplate, is an optical device that introduces a phase-shift γ between the two perpendicular components of the radiation's electric field. Most commonly used are a $\lambda/2$ retarder waveplate, that introduces a 180° phase shift, and a $\lambda/4$ retarder waveplate, that introduces a 90° phase shift.

A $\lambda/2$ retarder rotates the polarisation plane of the incoming radiation by an angle 2δ , where δ defines the orientation of the retarder's fast axis with respect to a given direction, and it is often used to measure linear polarisation. A $\lambda/4$ retarder transforms circular polarisation into linear polarisation, and may be used to measure circular polarisation. It can be demonstrated (Serkowski 1974; Landi Degl'Innocenti and Landolfi 2004) that the signal S measured by a detector behind a retarder and a polariser is given by

$$\begin{aligned}
 S(\delta, \beta, \gamma) \propto & \\
 & \frac{1}{2} \left\{ I + [Q \cos 2\delta + U \sin 2\delta] \cos(2\beta - 2\delta) - \right. \\
 & [Q \sin 2\delta - U \cos 2\delta] \sin(2\beta - 2\delta) \cos \gamma + \\
 & \left. V \sin(2\beta - 2\delta) \sin \gamma \right\}. \tag{A12}
 \end{aligned}$$

It is trivial to see that, in the ideal case, by defining

$$G(\delta, \gamma) = \frac{S(\delta, 0^\circ, \gamma) - S(\delta, 90^\circ, \gamma)}{S(\delta, 0^\circ, \gamma) + S(\delta, 90^\circ, \gamma)}, \tag{A13}$$

one can measure the Stokes parameters by giving the retarders various orientations, for example

$$\begin{aligned}
 P_Q &= G(\delta = 0, \gamma = \pi) &= -G(\delta = 45^\circ, \gamma = \pi) &= G(\delta = 90^\circ, \gamma = \pi) &= \dots \\
 P_U &= G(\delta = 22.5^\circ, \gamma = \pi) &= -G(\delta = 67.5^\circ, \gamma = \pi) &= G(\delta = 112.5^\circ, \gamma = \pi) &= \dots
 \end{aligned} \tag{A14}$$

In a real polarimeter, various factors can influence the measurements. For instance, the position angle δ and the retardation γ depend on wavelength λ , and the detector is often not calibrated well enough to ensure that the two beams are recorded with identical efficiency. Fortunately, a technique based on rotating the waveplate helps cancel most of these spurious effects. When the $\lambda/2$ retarder waveplate is rotated by 45° , the measured polarisation changes sign, whilst most instrumental effects remain unaffected. These effects cancel out if the reduced Stokes parameters are derived from the double differences

$$\begin{aligned}
 P_Q &= \frac{1}{2} [G(\delta = 0, \gamma = \pi) - G(\delta = 45^\circ, \gamma = \pi)] \\
 P_U &= \frac{1}{2} [G(\delta = 22.5^\circ, \gamma = \pi) - G(\delta = 67.5^\circ, \gamma = \pi)].
 \end{aligned} \tag{A15}$$

Alternative observational strategies involve setting the retarder waveplate at additional position angles, or even having it continuously rotating. An alternative method to recombine fluxes, practically equivalent to Eq. (A15), is by applying the formulas of the double ratio method, for which we refer to Sect. 4.2 and App. A.2 of Bagnulo et al. (2009).

In the following, we discuss some important residual effects not corrected by the beam-swapping technique.

A.2.3: Chromatism of the retarder waveplate

The position angle δ of a modulator may depend on the wavelength λ , and its effects are not cancelled out by the beam-swapping technique (see Sect. 7.2 of Bagnulo et al. 2009, and Patat and Taubenberger 2011). Without calibrating for chromatism, the measured polarisation angle will be offset from its true value; for instance, a constant polarisation position angle may appear to vary with λ . Calibration can be performed using either laboratory measurements or observations of a celestial object with a constant position angle (e.g., an asteroid). This calibration is not necessary if the quantity of interest is the fraction of linear polarisation P_L of Eq. (A3), because the chromatism effect influences both P_Q and P_U , and cancels out in the expression $P_Q^2 + P_U^2$.

A.2.4: Cross-talk from linear to circular polarisation

Compared to linear polarisation, only a very small fraction of circular polarisation is produced by scattering from particles or surfaces, and only in very specific, but interesting circumstances. For example, due to homochirality, light diffused by organic material is expected to produce circular polarisation, and this has indeed been observed in laboratory measurements (Wolstencroft 1974; Sparks et al. 2009; Sterzik et al. 2010). Attempts to search for bio-signatures with circular polarisation on celestial bodies have been made (e.g., Sparks et al. 2005), but the predicted signal is small ($\sim 10^{-4}$ or less), and astronomical observations may not reach the S/N necessary to detect it. Systematic errors may be caused by cross-talk from linear to circular polarisation if the target bodies for the circular polarisation measurements are linearly polarised, because the telescope and/or instrument optics may transform part of the linear polarisation signal into circular polarisation. This effect was noted in FORS1 data (Bagnulo et al. 2009), and was further analysed using FORS2 data by Siebenmorgen et al. (2014).

A.3: Observing techniques and data reduction

Hereafter, we will consider the optical scheme proposed by Appenzeller (1967), that was adopted in the FORS instrument on the VLT/ESO. This scheme consists of a retarder waveplate that can be set to fixed position angles, followed by a Wollaston prism, and a CCD. Most of the following considerations can be applied to other instrument configurations.

A.3.1: Broadband polarimetry

With 'broadband polarimetry', we refer to the measurement of the polarisation of a source integrated over the wavelength range of a filter passband. This technique relies on photometry of images obtained in opposite polarisation directions, which are then combined using for instance Eqs. (A15). There is a rich literature about the best techniques to estimate the flux of a point source in a CCD image, but simple aperture

photometry is usually well suited for polarimetric measurements. Basically, the quantities P_Q and P_U are plotted as functions of the aperture size. The best P_Q and P_U are then selected as the plateau values. The plateau is generally reached at aperture values for which the fluxes are still increasing (see Fig. 32). Visual inspection of these curves can help to determine whether background objects are affecting the measurement at specific apertures (for more details, see Bagnulo et al. 2016).

A.3.2: Polarimetric maps

For spatially extended objects like planets or cometary comae, it may be interesting to obtain polarimetric maps, and to correlate them with intensity and colour maps. Instead of combining the fluxes measured in relatively large apertures as described in Sect. A.3, one can combine the flux from one or a few pixels, associating the resulting polarisation values to positions in space. Background subtraction may require special attention if the object occupies a significant fraction of the field of view, and if the instrument suffers from instrumental polarisation that is variable across the field of view, as in the case of the FORS instrument (Patat and Romaniello 2006; González-Gaitán et al. 2020). In addition, polarimetric maps may well be affected by systematics due to changes in seeing between exposures, differences in the PSF of the two beams, and centring issues. These issues are discussed in detail by Gray et al. (2024a) (see also Sect. 4.4).

A.3.3: Spectropolarimetry

Spectra may be combined using the same formulae employed for broadband polarimetry. The main difference is that the (wavelength-dependent) background can only be estimated from strips parallel to the beams, rather than in extended regions around the source, as is possible in imaging mode. Background subtraction can be challenging if a Wollaston mask restricts the size of the strips used for estimating its contribution, and if the instrumental polarisation varies across the instrument's field of view. A detailed discussion of this issue (for the case of circular polarisation spectra) is presented in Sect. 6 of Bagnulo and Landstreet (2020). Another complication is that it is often impractical to determine how the polarisation spectra change with increasing extraction aperture (see Fig. 32). Consequently, it is more difficult to estimate the best choice for the aperture size than it is in the case of imaging polarimetry of point sources. This limitation may affect the accuracy of the measurements.

A.4: Quality checks

If there is confidence that the polarisation of an object is either parallel or perpendicular to the scattering plane, and if the instrument can be conveniently rotated, telescope time can be concentrated on measuring only one Stokes parameter. A small misalignment between the instrument's position angle and the scattering

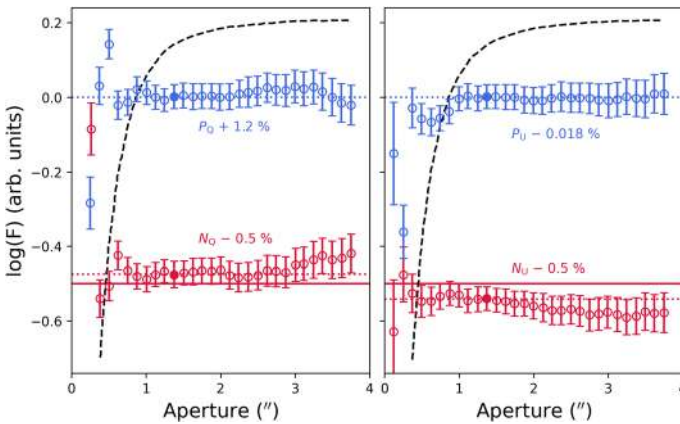


Fig. 32 In the left panel, the blue empty circles show P_Q as a function of the aperture used for the flux measurement, with their error bars calculated from photon noise and background subtraction, and offset to the adopted value. The solid symbols show the value finally adopted to estimated Stokes P_Q (1.2%) and its null parameters parameter, offset to -0.5% for display purpose. The black solid line shows the logarithm of the total flux expressed in arbitrary units, demonstrating that polarimetric measurements converge at smaller aperture values than photometric measurements. The right panel refers to P_U

plane may reduce the S/N, but will not introduce a systematic offset, as long as the misalignment is known, as we can apply the following correction:

$$P_r = \frac{1}{\cos(2\xi)} P'_Q, \tag{A16}$$

where ξ is the offset of the instrument’s position angle with respect to the direction perpendicular to the scattering plane and P'_Q is the value measured in the instrument reference system. This strategy can either save half of the telescope time or increase the S/N by a factor of $\simeq \sqrt{2}$ assuming all shutter time is used to measure only one Stokes parameter. *Vice versa*, when both Stokes parameters are measured, the P_U value can serve as a quality check, if for symmetry reasons it is expected to be zero. For example, the results of a survey could be supported by a plot showing the distribution of P_U/σ_U , which should resemble a Gaussian centred about zero with $\sigma = 1$ (see, e.g., Fig. 1 of Bagnulo et al. 2008).

Another quality check can be performed if a Stokes parameter is obtained from two or more pairs of exposures. When a Stokes parameter is measured from numerous pairs of exposures, it is natural to compute the external error (the mean quadratic error), which provides a more realistic estimate than the internal error derived from an *a priori* propagation. If a Stokes parameter is obtained as the average of only two pairs of exposures, then it is still possible to consider the difference between the estimates from each of the two pairs, which should be zero within the uncertainties. In case of broadband polarimetric measurements, this difference may be called “null parameter” (see Fig. 32). In case of spectropolarimetric observations, the difference between two spectra is called the ‘null profile’ (e.g., Donati et al.

1997). The distribution of the difference between the P_Q values for each wavelength bin, normalised by the uncertainties, should be similar to a Gaussian centred about zero, and with $\sigma = 1$.

These types of quality checks are also useful when calculating polarimetric maps. Both P_U maps and null maps should appear as random noise centred about zero. However, it must be taken into account that whilst systematic deviations from zero may indicate potential issues with the observations (or source variability), the consistency of the null parameters with zero does not necessarily guarantee that the measurement results are correct.

Acknowledgements O.M. acknowledges financial support from grant PID2021-1233700B-I00 (CATS) funded by MCIN/AEI/10.13039/501100011033 and the Severo Ochoa grant CEX2021-001131-S funded by MCIN/AEI/10.13039/501100011033. I.B. acknowledges financial support from the National Research Foundation of Ukraine (Project N2020.02/0371).

Author Contributions Authors' contributions: All authors contributed to all aspects of this review, but mainly responsible for each section are as follows: Intro and App. A: SB; Sect. 2: AC; Sect. 3: IB; Sect. 4: IGK; Sect. 5: DMS; Sect. 6: OM. All original figures of this review have been made by YGK.

Open Access This article is licensed under a Creative Commons Attribution-NonCommercial-NoDerivatives 4.0 International License, which permits any non-commercial use, sharing, distribution and reproduction in any medium or format, as long as you give appropriate credit to the original author(s) and the source, provide a link to the Creative Commons licence, and indicate if you modified the licensed material. You do not have permission under this licence to share adapted material derived from this article or parts of it. The images or other third party material in this article are included in the article's Creative Commons licence, unless indicated otherwise in a credit line to the material. If material is not included in the article's Creative Commons licence and your intended use is not permitted by statutory regulation or exceeds the permitted use, you will need to obtain permission directly from the copyright holder. To view a copy of this licence, visit <http://creativecommons.org/licenses/by-nc-nd/4.0/>.

References

- Aben I, Helderma F, Stam DM et al (1999) Spectral fine-structure in the polarisation of skylight. *Geophys Res Lett* 26(5):591–594. <https://doi.org/10.1029/1999GL900025>
- Aben I, Stam DM, Helderma F (2001) The ring effect in skylight polarisation. *Geophys Res Lett* 28(3):519–522. <https://doi.org/10.1029/2000GL011901>
- Afanasiev VL, Rosenbush VK, Kiselev NN (2014) Polarimetry of major Uranian moons at the 6-m telescope. *Astrophys Bull* 69(2):211–223. <https://doi.org/10.1134/S1990341314020096>
- Agarwal J, Kim Y, Kelley MSP, et al (2024) Dust emission and dynamics. In: Meech KJ, Combi MR, Bockelée-Morvan D, et al (eds) *Comets III*. University of Arizona Press, Tucson, [arXiv:2309.12759](https://arxiv.org/abs/2309.12759)
- A'Hearn MF, Millis RC, Schleicher DO et al (1995) The ensemble properties of comets: Results from narrowband photometry of 85 comets, 1976–1992. *Icarus* 118(2):223–270. <https://doi.org/10.1006/icar.1995.1190>
- Anguiano-Arteaga A, Pérez-Hoyos S, Sánchez-Lavega A et al (2021) Vertical distribution of aerosols and hazes over Jupiter's great red spot and its surroundings in 2016 from HST/WFC3 imaging. *J Geophys Res Planets* 126(11):e06996. <https://doi.org/10.1029/2021JE006996>
- Appenzeller I (1967) A new polarimeter for faint astronomical objects. *PASP* 79:136. <https://doi.org/10.1086/128454>
- Appenzeller I, Fricke K, Fürtig W et al (1998) Successful commissioning of FORS1—the first optical instrument on the VLT. *The Messenger* 94:1–6

- Arago F (1820) Quelques nouveaux details sur la passage de la comète découverte dans le mois de juillet 1819, devant le disque du soleil. *Ann Chim Phys*, Ser 2 13:104–110. <https://gallica.bnf.fr/ark:/12148/bpt6k65690085/f110.image>
- Arnold JA, Kalume A, Yu H et al (2022) Measurements of elastic light-scattering patterns and images of single, oriented, optically trapped particles. *JQSRT* 287:108223. <https://doi.org/10.1016/j.jqsrt.2022.108223>
- Avramchuk VV, Rakhimov VI, Chernova GP et al (1992) Photometry and polarimetry of Pluto near its perihelion position. I. *Kinem Fiz Neb Tel* 8(4):37–45
- Bagnulo S, Landstreet JD (2020) Discovery of six new strongly magnetic white dwarfs in the 20 pc local population. *A&A* 643:A134. <https://doi.org/10.1051/0004-6361/202038565>. arXiv:2010.05795 [astro-ph.SR]
- Bagnulo S, Szeifert T, Wade GA et al (2002) Measuring magnetic fields of early-type stars with FORS1 at the VLT. *A&A* 389:191–201. <https://doi.org/10.1051/0004-6361:20020606>
- Bagnulo S, Boehnhardt H, Muinonen K, et al (2006) Exploring the surface properties of transneptunian objects and Centaurs with polarimetric FORS1/VLT observations. *A&A* 450(3):1239–1248. <https://doi.org/10.1051/0004-6361:20054518>, arXiv:astro-ph/0601414 [astro-ph]
- Bagnulo S, Belskaya I, Muinonen K et al (2008) Discovery of two distinct polarimetric behaviours of trans-Neptunian objects. *A&A* 491(2):L33–L36. <https://doi.org/10.1051/0004-6361:200810938>. arXiv:0810.2714 [astro-ph]
- Bagnulo S, Landolfi M, Landstreet JD et al (2009) Stellar spectropolarimetry with retarder waveplate and beam splitter devices. *PASP* 121(883):993. <https://doi.org/10.1086/605654>
- Bagnulo S, Tozzi G, Boehnhardt H et al (2010) Polarimetry and photometry of the peculiar main-belt object 7968 = 133P/Elst-Pizarro. *A&A* 514:A99
- Bagnulo S, Cellino A, Sterzik M (2015) Linear spectropolarimetry: a new diagnostic tool for the classification and characterization of asteroids. *MNRAS Lett* 446:L11–L15
- Bagnulo S, Belskaya I, Stinson A et al (2016) Broadband linear polarization of Jupiter Trojans. *A&A* 585: A122. <https://doi.org/10.1051/0004-6361/201526889>. arXiv:1511.09271 [astro-ph.EP]
- Bagnulo S, Cellino A, Kolokolova L et al (2021) Unusual polarimetric properties for interstellar comet 2I/Borisov. *Nat Commun* 12:1797. <https://doi.org/10.1038/s41467-021-22000-x>
- Bagnulo S, Gray Z, Granvik M et al (2023) Optical spectropolarimetry of binary asteroid Didymos-Dimorphos before and after the DART impact. *ApJL* 945(2):L38. <https://doi.org/10.3847/2041-8213/abc261>. arXiv:2303.11776 [astro-ph.EP]
- Bandermann LW, Kemp JC, Wolstencroft RD (1972) Circular polarization of light scattered from rough surfaces. *MNRAS* 158:291. <https://doi.org/10.1093/mnras/158.3.291>
- Barthelemy M, Lystrup MB, Menager H et al (2011) Is the Jovian auroral H3+ emission polarised? *A&A* 530:A139. <https://doi.org/10.1051/0004-6361/201014314>
- Bazzon A, Schmid HM, Gislis D (2013) Measurement of the earthshine polarization in the B, V, R, and I bands as function of phase. *A&A* 556:A117. <https://doi.org/10.1051/0004-6361/201321855>. arXiv:1306.1218 [astro-ph.EP]
- Bazzon A, Schmid HM, Buenzli E (2014) HST observations of the limb polarization of Titan. *A&A* 572: A6. <https://doi.org/10.1051/0004-6361/201323139>. arXiv:1409.3421 [astro-ph.EP]
- Belskaya I (2020) Polarimetry of Transneptunian Objects and Centaurs V1.0. NASA Planetary Data System p 1. <https://doi.org/10.26033/8mqj-m072>
- Belskaya I, Shevchenko V (2000) Opposition effect of asteroids. *Icarus* 147:94–105
- Belskaya I, Shkuratov Y, Efimov Y et al (2005) The F-type asteroids with small inversion angles of polarization. *Icarus* 178:213–221
- Belskaya I, Bagnulo S, Muinonen K et al (2008) Polarimetry of the dwarf planet (136199) Eris. *A&A* 479 (1):265–269. <https://doi.org/10.1051/0004-6361:20078241>. arXiv:0711.4974 [astro-ph]
- Belskaya IN, Levasseur-Regourd AC, Shkuratov YG et al (2008) Surface Properties of Kuiper Belt Objects and Centaurs from Photometry and Polarimetry. In: Barucci MA, Boehnhardt H, Cruikshank DP et al (eds) *The Solar System Beyond Neptune*. University of Arizona Press, Tucson, pp 115–127
- Belskaya IN, Levasseur-Regourd AC, Cellino A et al (2009) Polarimetry of main belt asteroids: wavelength dependence. *Icarus* 199(1):97–105. <https://doi.org/10.1016/j.icarus.2008.09.010>
- Belskaya IN, Bagnulo S, Barucci MA et al (2010) Polarimetry of Centaurs (2060) Chiron, (5145) Pholus and (10199) Chariklo. *Icarus* 210(1):472–479. <https://doi.org/10.1016/j.icarus.2010.06.005>
- Belskaya IN, Bagnulo S, Stinson A et al (2012) Polarimetry of trans-Neptunian objects (136472) Makemake and (90482) Orcus. *A&A* 547:A101. <https://doi.org/10.1051/0004-6361/201220202>. arXiv:1209.6025 [astro-ph.EP]

- Belskaya I, Fornasier S et al (2017) Refining the asteroid taxonomy by polarimetric observations. *Icarus* 284:30–42
- Belskaya I, Berdyugin A, Krugly Y et al (2022) Polarimetry of M-type asteroids in the context of their surface composition. *A&A* 663:A146. <https://doi.org/10.1051/0004-6361/202142784>. arXiv:2204.04929 [astro-ph.EP]
- Bendjoya P, Cellino A, Rivet JP et al (2022) The Calern Asteroid polarisation survey. An updated catalogue of asteroid polarimetric data. *A&A* 665:A66. <https://doi.org/10.1051/0004-6361/202142960>
- Bertaux JL, Nevejans D, Korablev O et al (2007) SPICAV on venus express: three spectrometers to study the global structure and composition of the Venus atmosphere. *Planet Space Sci* 55(12):1673–1700. <https://doi.org/10.1016/j.pss.2007.01.016>
- Blum J (2006) Dust agglomeration. *Adv Phys* 55:881–947. <https://doi.org/10.1080/00018730601095039>
- Boehnhardt H, Bagnulo S, Muinonen K et al (2004) Surface characterization of 28978 Ixion (2001 KX₇₆). *A&A* 415:L21–L25. <https://doi.org/10.1051/0004-6361:20040005>
- Boehnhardt H, Tozzi G, Bagnulo S et al (2008) Photometry and polarimetry of the nucleus of comet 2P/Encke. *A&A* 489:1337–1343
- Böhren C, Huffman DR (1998) Absorption and scattering of light by small particles. Wiley. <https://doi.org/10.1002/9783527618156>
- Borisov G, Bagnulo S, Nikolov P et al (2015) Imaging polarimetry and spectropolarimetry of comet C/2013 R1 (Lovejoy). *Planet Space Sci* 118:187–192. <https://doi.org/10.1016/j.pss.2015.06.012>. arXiv:1601.02701 [astro-ph.EP]
- Borisov G, Devogèle M, Cellino A et al (2018) Rotational variation of the linear polarization of the asteroid (3200) Phaethon as evidence for inhomogeneity in its surface properties. *MNRAS* 480(1): L131–L135. <https://doi.org/10.1093/mnras/sly140>. arXiv:1807.11842 [astro-ph.EP]
- Bottke WF, Marschall R, Nesvorný D et al (2023) Origin and evolution of Jupiter’s Trojan asteroids. *Space Sci Rev* 219(8):83. <https://doi.org/10.1007/s11214-023-01031-4>. arXiv:2312.02864 [astro-ph.EP]
- Bowell E, Lumme K (1979) Colorimetry and magnitudes of asteroids. In: Gehrels T, Matthews MS (eds) *Asteroids*. University of Arizona Press, Tucson, pp 132–169
- Bowell E, Zellner B (1974) Polarizations of asteroids and satellites. In: Gehrels T (ed) *Planets, stars and nebulae studied with photopolarimetry*. University of Arizona Press, Tucson, pp 381–404
- Bowell E, West R, Heyer H, et al (1992) (4015) 1979 VA = Comet Wilson-Harrington (1949 III). *IAU Circ.*, No. 5585. Edited by Marsden, B. G
- Braak CJ, de Haan JF, Hovenier JW et al (2002) Galileo Photopolarimetry of Jupiter at 678.5 nm. *Icarus* 157(2):401–418. <https://doi.org/10.1006/icar.2002.6846>
- Braak CJ, de Haan JF, Hovenier JW et al (2002) Spatial and temporal variations of Venus haze properties obtained from Pioneer Venus Orbiter polarimetry. *J Geophys Res Planets* 107(E5):5029. <https://doi.org/10.1029/2001JE001502>
- Braga-Ribas F, Sicardy B, Ortiz JL et al (2014) A ring system detected around the Centaur (10199) Chariklo. *Nature* 508(7494):72–75. <https://doi.org/10.1038/nature13155>. arXiv:1409.7259 [astro-ph.EP]
- Breger M, Cochran WD (1982) Polarimetry of Pluto. *Icarus* 49(1):120–124. [https://doi.org/10.1016/0019-1035\(82\)90061-6](https://doi.org/10.1016/0019-1035(82)90061-6)
- Broadfoot AL, Kumar S, Belton MJS et al (1974) Mercury’s atmosphere from mariner 10: preliminary results. *Science* 185(4146):166–169. <https://doi.org/10.1126/science.185.4146.166>
- Brooke TY, Knacke RF, Joyce RR (1987) The near infrared polarization and color of comet P/Halley. *A&A* 187:621
- Brown ME (2016) The 3–4 μm Spectra of Jupiter Trojan Asteroids. *AJ* 152(6):159. <https://doi.org/10.3847/0004-6256/152/6/159>, arXiv:1606.03013 [astro-ph.EP]
- Burns JA, Lamy PL, Soter S (1979) Radiation forces on small particles in the Solar System. *Icarus* 40(1):1–48. [https://doi.org/10.1016/0019-1035\(79\)90050-2](https://doi.org/10.1016/0019-1035(79)90050-2)
- Burrows JP, Weber M, Buchwitz M et al (1999) The global ozone monitoring experiment (GOME): mission concept and first scientific results. *J Atmos Sci* 56(2):151–175. [https://doi.org/10.1175/1520-0469\(1999\)056<0151:TGOMEG>2.0.CO;2](https://doi.org/10.1175/1520-0469(1999)056<0151:TGOMEG>2.0.CO;2)
- Bus SJ, Binzel RP (2002) Phase II of the small main-belt asteroid spectroscopic survey. A feature-based taxonomy. *Icarus* 158(1):146–177. <https://doi.org/10.1006/icar.2002.6856>
- Cellino A, Zappalà V, Di Martino M et al (1987) Flattening, pole, and albedo features of 4 Vesta from photometric data. *Icarus* 70:546. [https://doi.org/10.1016/0019-1035\(87\)90095-9](https://doi.org/10.1016/0019-1035(87)90095-9)

- Cellino A, Belskaia I, Bendjoya P et al (2006) The strange polarimetric behavior of asteroid (234) Barbara. *Icarus* 180:565–567
- Cellino A, Gil-Hutton R, Dell’Oro A et al (2012) A new calibration of the albedo-polarization relation for the asteroids. *JQSR* 113(18):2552–2560. <https://doi.org/10.1016/j.jqsrt.2012.03.010>
- Cellino A, Bagnulo S, Tanga P et al (2014) A successful hunt for hidden Barbarians in the Watsonia asteroid family. *MNRAS Lett* 439:L75–L79
- Cellino A, Bagnulo S, Gil-Hutton R et al (2015) On the calibration of the relation between geometric albedo and polarimetric properties for the asteroids. *MNRAS* 451:3473–3488
- Cellino A, Ammannito E, Magni G et al (2016) The *Dawn* exploration of (4) Vesta as the ‘ground truth’ to interpret asteroid polarimetry. *MNRAS* 456(1):248–262. <https://doi.org/10.1093/mnras/stv2683>
- Cellino A, Bagnulo S, Belskaya I et al (2018) Unusual polarimetric properties of (101955) Bennu: similarities with F-class asteroids and cometary bodies. *MNRAS Lett* 481:L49–L53
- Cellino A, Bendjoya P, Delbó M et al (2020) Ground-based visible spectroscopy of asteroids to support the development of an unsupervised Gaia asteroid taxonomy. *A&A* 642:A80
- Chernova GP, Kiselev NN, Jockers K (1993) Polarimetric characteristics of dust particles as observed in 13 comets: comparisons with asteroids. *Icarus* 103(1):144–158. <https://doi.org/10.1006/icar.1993.1063>
- Chornaya E, Zubko E, Luk’yanyk I et al (2020) Imaging polarimetry and photometry of comet 21P/Giacobini-Zinner. *Icarus* 337:113471. <https://doi.org/10.1016/j.icarus.2019.113471>. [arXiv:2012.13208](https://arxiv.org/abs/2012.13208) [astro-ph.EP]
- Clarke D (1974) Polarimetric definitions. In: Gehrels T (ed) *IAU Colloq. 23: Planets, Stars, and Nebulae: Studied with Photopolarimetry*, p 45
- Coffeen DL (1974) Optical polarization measurements of the Jupiter atmosphere at 103° phase angle. *J Geophys Res* 79(25):3645. <https://doi.org/10.1029/JA079i025p03645>
- Coffeen DL, Gehrels T (1969) Wavelength dependence of polarization. XV. Observations of venus. *AJ* 74:433. <https://doi.org/10.1086/110822>
- Colin L, Hunten DM (1977) 11. Pioneer venus experiment descriptions. *Space Sci Rev* 20(4):451–525. <https://doi.org/10.1007/BF02186463>
- Da Deppo V, Jones G, Brydon G, et al (2021) The EnVisS camera for the Comet Interceptor ESA mission. In: *European Planetary Science Congress*, pp EPSC2021–101, <https://doi.org/10.5194/epsc2021-101>
- Daly RT, Ernst CM, Barnouin OS et al (2023) Successful kinetic impact into an asteroid for planetary defence. *Nature* 616(7957):443–447. <https://doi.org/10.1038/s41586-023-05810-5>. [arXiv:2303.02248](https://arxiv.org/abs/2303.02248) [astro-ph.EP]
- de Kok RJ, Stam DM, Karalidi T (2011) Characterizing exoplanetary atmospheres through infrared polarimetry. *ApJ* 741(1):59. <https://doi.org/10.1088/0004-637X/741/1/59>. [arXiv:1108.1290](https://arxiv.org/abs/1108.1290) [astro-ph.EP]
- De Sanctis MC, Vinogradoff V, Raponi A et al (2019) Characteristics of organic matter on Ceres from VIR/*Dawn* high spatial resolution spectra. *MNRAS* 482(2):2407–2421. <https://doi.org/10.1093/mnras/sty2772>
- Deb Roy P, Das HS, Medhi BJ (2015) Imaging polarimetry of Comet C/2012 L2 (LINEAR). *Icarus* 245:241–246. <https://doi.org/10.1016/j.icarus.2014.07.002>. [arXiv:1410.1660](https://arxiv.org/abs/1410.1660) [astro-ph.EP]
- Deb Roy P, Halder P, Das HS et al (2015) Imaging polarimetry of comets C/2013 V1 (Boattini) and 290P/Jager before and after perihelion. *MNRAS* 450(2):1770–1776. <https://doi.org/10.1093/mnras/stv707>
- Degewij J, Tedesco EF, Zellner B (1979) Albedo and color contrasts on asteroid surfaces. *Icarus* 40(3):364–374. [https://doi.org/10.1016/0019-1035\(79\)90029-0](https://doi.org/10.1016/0019-1035(79)90029-0)
- Degewij J, Andersson LE, Zellner B (1980) Photometric properties of outer planetary satellites. *Icarus* 44(2):520–540. [https://doi.org/10.1016/0019-1035\(80\)90042-1](https://doi.org/10.1016/0019-1035(80)90042-1)
- DeMeo F, Binzel R, Slivan S et al (2009) An extension of the Bus asteroid taxonomy into the near-infrared. *Icarus* 202:160–180
- Deschamps PY, Breon FM, Leroy M et al (1994) The POLDER mission: instrument characteristics and scientific objectives. *IEEE Trans Geosci Remote Sens* 32(3):598–615. <https://doi.org/10.1109/36.297978>
- Devogèle M, Cellino A, Borisov G et al (2018) The phase-polarization curve of asteroid (3200) Phaethon. *MNRAS* 479(3):3498–3508. <https://doi.org/10.1093/mnras/sty1587>. [arXiv:1806.05277](https://arxiv.org/abs/1806.05277) [astro-ph.EP]
- Devogèle M, Tanga P, Cellino A et al (2018) New polarimetric and spectroscopic evidence of anomalous enrichment in spinel-bearing calcium–aluminium-rich inclusions among L-type asteroids. *Icarus* 304:31–57. <https://doi.org/10.1016/j.icarus.2017.12.026>. [arXiv:1802.06975](https://arxiv.org/abs/1802.06975) [astro-ph.EP]

- di Serego Alighieri S (2019) The conventions for the polarization angle. In: Belluzzi L, Casini R, Romoli M, et al (eds) Solar Polarization Workshop 8, ASP Conference Series, vol 526. Astronomical Society of the Pacific, p 309
- Dlugach JM, Ivanova OV, Mishchenko MI et al (2018) Retrieval of microphysical characteristics of particles in atmospheres of distant comets from ground-based polarimetry. *JQRT* 205:80–90
- Dollfus A (1957) Étude des planètes par la polarisation de leur lumière. *Supplements aux Annales d'Astrophysique* 4:3–114
- Dollfus A (1961) Polarizations Studies of Planets. In: Kuiper GP, Middlehurst BM (eds) Planets and satellites. University of Chicago Press, Chicago, p 343
- Dollfus A, Auriere M (1974) Optical polarimetry of planet Mercury. *Icarus* 23(3):465–482. [https://doi.org/10.1016/0019-1035\(74\)90066-9](https://doi.org/10.1016/0019-1035(74)90066-9)
- Dollfus A, Bowell E (1971) Polarimetric properties of the lunar surface and its interpretation. Part I. Telescopic observations. *A&A* 10:29
- Dollfus A, Coffeen DL (1970) Polarization of venus I disk observations. *A&A* 8:251
- Dollfus A, Focas J (1969) The planet mars: the nature of its surface, the characteristic of its atmosphere from the polarimetry of its light. I. Observations. *A&A* 2:63
- Dollfus A, Zellner B (1979) Optical polarimetry of asteroids and laboratory samples. In: Gehrels T (ed) Asteroids. University of Arizona Press, Tucson, pp 170–183
- Dollfus A, Focas J, Bowell E (1969) The planet mars: the nature of its surface, the characteristics of its atmosphere from the polarimetry of its light. Part II—The Nature of the Soil. *A&A* 2:105
- Dollfus A, Bowell E, Titulaer C (1971) Polarimetric properties of the lunar surface and its interpretation. Part II. Terrestrial samples in orange light. *A&A* 10:450
- Dollfus A, Wolff M, Geake J et al (1989) Photopolarimetry of asteroids. In: Binzel R, Gehrels T, Matthews M (eds) Asteroids II. University of Arizona Press, Tucson, pp 594–616
- Dollfus AC (1955) Étude des planètes par la polarisation de leur lumière (Study of the Planets by Means of the Polarization of their Light). PhD thesis, Université Pierre et Marie Curie (Paris VI), France
- Donati JF, Semel M, Carter BD et al (1997) Spectropolarimetric observations of active stars. *MNRAS* 291(4):658–682. <https://doi.org/10.1093/mnras/291.4.658>
- Dones L, Brasser R, Kaib N et al (2015) Origin and evolution of the cometary reservoirs. *Space Sci Rev* 197(1–4):191–269. <https://doi.org/10.1007/s11214-015-0223-2>
- Draine BT, Flatau PJ (1994) Discrete-dipole approximation for scattering calculations. *J Opt Soc Am A* 11(4):1491–1499. <https://doi.org/10.1364/JOSAA.11.001491>
- Draine BT, Lee HM (1984) Optical properties of interstellar graphite and silicate grains. *ApJ* 285:89. <https://doi.org/10.1086/162480>
- Dubovik O, Sinyuk A, Lapyonok T et al (2006) Application of spheroid models to account for aerosol particle nonsphericity in remote sensing of desert dust. *J Geophys Res Atmos* 111(D11):D11208. <https://doi.org/10.1029/2005JD006619>
- Duley WW (1984) Refractive indices for amorphous carbon. *ApJ* 287:694–696. <https://doi.org/10.1086/162727>
- Duncan MJ, Levison HF (1997) A scattered comet disk and the origin of Jupiter family comets. *Science* 276:1670–1672. <https://doi.org/10.1126/science.276.5319.1670>
- Ebisawa S, Dollfus A (1993) Dust in the martian atmosphere: polarimetric sensing. *A&A* 272:671–686
- Egan WG, Johnson WR, Whitehead VS (1991) Terrestrial polarization imagery obtained from the Space Shuttle: characterization and interpretation. *Appl Opt* 30(4):435–442. <https://doi.org/10.1364/AO.30.000435>
- Ejeta C, Boehnhardt H, Bagnulo S et al (2012) Spectro-polarimetry of the bright side of Saturn's moon Iapetus. *A&A* 537:A23. <https://doi.org/10.1051/0004-6361/201117870>. [arXiv:1110.3163](https://arxiv.org/abs/1110.3163) [astro-ph.EP]
- Ejeta C, Muinonen K, Boehnhardt H et al (2013) Polarization of Saturn's moon Iapetus. III. Models of the bright and the dark sides. *A&A* 554:A117. <https://doi.org/10.1051/0004-6361/201220467>
- Emde C, Buras-Schnell R, Sterzik M et al (2017) Influence of aerosols, clouds, and sunglint on polarization spectra of Earthshine. *A&A* 605:A2. <https://doi.org/10.1051/0004-6361/201629948>. [arXiv:1705.03298](https://arxiv.org/abs/1705.03298) [astro-ph.EP]
- Escobar-Cerezo J, Palmer C, Muñoz O et al (2017) Scattering properties of large irregular cosmic dust particles at visible wavelengths. *ApJ* 838(1):74. <https://doi.org/10.3847/1538-4357/aa6303>
- Escobar-Cerezo J, Muñoz O, Moreno F et al (2018) An experimental scattering matrix for lunar regolith simulants JSC-1A at visible wavelengths. *ApJS* 235(1):19. <https://doi.org/10.3847/1538-4365/aa66cc>

- Feldman PD, Cochran AL, Combi MR (2004) Spectroscopic investigations of fragment species in the coma. In: Festou MC, Keller HU, Weaver HA (eds) *Comets II*. University of Arizona Press, Tucson, p 425
- Feofilov PP (1961) The physical basis of polarized emission. Consultants Bureau, New York
- Fix LA, Kelsey JD (1973) Polarimetry of Pluto. *ApJ* 184:633–636. <https://doi.org/10.1086/152354>
- Fossati L, Bagnulo S, Haswell CA et al (2012) The habitability and detection of earth-like planets orbiting cool white dwarfs. *ApJL* 757(1):L15. <https://doi.org/10.1088/2041-8205/757/1/L15>. [arXiv:1207.6210](https://arxiv.org/abs/1207.6210) [astro-ph.SR]
- Fouchard M, Rickman H, Froeschlé C et al (2017) On the present shape of the Oort cloud and the flux of new comets. *Icarus* 292:218–233. <https://doi.org/10.1016/j.icarus.2017.01.013>
- Frattin E, Muñoz O, Moreno F et al (2019) Experimental phase function and degree of linear polarization of cometary dust analogues. *MNRAS* 484(2):2198–2211. <https://doi.org/10.1093/mnras/stz129>. [arXiv:1901.05975](https://arxiv.org/abs/1901.05975) [astro-ph.EP]
- Frattin E, Martikainen J, Muñoz O et al (2022) Experimental phase function and degree of linear polarization curve of olivine and spinel and the origin of the Barbarian polarization behaviour. *MNRAS* 517:5463–5472
- Fukuhara T, Futaguchi M, Hashimoto GL et al (2017) Large stationary gravity wave in the atmosphere of Venus. *Nat Geosci* 10(2):85–88. <https://doi.org/10.1038/ngeo2873>
- Fulle M (2004) Motion of cometary dust. In: Festou MC, Keller HU, Weaver HA (eds) *Comets II*. University of Arizona Press, Tucson, p 565
- Ganesh S, Joshi UC, Baliyan KS (2009) Optical polarimetry of Comet NEAT C/2001 Q4. *Icarus* 201(2):666–673. <https://doi.org/10.1016/j.icarus.2009.01.008>. [arXiv:0901.2789](https://arxiv.org/abs/0901.2789) [astro-ph.EP]
- García RS, Gil-Hutton R, García-Migani E (2020) Observational results for five short-period and five long-period comets. *Planet Space Sci* 180:104779. <https://doi.org/10.1016/j.pss.2019.104779>
- Gautam P, Sorensen CM (2021) A wide range (0.32°–177.6°), multi-angle light scattering setup and concomitant analysis method. *Rev Sci Instr* 92(11):113105. <https://doi.org/10.1063/5.0068318>
- Geake J, Dollfus A (1986) Planetary surface texture and albedo from parameter plots of optical polarization data. *MNRAS* 218:75–91
- Geake JE, Geake M (1990) A remote sensing method for sub-wavelength grains on planetary surfaces by optical polarimetry. *MNRAS* 245:46. <https://doi.org/10.1093/mnras/245.1.46>
- Geffrin JM, Sabouroux P (2009) Continuing with the fresnel database: experimental setup and improvements in 3d scattering measurements. *Inverse Prob* 25(2):024001. <https://doi.org/10.1088/0266-5611/25/2/024001>
- Geffrin JM, García-Cámara B, Gómez-Medina R et al (2012) Magnetic and electric coherence in forward- and back-scattered electromagnetic waves by a single dielectric subwavelength sphere. *Nat Commun* 3:1171. <https://doi.org/10.1038/ncomms2167>
- Gehrels T, Herman BM, Owen T (1969) Wavelength dependence of polarization. XIV. Atmosphere of jupiter. *AJ* 74:190. <https://doi.org/10.1086/110790>
- Gehrels T, Baker LR, Beshore E et al (1980) Imaging photopolarimeter on pioneer saturn. *Science* 207(4429):434–439. <https://doi.org/10.1126/science.207.4429.434>
- Gehrz RD, Ney EP, (1992) 0.7- to 23- μ m photometric observations of P, Halley, (1986) III and six recent bright comets. *Icarus* 100(1):162–186. [https://doi.org/10.1016/0019-1035\(92\)90027-5](https://doi.org/10.1016/0019-1035(92)90027-5)
- Gehrz RD, Ney EP, Piscitelli J et al (1989) Infrared photometry and spectroscopy of comet 2P/Encke 1987. *Icarus* 80(2):280–288. [https://doi.org/10.1016/0019-1035\(89\)90139-5](https://doi.org/10.1016/0019-1035(89)90139-5)
- Goidet-Devel B, Renard JB, Levasseur-Regourd AC (1995) Polarization of asteroids. Synthetic curves and characteristic parameters. *Planet Space Sci* 43(6):779–786. [https://doi.org/10.1016/0032-0633\(94\)00140-M](https://doi.org/10.1016/0032-0633(94)00140-M)
- Gómez Martín JC, Muñoz O, Martikainen J et al (2024) Experimental phase function and degree of linear polarization of light scattered by hydrogenated amorphous carbon circumstellar dust analogs. *ApJS* 270(1):2. <https://doi.org/10.3847/1538-4365/ad0379>
- González-Gaitán S, Mourão AM, Patat F et al (2020) Tips and tricks in linear imaging polarimetry of extended sources with FORS2 at the VLT. *A&A* 634:A70. <https://doi.org/10.1051/0004-6361/201936379>. [arXiv:1912.08684](https://arxiv.org/abs/1912.08684) [astro-ph.IM]
- Gradie J, Tedesco E (1982) Compositional structure of the asteroid belt. *Science* 216:1405–1407
- Grav T, Bauer JM, Mainzer AK et al (2015) NEOWISE: observations of the irregular satellites of Jupiter and Saturn. *ApJ* 809(1):3. <https://doi.org/10.1088/0004-637X/809/1/3>. [arXiv:1505.07820](https://arxiv.org/abs/1505.07820) [astro-ph.EP]

- Gray Z, Bagnulo S, Boehnhardt H et al (2024) Imaging polarimetry of comet 67 P/Churyumov-Gerasimenko: homogeneous distribution of polarization and its implications. *MNRAS* 531(1):1638–1652. <https://doi.org/10.1093/mnras/stae1284>. arXiv:2405.09297 [astro-ph.EP]
- Gray Z, Bagnulo S, Granvik M et al (2024) Polarimetry of Didymos–Dimorphos: unexpected long-term effects of the DART impact. *Planet Sci J* 5(1):18. <https://doi.org/10.3847/PSJ/ad0f18>. arXiv:2311.13483 [astro-ph.EP]
- Grynko Y, Shkuratov Y, Förstner J (2020) Light backscattering from large clusters of densely packed irregular particles. *JQSRT* 255:107234. <https://doi.org/10.1016/j.jqsrt.2020.107234>
- Grynko Y, Shkuratov Y, Alhaddad S et al (2022) Negative polarization of light at backscattering from a numerical analog of planetary regoliths. *Icarus* 384:115099. <https://doi.org/10.1016/j.icarus.2022.115099>
- Gundlach B, Fulle M, Blum J (2020) On the activity of comets: understanding the gas and dust emission from comet 67/Churyumov-Gerasimenko's south-pole region during perihelion. *MNRAS* 493(3):3690–3715. <https://doi.org/10.1093/mnras/staa449>
- Gustafson BÅS (1996) Microwave analog to light scattering measurements: a modern implementation of a proven method to achieve precise control. *JQSRT* 55(5):663–672. [https://doi.org/10.1016/0022-4073\(96\)00009-X](https://doi.org/10.1016/0022-4073(96)00009-X)
- Gustafson BÅS, Kolokolova L (1999) A systematic study of light scattering by aggregate particles using the microwave analog technique: Angular and wavelength dependence of intensity and polarization. *J Geophys Res* 104(D24):31711–31720. <https://doi.org/10.1029/1999JD900327>
- Güttler C, Mannel T, Rotundi A et al (2019) Synthesis of the morphological description of cometary dust at comet 67P/Churyumov-Gerasimenko. *A&A* 630:A24. <https://doi.org/10.1051/0004-6361/201834751>. arXiv:1902.10634 [astro-ph.EP]
- Guzik P, Drahus M, Rusek K et al (2020) Initial characterization of interstellar comet 2I/Borisov. *Nature Astron* 4:53–57. <https://doi.org/10.1038/s41550-019-0931-8>. arXiv:1909.05851 [astro-ph.EP]
- Hadamcik E, Lvasseur-Regourd AC (2003) Dust evolution of comet C/1995 O1 (Hale-Bopp) by imaging polarimetric observations. *A&A* 403:757–768. <https://doi.org/10.1051/0004-6361:20030378>
- Hadamcik E, Lvasseur-Regourd AC (2003) Imaging polarimetry of cometary dust: different comets and phase angles. *JQSRT* 79–80:661–678. [https://doi.org/10.1016/S0022-4073\(02\)00314-X](https://doi.org/10.1016/S0022-4073(02)00314-X)
- Hadamcik E, Lvasseur-Regourd AC (2009) Optical properties of dust from Jupiter family comets. *Planet Space Sci* 57(10):1118–1132. <https://doi.org/10.1016/j.pss.2008.10.015>
- Hadamcik E, Renard JB, Lvasseur-Regourd AC et al (2006) Light scattering by fluffy particles with the PROGRA2 experiment: mixtures of materials. *JQSRT* 100:143–156. <https://doi.org/10.1016/j.jqsrt.2005.11.032>
- Hadamcik E, Renard JB, Lasue J et al (2023) Low-albedo asteroids: analogues with a high polarization at large phase angles. *MNRAS* 520(2):1963–1974. <https://doi.org/10.1093/mnras/stac2749>
- Hall JS, Riley LA (1974) A photometric study of saturn and its rings. *Icarus* 23(2):144–156. [https://doi.org/10.1016/0019-1035\(74\)90002-5](https://doi.org/10.1016/0019-1035(74)90002-5)
- Hanner MS, Bradley JP (2004) Composition and mineralogy of cometary dust. In: Festou MC, Keller HU, Weaver HA (eds) *Comets II*. University of Arizona Press, Tucson, p 555
- Hansen JE (1971) Circular polarization of sunlight reflected by clouds. *J Atmos Sci* 28:1515–1516. [https://doi.org/10.1175/1520-0469\(1971\)028<1515:CPOSRB>2.0.CO;2](https://doi.org/10.1175/1520-0469(1971)028<1515:CPOSRB>2.0.CO;2)
- Hansen JE, Arking A (1971) Clouds of venus: evidence for their nature. *Science* 171(3972):669–672. <https://doi.org/10.1126/science.171.3972.669>
- Hansen JE, Hovenier JW (1974) Interpretation of the polarization of Venus. *J Atmos Sci* 31:1137–1160. [https://doi.org/10.1175/1520-0469\(1974\)031<1137:IOTPOV>2.0.CO;2](https://doi.org/10.1175/1520-0469(1974)031<1137:IOTPOV>2.0.CO;2)
- Hansen JE, Travis LD (1974) Light scattering in planetary atmospheres. *Space Sci Rev* 16(4):527–610. <https://doi.org/10.1007/BF00168069>
- Harris A, Davies J, Green S (1998) Thermal infrared spectrophotometry of the near-earth asteroids 2100 Ra-Shalom and 1991 EE. *Icarus* 135:441–450
- Hasegawa H, Ichikawa T, Abe S et al (1997) Near-infrared photometric and polarimetric observations of comet hale-bopp. *Earth Moon Planets* 78:353–358. <https://doi.org/10.1023/A:1006298327163>
- Henning T, Il'In VB, Krivova NA et al (1999) WWW database of optical constants for astronomy. *A&AS* 136:405–406. <https://doi.org/10.1051/aas:1999222>
- Hergenrother C, Adam C, Chesley S, et al (2020) Introduction to the Special Issue: Exploration of the Activity of Asteroid (101955) Bennu. *J Geophys Res Planets* 125:e06549

- Hines DC, Levasseur-Regourd AC (2016) Polarimetry observations of comets: status, questions, future pathways. *Planet Space Sci* 123:41–50. <https://doi.org/10.1016/j.pss.2015.11.016>
- Hovenier JW (2000) Measuring scattering matrices of small particles at optical wavelengths. In: Mishchenko MI, Hovenier JW, Travis LD (eds) *Light scattering by nonspherical particles: theory, measurements, and applications*. Academic Press, San Diego
- Hovenier JW, Van Der Mee C, Domke H (2004) Transfer of polarized light in planetary atmospheres: basic concepts and practical methods. *Astrophysics and Space Science Library*, vol 318. Springer, Dordrecht. <https://doi.org/10.1007/978-1-4020-2856-4>
- Ingersoll AP (1971) Polarization measurements of mars and mercury: Rayleigh scattering in the Martian atmosphere. *ApJ* 163:121. <https://doi.org/10.1086/150750>
- Ishimaru K, Lauretta DS (2024) Analysis of layered boulders on asteroid (101955) Bennu and their implications for fluid flow on the parent body. *Meteorit Planet Sci* 59(1):193–210. <https://doi.org/10.1111/maps.14115>
- Ito T, Ishiguro M, Arai T et al (2018) Extremely strong polarization of an active asteroid (3200) Phaethon. *Nat Commun* 9:2486
- Ivanova O, Rosenbush V, Afanasiev V et al (2017) Polarimetry, photometry, and spectroscopy of comet C/2009 P1 (Garradd). *Icarus* 284:167–182. <https://doi.org/10.1016/j.icarus.2016.11.014>. arXiv:2101.05110 [astro-ph.EP]
- Ivanova O, Luk'yanyk I, Kolokolova L et al (2019) Photometry, spectroscopy, and polarimetry of distant comet C/2014 A4 (SONEAR). *A&A* 626:A26. <https://doi.org/10.1051/0004-6361/201935077>. arXiv:1905.02465 [astro-ph.EP]
- Ivanova O, Rosenbush V, Luk'yanyk I et al (2021) Observations of distant comet C/2011 KP36 (Spacewatch): photometry, spectroscopy, and polarimetry. *A&A* 651:A29. <https://doi.org/10.1051/0004-6361/202039668>
- Ivanova O, Licandro J, Moreno F et al (2023) Long-lasting activity of asteroid (248370) 2005 QN₁₇₃. *MNRAS* 525(1):402–414. <https://doi.org/10.1093/mnras/stad2294>
- Ivanova O, Rosenbush V, Luk'yanyk I et al (2023) Quasi-simultaneous photometric, polarimetric, and spectral observations of distant comet C/2014 B1 (Schwartz). *A&A* 672:A76. <https://doi.org/10.1051/0004-6361/202244686>
- Ivanova OV, Dlugach JM, Afanasiev VL et al (2015) CCD polarimetry of distant comets C/2010 S1 (LINEAR) and C/2010 R1 (LINEAR) at the 6-m telescope of the SAO RAS. *Planet Space Sci* 118:199–210. <https://doi.org/10.1016/j.pss.2015.05.009>. arXiv:1506.07986 [astro-ph.EP]
- Jackson JD (1998) *Classical electrodynamics*, 3rd edn. Wiley-VCH, New York
- Jeong M, Kim SS, Garrick-Bethell I et al (2015) Multi-band polarimetry of the lunar surface. I. Global properties. *ApJS* 221(1):16. <https://doi.org/10.1088/0067-0049/221/1/16>
- Jiang H, Ji J, Yu L et al (2023) Mid-IR observations of IRAS, AKARI, WISE/NEOWISE, and Subaru for Large Icy Asteroid (704) Interamnia: a new perspective of regolith properties and water ice fraction. *ApJ* 944(2):202. <https://doi.org/10.3847/1538-4357/acaea>. arXiv:2212.09534 [astro-ph.EP]
- Jockers K, Kiselev N, Bonev T et al (2005) CCD imaging and aperture polarimetry of comet 2P/Encke: are there two polarimetric classes of comets? *A&A* 441(2):773–782. <https://doi.org/10.1051/0004-6361/20053348>
- Jones GH, Snodgrass C, Tubiana C et al (2024) The Comet Interceptor mission. *Space Sci Rev* 220(1):9. <https://doi.org/10.1007/s11214-023-01035-0>
- Jones TJ, Gehrz RD (2000) Infrared imaging polarimetry of comet C/1995 01 (Hale-Bopp). *Icarus* 143(2):338–346. <https://doi.org/10.1006/icar.1999.6275>
- Jones TJ, Stark D, Woodward CE, et al (2008) Evidence of fragmenting dust particles from near-simultaneous optical and near-infrared photometry and polarimetry of comet 73P/Schwassmann-Wachmann 3. *AJ* 135(4):1318–1327. <https://doi.org/10.1088/0004-6256/135/4/1318>, arXiv:0802.1182 [astro-ph]
- Joos F, Schmid HM (2007) Limb polarization of Uranus and Neptune. II. Spectropolarimetric observations. *A&A* 463(3):1201–1210. <https://doi.org/10.1051/0004-6361/20066212>, arXiv:astro-ph/0612213 [astro-ph]
- Joshi UC, Sen AK, Deshpande MR et al (1992) Photopolarimetric studies of Comet Austin. *J Astrophys Astron* 13(3):267–277. <https://doi.org/10.1007/BF02702294>
- Joshi UC, Baliyan KS, Ganesh S (2003) Polarization studies of comet C/2000 WM1 (LINEAR). *A&A* 405:1129–1135. <https://doi.org/10.1051/0004-6361/20030684>, arXiv:astro-ph/0305243 [astro-ph]
- Kahn R, West R, McDonald D et al (1997) Sensitivity of multiangle remote sensing observations to aerosol sphericity. *J Geophys Res* 102(14):16861–16870. <https://doi.org/10.1029/96JD01934>

- Kattawar GW, Adams CN (1971) Flux and polarization reflected from a Rayleigh-scattering planetary atmosphere. *ApJ* 167:183. <https://doi.org/10.1086/151017>
- Kattawar GW, Plass GN, Adams CN (1971) Flux and polarization calculations of the radiation reflected from the clouds of venus. *ApJ* 170:371. <https://doi.org/10.1086/151222>
- Kawabata K, Coffeen DL, Hansen JE et al (1980) Cloud and haze properties from Pioneer Venus polarimetry. *J Geophys Res* 85:8129–8140. <https://doi.org/10.1029/JA085iA13p08129>
- Keller CU (2002) Instrumentation for astrophysical spectropolarimetry. In: Trujillo-Bueno J, Moreno-Insertis F, Sánchez F (eds) *Astrophysical spectropolarimetry*. Cambridge University Press, Cambridge, pp 303–354
- Keller CU, Snik F, Harrington DM et al (2015) Instrumentation. In: Kolokolova L, Hough J, Levasseur-Regourd AC (eds) *Polarimetry of stars and planetary systems*. Cambridge University Press, Cambridge, p 35
- Kelley MS, Woodward CE, Harker DE, et al (2006) A spitzer study of comets 2P/Encke, 67P/Churyumov-Gerasimenko, and C/2001 HT50 (LINEAR-NEAT). *ApJ* 651(2):1256–1271. <https://doi.org/10.1086/507701>, [arXiv:astro-ph/0607416](https://arxiv.org/abs/astro-ph/0607416) [astro-ph]
- Kelley MSP, Hsieh HH, Bodewits D et al (2023) Spectroscopic identification of water emission from a main-belt comet. *Nature* 619(7971):720–723. <https://doi.org/10.1038/s41586-023-06152-y>
- Kemp JC, Wolstencroft RD (1971) Circular polarization: Jupiter and other planets. *Nature* 232(5307):165–168. <https://doi.org/10.1038/232165a0>
- Kikuchi S (2006) Linear polarimetry of five comets. *JQSRT* 100(1–3):179–186. <https://doi.org/10.1016/j.jqsrt.2005.11.036>
- Kikuchi S, Mikami Y, Mukai T et al (1987) Polarimetry of comet P/Halley. *A&A* 187(1–2):689–692
- Kikuchi S, Mikami Y, Mukai T et al (1989) Polarimetry of Comet Bradfield (1987s). *A&A* 214(1–2):386–388
- Kiselev N, Rosenbush V, Jockers K et al (2005) Database of comet polarimetry: analysis and some results. *Earth Moon Planets* 97(3–4):365–378. <https://doi.org/10.1007/s11038-006-9080-z>
- Kiselev N, Rosenbush V, Levasseur-Regourd AC et al (2015) Comets. In: Kolokolova L, Hough J, Levasseur-Regourd AC (eds) *Polarimetry of stars and planetary systems*. Cambridge University Press, Cambridge, p 379
- Kiselev N, Shubina E, Velichko S et al (2017) Compilation of comet polarimetry from published and unpublished sources. *NASA Planet Data Syst* 2:8
- Kiselev N, Rosenbush V, Ivanova O et al (2020) Comet 2P/Encke in apparition of 2017: II. Polarization and color. *Icarus* 348:113768. <https://doi.org/10.1016/j.icarus.2020.113768>. [arXiv:2101.04193](https://arxiv.org/abs/2101.04193) [astro-ph.EP]
- Kiselev N, Rosenbush V, Muinonen K et al (2022) New polarimetric data for the Galilean satellites: Europa observations and modeling. *Planet Sci J* 3(6):134. <https://doi.org/10.3847/PSJ/ac6bef>
- Kiselev N, Rosenbush V, Leppälä A et al (2024) New polarimetric data for the Galilean satellites: Io and Ganymede observations and modeling. *Planet Sci J* 5(1):10. <https://doi.org/10.3847/PSJ/ad0bf9>
- Kiselev N, Savushkin AA, Petrov DV et al (2024) Results of polarimetric and photometric observations of NEAs 162082 (1998 HL1), 163373 (2002 PZ39), 52768 (1982 OR2), and 159402 (1999 AP10). *MNRAS* 527(2):3174–3182. <https://doi.org/10.1093/mnras/stad3189>
- Kiselev NN, Lupishko DF (2004) Properties and peculiarities of Mercury’s regolith disk-integrated polarimetry in 2000–2002. *Solar Syst Res* 38(2):85–92. <https://doi.org/10.1023/B:SOLS.0000022819.93494.4d>
- Kiselev NN, Chernova GP, Lupishko DF (1994) Polarimetry of asteroids 1036 Ganymed and 1627 Ivar. *Kinem Fiz Neb Tel* 10(2):35–39
- Kiselev NN, Jockers K, Bonev T (2004) CCD imaging polarimetry of Comet 2P/Encke. *Icarus* 168(2):385–391. <https://doi.org/10.1016/j.icarus.2003.12.012>
- Kiselev NN, Rosenbush VK, Petrov D et al (2022) Asteroid (3200) Phaethon: results of polarimetric, photometric, and spectral observations. *MNRAS* 514(4):4861–4875. <https://doi.org/10.1093/mnras/stac1559>. [arXiv:2206.00911](https://arxiv.org/abs/2206.00911) [astro-ph.EP]
- Knibbe WJJ, de Haan JF, Hovenier JW et al (1997) A biwavelength analysis of pioneer venus polarization observations. *J Geophys Res* 102(E5):10945–10958. <https://doi.org/10.1029/97JE00312>
- Knibbe WJJ, de Haan JF, Hovenier JW et al (1998) Analysis of temporal variations of the polarization of Venus observed by Pioneer Venus Orbiter. *J Geophys Res* 103(E4):8557–8574. <https://doi.org/10.1029/97JE03558>

- Kochergin A, Zubko E, Chornaya E et al (2021) Monitoring the negative polarization in Comet 29P/Schwassmann–Wachmann during quiescence. *Icarus* 366:114536. <https://doi.org/10.1016/j.icarus.2021.114536>
- Kochergin A, Zubko E, Chornaya E et al (2023) Microphysics of dust in a distant comet C/2017 K2 (PanSTARRS) retrieved by means of polarimetry. *JQSRT* 297:108471. <https://doi.org/10.1016/j.jqsrt.2022.108471>
- Kokololova L, Jockers K (1997) Composition of cometary dust from polarization spectra. *Planet Space Sci* 45:1543–1550. [https://doi.org/10.1016/S0032-0633\(97\)00099-8](https://doi.org/10.1016/S0032-0633(97)00099-8)
- Kokololova L, Kimura H (2010) Effects of electromagnetic interaction in the polarization of light scattered by cometary and other types of cosmic dust. *A&A* 513:A40. <https://doi.org/10.1051/0004-6361/200913681>
- Kokololova L, Hanner MS, Levasseur-Regourd AC et al (2004) Physical properties of cometary dust from light scattering and thermal emission. In: Festou MC, Keller HU, Weaver HA (eds) *Comets II*. University of Arizona Press, Tucson, p 577
- Kokololova L, Kimura H, Kiselev N, et al (2007) Two different evolutionary types of comets proved by polarimetric and infrared properties of their dust. *A&A* 463(3):1189–1196. <https://doi.org/10.1051/0004-6361:20065069>, [arXiv:astro-ph/0703220](https://arxiv.org/abs/astro-ph/0703220) [astro-ph]
- Kokololova L, Hough J, Levasseur-Regourd AC (2015) *Polarimetry of stars and planetary systems*. Cambridge University Press, Cambridge. <https://doi.org/10.1017/CBO9781107358249>
- Ksanfomaliti LV, Moroz VI, Dollfus A (1975) Polarimetric experiment aboard Mars 5. *Kosmicheskie Issledovaniia* 13:92–98
- Kulyk I (2012) Brightness and polarization opposition effects at low phase angles of the Saturnian satellites Tethys, Dione, and Rhea. *Planet Space Sci* 73(1):407–424. <https://doi.org/10.1016/j.pss.2012.07.019>
- Kwon Y, Bagnulo S, Cellino A (2023) Optical spectropolarimetry of large C-complex asteroids: polarimetric evidence for heterogeneous surface compositions. *A&A* 677:A146
- Kwon YG, Ishiguro M, Kuroda D, et al (2017) Optical and Near-infrared Polarimetry of Non-periodic Comet C/2013 US10 (Catalina). *AJ* 154(4):173. <https://doi.org/10.3847/1538-3881/aa89ef>, [arXiv:1708.09528](https://arxiv.org/abs/1708.09528) [astro-ph.EP]
- Kwon YG, Ishiguro M, Shinnaka Y et al (2018) High polarization degree of the continuum of comet 2P/Encke based on spectropolarimetric signals during its 2017 apparition. *A&A* 620:A161. <https://doi.org/10.1051/0004-6361/201833968>, [arXiv:1810.02462](https://arxiv.org/abs/1810.02462) [astro-ph.EP]
- Kwon YG, Ishiguro M, Kwon J et al (2019) Near-infrared polarimetric study of near-Earth object 252P/LINEAR: an implication of scattered light from the evolved dust particles. *A&A* 629:A121. <https://doi.org/10.1051/0004-6361/201935542>, [arXiv:1907.03952](https://arxiv.org/abs/1907.03952) [astro-ph.EP]
- Kwon YG, Kokololova L, Agarwal J et al (2021) An update of the correlation between polarimetric and thermal properties of cometary dust. *A&A* 650:L7. <https://doi.org/10.1051/0004-6361/202141199>, [arXiv:2105.13182](https://arxiv.org/abs/2105.13182) [astro-ph.EP]
- Kwon YG, Bagnulo S, Markkanen J et al (2022) VLT spectropolarimetry of comet 67P: dust environment around the end of its intense southern summer. *A&A* 657:A40. <https://doi.org/10.1051/0004-6361/202141865>, [arXiv:2110.00266](https://arxiv.org/abs/2110.00266) [astro-ph.EP]
- Kwon YG, Masiero JR, Markkanen J (2022) Examining the dust of the tailless Oort-cloud comet C/2020 T2. *A&A* 668:A97. <https://doi.org/10.1051/0004-6361/202244853>
- Kwon YG, Bagnulo S, Markkanen J, et al (2024) The pre-perihelion evolution of the activity of comet C/2017 K2 (Pan-STARRS) during the water ice-line crossover. *AJ* 168(4):164. <https://doi.org/10.3847/1538-3881/ad6b15>, [arXiv:2408.01636](https://arxiv.org/abs/2408.01636) [astro-ph.EP]
- Lamy PL, Toth I, Fernandez YR et al (2004) The sizes, shapes, albedos, and colors of cometary nuclei. In: Festou MC, Keller HU, Weaver HA (eds) *Comets II*. University of Arizona Press, Tucson, p 223
- Landau R (1975) The 3.5-micron polarization of mercury. *Icarus* 26(2):243–249. [https://doi.org/10.1016/0019-1035\(75\)90084-6](https://doi.org/10.1016/0019-1035(75)90084-6)
- Landi Degl'Innocenti E, Landolfi M (2004) Polarization in spectral lines. *Astrophysics and Space Science Library*, vol 307. Springer, Dordrecht. <https://doi.org/10.1007/1-4020-2415-0>
- Landi Degl'Innocenti E, Bagnulo S, Fossati L (2007) Polarimetric standardization. In: Sterken C (ed) *The future of photometric, spectrophotometric and polarimetric standardization*. ASP Conference Series, vol 364. Astronomical Society of the Pacific, p 495, <https://doi.org/10.48550/arXiv.astro-ph/0610262>, [arXiv:astro-ph/0610262](https://arxiv.org/abs/astro-ph/0610262)
- Lane AL, Hord CW, West RA et al (1982) Photopolarimetry from Voyager 2: preliminary results on Saturn, Titan, and the Rings. *Science* 215(4532):537–543. <https://doi.org/10.1126/science.215.4532.537>

- Lane AL, Hord CW, West RA et al (1986) Photometry from Voyager 2: initial results from the Uranian Atmosphere, Satellites, and Rings. *Science* 233(4759):65–70. <https://doi.org/10.1126/science.233.4759.65>
- Le Borgne JF, Crovisier J (1987) Polarization of molecular fluorescence bands in comets: recent observations and interpretation. In: Rolfe EJ, Battrick B, Ackerman M, et al (eds) *Diversity and similarity of comets*, pp 171–175
- Le Borgne JF, Leroy JL, Arnaud J (1987) Polarimetry of comet P/Halley: continuum versus molecular bands. *A&A* 187:526
- Le Borgne JF, Leroy JL, Arnaud J (1987) Polarimetry of visible and near-UV molecular bands—Comets P/Halley and Hartley–Good. *A&A* 173(1):180–182
- Levasseur-Regourd AC, Cabane M, Haudebourg V et al (1998) Light scattering by dust under microgravity conditions. *Earth Moon Planets* 80:343–368. <https://doi.org/10.1023/A:1006390518381>
- Levasseur-Regourd AC, Renard JB, Shkuratov Y et al (2015) Laboratory studies. In: Kolokolova L, Hough J, Levasseur-Regourd AC (eds) *Polarimetry of stars and planetary systems*. Cambridge University Press, Cambridge, p 35
- Levasseur-Regourd AC, Agarwal J, Cottin H et al (2018) Cometary dust. *Space Sci Rev* 214(3):64. <https://doi.org/10.1007/s11214-018-0496-3>
- Levison HF, Olkin CB, Noll KS et al (2021) Lucy mission to the trojan asteroids: science goals. *Planet Sci J* 2(5):171. <https://doi.org/10.3847/PSJ/abf840>
- Li JY, Hirabayashi M, Farnham TL et al (2023) Ejecta from the DART-produced active asteroid Dimorphos. *Nature* 616(7957):452–456. <https://doi.org/10.1038/s41586-023-05811-4>. arXiv:2303.01700 [astro-ph.EP]
- Licandro J, de la Fuente Marcos C, de la Fuente Marcos R et al (2019) Spectroscopic and dynamical properties of comet C/2018 F4, likely a true average former member of the Oort cloud. *A&A* 625:A133. <https://doi.org/10.1051/0004-6361/201834902>. arXiv:1903.10838 [astro-ph.EP]
- Lillie CF, Hord CW, Pang K et al (1977) The Voyager mission photopolarimeter experiment. *Space Sci Rev* 21(2):159–181. <https://doi.org/10.1007/BF00200849>
- Liu J, Yang P, Muinonen K (2015) Dust-aerosol optical modeling with Gaussian spheres: Combined invariant-embedding T-matrix and geometric-optics approach. *JQSRT* 161:136–144. <https://doi.org/10.1016/j.jqsrt.2015.04.003>
- Liu L, Mishchenko M (2018) Scattering and radiative properties of morphologically complex carbonaceous aerosols: a systematic modeling study. *Remote Sens* 10(10):1634. <https://doi.org/10.3390/rs10101634>
- Lorenz RD, Smith PH, Lemmon MT (2004) Seasonal change in Titan’s haze 1992–2002 from Hubble Space Telescope observations. *Geophys Res Lett* 31(10):L10702. <https://doi.org/10.1029/2004GL019864>
- Lorenz RD, Lemmon MT, Smith PH (2006) Seasonal evolution of Titan’s dark polar hood: midsummer disappearance observed by the Hubble Space Telescope. *MNRAS* 369(4):1683–1687. <https://doi.org/10.1111/j.1365-2966.2006.10405.x>
- Lumme K (1993) Muinonen KO (1993) A two-parameter system for linear polarization of some solar system objects. *Asteroids, Meteors, Comets*, p 194
- Lupishko DF (2018) Generalized calibration of the polarimetric albedo scale of asteroids. *Solar Syst Res* 52(2):98–114. <https://doi.org/10.1134/S0038094618010069>
- Liot B (1929) Recherches sur la polarisation de la lumière des planètes et de quelques substances terrestres / Research on polarization of light from planets and some terrestrial substances. PhD thesis, Université Pierre et Marie Curie (Paris VI), France
- Mackowski DW (2022) The extension of the multiple sphere T matrix code to include multiple plane boundaries and 2-D periodic systems. *JQSRT* 290:108292. <https://doi.org/10.1016/j.jqsrt.2022.108292>
- Mackowski DW, Mishchenko MI (2011) A multiple sphere T-matrix Fortran code for use on parallel computer clusters. *JQSRT* 112:2182–2192. <https://doi.org/10.1016/j.jqsrt.2011.02.019>
- Maconi G, Helander P, Gritsevich M et al (2020) 4 π Scatterometer: a new technique for understanding the general and complete scattering properties of particulate media. *JQSRT* 246:106910. <https://doi.org/10.1016/j.jqsrt.2020.106910>
- Mahapatra G, Lefèvre M, Rossi L et al (2021) Polarimetry as a tool for observing orographic gravity waves on venus. *Planet Sci J* 2(3):96. <https://doi.org/10.3847/PSJ/abf4cf>
- Mahlke M, Carry B, Mattei P (2022) Asteroid taxonomy from cluster analysis of spectrometry and albedo. *A&A* 665:A26

- Malus, (1809) Ueber die Messung des Brechungsvermögens der undurchsichtigen Körper. *Ann Phys* 31 (3):225–234. <https://doi.org/10.1002/andp.18090310302>
- Mannel T, Bentley MS, Boakes PD et al (2019) Dust of comet 67P/Churyumov-Gerasimenko collected by Rosetta/MIDAS: classification and extension to the nanometer scale. *A&A* 630:A26. <https://doi.org/10.1051/0004-6361/201834851>
- Martikainen J, Muñoz O, Jardiel T et al (2023) Optical constants of martian dust analogs at UV-visible-near-infrared wavelengths. *ApJS* 268(2):47. <https://doi.org/10.3847/1538-4365/acf0be>
- Martin TZ, Goguen JD, Travis LD, et al (2000) Galileo PPR polarimetric phase curves for the Galilean satellites. In: *AAS/Division for Planetary Sciences Meeting Abstracts #32*, p 39.04
- Masiero J, Mainzer A, Grav T et al (2012) A revised asteroid polarization-Albedo relationship using WISE/NEOWISE data. *ApJ* 749:104
- Masiero J, Devoegele M, Macias I et al (2023) The increasingly strange polarimetric behavior of the Barbarian asteroids. *Planet Sci J* 4:93. <https://doi.org/10.3847/PSJ/acd383>
- McCord TB, Adams JB, Johnson TV (1970) Asteroid vesta: spectral reflectivity and compositional implications. *Science* 168(3938):1445–1447. <https://doi.org/10.1126/science.168.3938.1445>
- McLean W, Stam DM, Bagnulo S et al (2017) A polarimetric investigation of Jupiter: Disk-resolved imaging polarimetry and spectropolarimetry. *A&A* 601:A142. <https://doi.org/10.1051/0004-6361/201629314>
- Meech KJ, Svoren J (2004) Using cometary activity to trace the physical and chemical evolution of cometary nuclei. In: Festou MC, Keller HU, Weaver HA (eds) *Comets II*. University of Arizona Press, Tucson, p 317
- Meech KJ, Yang B, Kleyna J et al (2016) Inner solar system material discovered in the Oort cloud. *Sci Adv* 2:e1600038. <https://doi.org/10.1126/sciadv.1600038>
- Meierhenrich UJ, Thiemann WHP, Barbier B et al (2002) Circular polarization of light by planet mercury and enantiomorphism of its surface minerals. *Orig Life Evol Biosph* 32(2):181–190. <https://doi.org/10.1023/A:1016028930938>
- Meng Z, Yang P, Kattawar GW et al (2010) Single-scattering properties of tri-axial ellipsoidal mineral dust aerosols: A database for application to radiative transfer calculations. *J Aerosol Sci* 41(5):501–512. <https://doi.org/10.1016/j.jaerosci.2010.02.008>
- Michalsky JJ, Stokes RA (1977) Whole-disk polarization measurements of Uranus at visible wavelengths. *ApJL* 213:L135–L137. <https://doi.org/10.1086/182426>
- Miles-Páez PA, Pallé E, Zapatero Osorio MR (2014) Simultaneous optical and near-infrared linear spectropolarimetry of the earthshine. *A&A* 562:L5. <https://doi.org/10.1051/0004-6361/201323009>. [arXiv:1401.6029](https://arxiv.org/abs/1401.6029) [astro-ph.EP]
- Mishchenko M, Geogdzhayev I, Liu L et al (2003) Aerosol retrievals from AVHRR radiances: effects of particle nonsphericity and absorption and an updated long-term global climatology of aerosol properties. *JQSRT* 79–80:953. [https://doi.org/10.1016/S0022-4073\(02\)00331-X](https://doi.org/10.1016/S0022-4073(02)00331-X)
- Mishchenko MI (2006) Scale invariance rule in electromagnetic scattering. *JQSRT* 101(3):411–415. <https://doi.org/10.1016/j.jqsrt.2006.02.047>
- Mishchenko MI, Dlugach JM (1993) Coherent backscatter and the opposition effect for E-type asteroids. *Planet Space Sci* 41(3):173–181. [https://doi.org/10.1016/0032-0633\(93\)90056-8](https://doi.org/10.1016/0032-0633(93)90056-8)
- Mishchenko MI, Travis LD, Mackowski DW (1996) T-matrix computations of light scattering by nonspherical particles: a review. *JQSRT* 55(5):535–575. [https://doi.org/10.1016/0022-4073\(96\)00002-7](https://doi.org/10.1016/0022-4073(96)00002-7)
- Mishchenko MI, Hovenier JW, Travis LD (eds) (2000) *Light scattering by nonspherical particles: theory, measurements, and applications*. Academic Press, San Diego
- Mishchenko MI, Travis LD, Lasis AA (2006) *Multiple scattering of light by particles: radiative transfer and coherent backscattering*. Cambridge University Press, Cambridge
- Moreno F, Muñoz O, Guirado D et al (2007) Comet dust as a size distribution of irregularly shaped, compact particles. *JQSRT* 106(1–3):348–359. <https://doi.org/10.1016/j.jqsrt.2007.01.023>
- Morgado BE, Sicardy B, Braga-Ribas EA (2023) A dense ring of the trans-Neptunian object Quaoar outside its Roche limit. *Nature* 614(7947):239–243. <https://doi.org/10.1038/s41586-022-05629-6>
- Morozhenko AV, Yanovitskii EG (1973) The optical properties of venus and the Jovian planets. I. The atmosphere of Jupiter according to polarimetric observations. *Icarus* 18(4):583–592. [https://doi.org/10.1016/0019-1035\(73\)90060-2](https://doi.org/10.1016/0019-1035(73)90060-2)
- Mrozowski S (1936) Über den Isotopenverschiebungseffekt im Bandenspektrum des Quecksilberdeutrids. *Z. Angew Phys* 9(3–4):236–251. <https://doi.org/10.1007/BF01370567>

- Muinenen KO (1990) Light scattering by inhomogeneous media backward enhancement and reversal of linear polarization. PhD thesis, University of Helsinki, Finland
- Muinenen K, Saarinen K (2000) Ray optics approximation for Gaussian random cylinders. *JQSR* 64(2):201–218. [https://doi.org/10.1016/S0022-4073\(98\)00147-2](https://doi.org/10.1016/S0022-4073(98)00147-2)
- Muinenen K, Lumme K, Peltoniemi J et al (1989) Light scattering by randomly oriented crystals. *Appl Opt* 28:3051–3060. <https://doi.org/10.1364/AO.28.003051>
- Muinenen K, Nousiainen T, Fast P et al (1996) Light scattering by Gaussian random particles: ray optics approximation. *JQSR* 55(5):577–601. [https://doi.org/10.1016/0022-4073\(96\)00003-9](https://doi.org/10.1016/0022-4073(96)00003-9)
- Muinenen K, Penttälä A, Cellino A et al (2009) Asteroid photometric and polarimetric phase curves: joint linear-exponential modeling. *Meteorit Planet Sci* 44:1937–1946
- Muinenen K, Tynnelä J, Zubko E et al (2011) Polarization of light backscattered by small particles. *JQSR* 112:2193–2212. <https://doi.org/10.1016/j.jqsrt.2011.06.009>
- Muinenen K, Mishchenko MI, Dlugach JM et al (2012) Coherent backscattering verified numerically for a finite volume of spherical particles. *ApJ* 760(2):118. <https://doi.org/10.1088/0004-637X/760/2/118>
- Muinenen K, Penttälä A, Videen G (2015) Multiple scattering of light in particulate media. In: Kolokolova L, Hough J, Levasseur-Regourd AC (eds) *Polarimetry of stars and planetary systems*. Cambridge University Press, Cambridge, p 114
- Muñoz O, Volten H, de Haan JF et al (2000) Experimental determination of scattering matrices of olivine and Allende meteorite particles. *A&A* 360:777–788
- Muñoz O, Moreno F, Guirado D et al (2011) The IAA cosmic dust laboratory: experimental scattering matrices of clay particles. *Icarus* 211(1):894–900. <https://doi.org/10.1016/j.icarus.2010.10.027>
- Muñoz O, Moreno F, Gómez-Martín JC et al (2020) Experimental phase function and degree of linear polarization curves of millimeter-sized cosmic dust analogs. *ApJS* 247(1):19. <https://doi.org/10.3847/1538-4365/ab6851>
- Muñoz O, Frattin E, Jardiel T et al (2021) Retrieving dust grain sizes from photopolarimetry: an experimental approach. *ApJS* 256(1):17. <https://doi.org/10.3847/1538-4365/ac0efa>. [arXiv:2109.05764](https://arxiv.org/abs/2109.05764) [astro-ph.EP]
- Muñoz O, Frattin E, Martikainen J et al (2025) Update Granada–Amsterdam Light Scattering Database. *JQSR* 331:109252. <https://doi.org/10.1016/j.jqsrt.2024.109252>
- Myers RV (1985) Polarization of comets at small phase angles. *Icarus* 63(2):206–216. [https://doi.org/10.1016/0019-1035\(85\)90005-3](https://doi.org/10.1016/0019-1035(85)90005-3)
- Nelson RM, Hapke BW, Smythe WD et al (2000) The opposition effect in simulated planetary regoliths. Reflectance and circular polarization ratio change at small phase angle. *Icarus* 147(2):545–558. <https://doi.org/10.1006/icar.2000.6454>
- Nelson RM, Boryta MD, Hapke BW et al (2018) Laboratory simulations of planetary surfaces: understanding regolith physical properties from remote photopolarimetric observations. *Icarus* 302:483–498. <https://doi.org/10.1016/j.icarus.2017.11.021>
- Nesvorný D, Vokrouhlický D, Dones L et al (2017) Origin and evolution of short-period comets. *ApJ* 845(1):27. <https://doi.org/10.3847/1538-4357/aa7cf6>. [arXiv:1706.07447](https://arxiv.org/abs/1706.07447) [astro-ph.EP]
- Noll KS, Brown ME, Weaver HA et al (2020) Detection of a satellite of the Trojan Asteroid (3548) Eurybates—a Lucy mission target. *Planet Sci J* 1(2):44. <https://doi.org/10.3847/PSJ/abac54>. [arXiv:2008.01858](https://arxiv.org/abs/2008.01858) [astro-ph.EP]
- Öhman Y (1941) Measurements of polarization in the spectra of comet Cunningham (1940 C) and comet Paraskevopoulos (1941 C). *Stockholms Observatoriums Annaler* 13:11.1–11.20
- Oishi M, Kawara K, Kobayashi Y et al (1978) Infrared observations of Comet West (1975n). I. Observational results. *PASJ* 30:149–160
- Oishi M, Okuda H, Wickramasinghe NC (1978) Infrared observations of comet west (1975n). II. A model of the cometary dust. *PASJ* 30:161–172
- O’Leary BT, Rea DG (1967) On the polarimetric evidence for an atmosphere on Mercury. *ApJ* 148:249. <https://doi.org/10.1086/149141>
- Oliva E (1997) Wedged double Wollaston, a device for single shot polarimetric measurements. *A&AS* 123:589–592. <https://doi.org/10.1051/aas:1997175>
- Opitom C, Fitzsimmons A, Jehin E et al (2019) 2I/Borisov: A C₂-depleted interstellar comet. *A&A* 631:L8. <https://doi.org/10.1051/0004-6361/201936959>. [arXiv:1910.09078](https://arxiv.org/abs/1910.09078) [astro-ph.EP]
- Opitom C, Murphy B, Snodgrass C et al (2023) Morphology and spectral properties of the DART impact ejecta with VLT/MUSE. *A&A* 671:L11. <https://doi.org/10.1051/0004-6361/202345960>
- Ortiz JL, Duffard R, Pinilla-Alonso N et al (2015) Possible ring material around centaur (2060) Chiron. *A&A* 576:A18. <https://doi.org/10.1051/0004-6361/201424461>. [arXiv:1501.05911](https://arxiv.org/abs/1501.05911) [astro-ph.EP]

- Ortiz JL, Santos-Sanz P, Sicardy B et al (2017) The size, shape, density and ring of the dwarf planet Haumea from a stellar occultation. *Nature* 550(7675):219–223. <https://doi.org/10.1038/nature24051>. [arXiv:2006.03113](https://arxiv.org/abs/2006.03113) [astro-ph.EP]
- Oszkiewicz D, Troianskyi V, Galád A et al (2023) Spins and shapes of basaltic asteroids and the missing mantle problem. *Icarus* 397:115520. <https://doi.org/10.1016/j.icarus.2023.115520>
- Ovcharenko AA, Shkuratov YG (2000) Weak-localization effect for light backscattered by surfaces with a complex structure. *Opt Spectrosc* 88(2):253–259. <https://doi.org/10.1134/1.626788>
- Ovcharenko AA, Bondarenko SY, Zubko ES et al (2006) Particle size effect on the opposition spike and negative polarization. *JQSRT* 101(3):394–403. <https://doi.org/10.1016/j.jqsrt.2006.02.036>
- Patat F, Romaniello M (2006) Error analysis for dual-beam optical linear polarimetry. *PASP* 118(839):146–161. <https://doi.org/10.1086/497581>, [arXiv:astro-ph/0509153](https://arxiv.org/abs/astro-ph/0509153) [astro-ph]
- Patat F, Taubenberger S (2011) Characterisation of the CAFOS linear spectropolarimeter. *A&A* 529:A57. <https://doi.org/10.1051/0004-6361/201116566>. [arXiv:1102.4447](https://arxiv.org/abs/1102.4447) [astro-ph.IM]
- Patty CHL, Loes ten Kate I, Buma WJ et al (2019) Circular spectropolarimetric sensing of vegetation in the field: possibilities for the remote detection of extraterrestrial life. *Astrobiology* 19(10):1221–1229. <https://doi.org/10.1089/ast.2019.2050>. [arXiv:1902.05859](https://arxiv.org/abs/1902.05859) [astro-ph.EP]
- Pavlovsky CM, Clampin M, De Marchi G, et al (2002) ACS sensitivity. In: American Astronomical Society Meeting Abstracts #200, p 62.01
- Penttilä A, Lumme K, Hadamcik E et al (2005) Statistical analysis of asteroidal and cometary polarization phase curves. *A&A* 432:1081–1090
- Penttilä A, Muinonen K, Granvik M et al (2024) Modeling linear polarization of the Didymos-Dimorphos system before and after the DART impact. *Planet Sci J* 5(1):27. <https://doi.org/10.3847/PSJ/ad1757>
- Pereira CL, Sicardy B, Morgado BE et al (2023) The two rings of (50000) Quaoar. *A&A* 673:L4. <https://doi.org/10.1051/0004-6361/202346365>. [arXiv:2304.09237](https://arxiv.org/abs/2304.09237) [astro-ph.EP]
- Petropoulou V, Dotto E, Banaszekiewicz M, et al (2022) Neorocks: an innovative and pragmatic approach to planetary defense. Paper presented at 44th COSPAR Scientific Assembly. Held 16–24 July, 2022. Online at <https://www.cosparathens2022.org/>. Abstract B1.1-0080-22
- Petrov D, Shkuratov Y, Videen G (2011) Electromagnetic wave scattering from particles of arbitrary shapes. *JQSRT* 112:1636–1645. <https://doi.org/10.1016/j.jqsrt.2011.01.036>
- Petrov D, Shkuratov Y, Videen G (2012) Light scattering by arbitrary shaped particles with rough surfaces: Sh-matrices approach. *JQSRT* 113(18):2406–2418. <https://doi.org/10.1016/j.jqsrt.2012.04.016>
- Petrova EV, Tishkovets VP, Jockers K (2007) Modeling of opposition effects with ensembles of clusters: interplay of various scattering mechanisms. *Icarus* 188(1):233–245. <https://doi.org/10.1016/j.icarus.2006.11.011>
- Pirola V, Kosenkov IA, Berdyugin AV, et al (2021) Double image polarimeter—ultra fast: simultaneous three-color (BV R) polarimeter with electron-multiplying charge-coupled devices. *AJ* 161(1):20. <https://doi.org/10.3847/1538-3881/abc74f>
- Poch O, Cerubini R, Pommerol A et al (2018) Polarimetry of water ice particles providing insights on grain size and degree of sintering on icy planetary surfaces. *J Geophys Res Planets* 123(10):2564–2584. <https://doi.org/10.1029/2018JE005753>. [arXiv:1809.08435](https://arxiv.org/abs/1809.08435) [astro-ph.EP]
- Poch O, Istiqomah I, Quirico E, et al (2020) Ammonium salts are a reservoir of nitrogen on a cometary nucleus and possibly on some asteroids. *Science* 367(6483):aaw7462. <https://doi.org/10.1126/science.aaw7462>, [arXiv:2003.06034](https://arxiv.org/abs/2003.06034) [astro-ph.EP]
- Pope SK, Tomasko MG, Williams MS et al (1992) Clouds of ammonia ice: laboratory measurements of the single-scattering properties. *Icarus* 100(1):203–220. [https://doi.org/10.1016/0019-1035\(92\)90030-B](https://doi.org/10.1016/0019-1035(92)90030-B)
- Prialnik D, Benkhoff J, Podolak M (2004) Modeling the structure and activity of comet nuclei. In: Festou MC, Keller HU, Weaver HA (eds) *Comets II*. University of Arizona Press, Tucson, p 359
- Pryor WR, Hord CW (1991) A study of photopolarimeter system UV absorption data on Jupiter, Saturn, Uranus, and Neptune: Implications for auroral haze formation. *Icarus* 91(1):161–172. [https://doi.org/10.1016/0019-1035\(91\)90135-G](https://doi.org/10.1016/0019-1035(91)90135-G)
- Pryor WR, West RA, Simmons KE et al (1992) High-phase-angle observations of Neptune at 2650 and 7500 Å: Haze structure and particle properties. *Icarus* 99(2):302–317. [https://doi.org/10.1016/0019-1035\(92\)90148-Z](https://doi.org/10.1016/0019-1035(92)90148-Z)
- Pryor WR, West RA, Simmons KE (1997) High-phase-angle observations of Uranus at 2650 Å: haze structure and particle properties. *Icarus* 127(2):508–522. <https://doi.org/10.1006/icar.1997.5706>
- Raponi A, De Sanctis MC, Carrozzo FG et al (2019) Mineralogy of Occator crater on Ceres and insight into its evolution from the properties of carbonates, phyllosilicates, and chlorides. *Icarus* 320:83–96. <https://doi.org/10.1016/j.icarus.2018.02.001>

- Raponi A, Ciarniello M, Capaccioni F et al (2020) Infrared detection of aliphatic organics on a cometary nucleus. *Nature Astron* 4:500–505. <https://doi.org/10.1038/s41550-019-0992-8>. arXiv:2009.14476 [astro-ph.EP]
- Reid JP (2009) Particle levitation and laboratory scattering. *JQSRT* 110:1293–1306. <https://doi.org/10.1016/j.jqsrt.2009.02.019>
- Renard JB, Hadamcik E, Levasseur-Regourd AC (1996) Polarimetric CCD imaging of comet 47P/Ashbrook-Jackson and variability of polarization in the inner coma of comets. *A&A* 316:263–269
- Renard JB, Hadamcik E, Worms JC (2024) The laboratory PROGRA2 database to interpret the linear polarization and brightness phase curves of light scattered by solid particles in clouds and layers. *JQSRT* 320:8
- Rosenbush V, Kiselev N, Velichko S (2002) polarimetric and photometric observations of split comet C/2001 A2 (LINEAR). *Earth Moon Planets* 90(1):423–433. <https://doi.org/10.1023/A:1021502904966>
- Rosenbush V, Kiselev N, Afanasiev V (2015) Icy moons of the outer planets. In: Kolokolova L, Hough J, Levasseur-Regourd AC (eds) *Polarimetry of stars and planetary systems*. Cambridge University Press, Cambridge, p 340
- Rosenbush VK (2002) The phase-angle and longitude dependence of polarization for Callisto. *Icarus* 159(1):145–155. <https://doi.org/10.1006/icar.2002.6879>
- Rosenbush VK, Rosenbush AE, Dement'ev MS (1994) Comets Okazaki-Levy-Rudenko (1989 XIX) and Levy (1990 XX): polarimetry and stellar occultations. *Icarus* 108(1):81–91. <https://doi.org/10.1006/icar.1994.1042>
- Rosenbush VK, Avramchuk VV, Rosenbush AE et al (1997) Polarization properties of the Galilean satellites of Jupiter: observations and preliminary analysis. *ApJ* 487(1):402–414. <https://doi.org/10.1086/304584>
- Rosenbush VK, Ivanova OV, Kiselev NN et al (2017) Spatial variations of brightness, colour and polarization of dust in comet 67P/Churyumov-Gerasimenko. *MNRAS* 469:S475–S491. <https://doi.org/10.1093/mnras/stx2003>
- Rossi L, Marq E, Montmessin F et al (2015) Preliminary study of Venus cloud layers with polarimetric data from SPICAV/VEx. *Planet Space Sci* 113:159–168. <https://doi.org/10.1016/j.pss.2014.11.011>
- Rouleau F, Martin PG (1991) Shape and clustering effects on the optical properties of amorphous carbon. *ApJ* 377:526. <https://doi.org/10.1086/170382>
- Rousselot P, Petit JM, Poulet F et al (2005) Photometric study of Centaur (60558) 2000 EC₉₈ and trans-neptunian object (55637) 2002 UX₂₅ at different phase angles. *Icarus* 176(2):478–491. <https://doi.org/10.1016/j.icarus.2005.03.001>
- Roy Choudhury S, Hadamcik E, Sen A (2014) A study of comet 78P/Gehrels by imaging polarimetry. *JQSRT* 146:444–451. <https://doi.org/10.1016/j.jqsrt.2014.02.010>, *Electromagnetic and Light Scattering by Nonspherical Particles XIV*
- Roy Choudhury S, Hadamcik E, Sen AK (2015) Study of some comets through imaging polarimetry. *Planet Space Sci* 118:193–198. <https://doi.org/10.1016/j.pss.2015.06.011>
- Saito M, Yang P, Ding J et al (2021) A comprehensive database of the optical properties of irregular aerosol particles for radiative transfer simulations. *J Atmos Sci* 78(7):2089–2111. <https://doi.org/10.1175/JAS-D-20-0338.1>
- Santer R, Dollfus A (1981) Optical reflectance polarimetry of Saturn's globe and rings IV. Aerosols in the upper atmosphere of Saturn. *Icarus* 48(3):496–518. [https://doi.org/10.1016/0019-1035\(81\)90060-9](https://doi.org/10.1016/0019-1035(81)90060-9)
- Santer R, Deschamps M, Ksanfomaliti LV, et al (1985) Photopolarimetric analysis of the Martian atmosphere by the Soviet MARS-5 orbiter. I. White clouds and dust veils. *A&A* 150(2):217–228
- Santer R, Deschamps M, Ksanfomaliti LV et al (1986) Photopolarimetry of Martian aerosols. II. Limb and terminator measurements. *A&A* 158(1–2):247–258
- Scarrott SM, Warren-Smith RF, Pallister WS et al (1983) Electronographic polarimetry: the Durham polarimeter. *MNRAS* 204:1163–1177. <https://doi.org/10.1093/mnras/204.4.1163>
- Schmid HM, Joos F, Tschan D (2006) Limb polarization of Uranus and Neptune. I. Imaging polarimetry and comparison with analytic models. *A&A* 452(2):657–668. <https://doi.org/10.1051/0004-6361:20053273>
- Schmid HM, Joos F, Buenzli E et al (2011) Long slit spectropolarimetry of Jupiter and Saturn. *Icarus* 212(2):701–713. <https://doi.org/10.1016/j.icarus.2011.01.016>. arXiv:1101.5000 [astro-ph.EP]
- Seager S, Whitney BA, Sasselov DD (2000) Photometric Light Curves and Polarization of Close-in Extrasolar Giant Planets. *ApJ* 540(1):504–520. <https://doi.org/10.1086/309292>, arXiv:astro-ph/0004001 [astro-ph]

- Serkowski K (1974) Polarimeters for Optical Astronomy. In: Gehrels T (ed) IAU Colloq. 23: Planets, Stars, and Nebulae: Studied with Photopolarimetry, p 135
- Shalygina OS, Korokhin VV, Starukhina LV et al (2008) The north-south asymmetry of polarization of Jupiter: The causes of seasonal variations. *Solar Syst Res* 42(1):8–17. <https://doi.org/10.1134/S0038094608010024>
- Shkuratov IG, Opanasenko NV, Kreslavskii MA (1992) Polarimetric and photometric properties of the Moon: Telescopic observations and laboratory simulations. 1. The negative polarization. *Icarus* 95(2):283–299. [https://doi.org/10.1016/0019-1035\(92\)90044-8](https://doi.org/10.1016/0019-1035(92)90044-8)
- Shkuratov Y, Ovcharenko A, Zubko E et al (2002) The opposition effect and negative polarization of structural analogs for planetary Regoliths. *Icarus* 159(2):396–416. <https://doi.org/10.1006/icar.2002.6923>
- Shkuratov Y, Ovcharenko A, Zubko E et al (2004) The negative polarization of light scattered from particulate surfaces and of independently scattering particles. *JQSRT* 88:267–284. <https://doi.org/10.1016/j.jqsrt.2004.03.029>
- Shkuratov Y, Kreslavsky M, Kaydash V et al (2005) Hubble Space Telescope imaging polarimetry of Mars during the 2003 opposition. *Icarus* 176(1):1–11. <https://doi.org/10.1016/j.icarus.2005.01.009>
- Shkuratov Y, Bondarenko S, Ovcharenko A et al (2006) Comparative studies of the reflectance and degree of linear polarization of particulate surfaces and independently scattering particles. *JQSRT* 100(1–3):340–358. <https://doi.org/10.1016/j.jqsrt.2005.11.050>
- Shkuratov Y, Bondarenko S, Kaydash V et al (2007) Photometry and polarimetry of particulate surfaces and aerosol particles over a wide range of phase angles. *JQSRT* 106(1–3):487–508. <https://doi.org/10.1016/j.jqsrt.2007.01.031>
- Shkuratov Y, Kaydash V, Korokhin V et al (2011) Optical measurements of the Moon as a tool to study its surface. *Planet Space Sci* 59(13):1326–1371. <https://doi.org/10.1016/j.pss.2011.06.011>
- Shkuratov YG (1987) Negative polarization of sunlight scattered from celestial bodies—interpretation of the wavelength dependence. *Sov Astron Lett* 13:182
- Shkuratov YG (1989) A new mechanism of formation of negative polarization of light scattered by the solid surfaces of cosmic bodies. *Solar Syst Res* 23(2):111
- Shkuratov YG, Muinonen K, Bowell E et al (1994) A critical review of theoretical models of negatively polarized light scattered by atmosphereless solar system bodies. *Earth Moon Planets* 65(3):201–246. <https://doi.org/10.1007/BF00579535>
- Siebenmorgen R, Voshchinnikov NV, Bagnulo S (2014) Dust in the diffuse interstellar medium. Extinction, emission, linear and circular polarisation. *A&A* 561:A82. <https://doi.org/10.1051/0004-6361/201321716>, [arXiv:1308.3148](https://arxiv.org/abs/1308.3148) [astro-ph.GA]
- Silva JE, Peralta J, Cardesin-Moinelo A et al (2024) Atmospheric gravity waves in Venus dayside clouds from VIRTIS-M images. *Icarus* 415:116076. <https://doi.org/10.1016/j.icarus.2024.116076>
- Smith PH, Tomasko MG (1984) Photometry and polarimetry of Jupiter at large phase angles II. Polarimetry of the South Tropical Zone, South Equatorial Belt, and the polar regions from the Pioneer 10 and 11 missions. *Icarus* 58(1):35–73. [https://doi.org/10.1016/0019-1035\(84\)90097-6](https://doi.org/10.1016/0019-1035(84)90097-6)
- Spadaccia S, Patty CHL, Capelo HL, et al (2022) Negative polarization properties of regolith simulants. Systematic experimental evaluation of composition effects. *A&A* 665:A49. <https://doi.org/10.1051/0004-6361/202243844>, [arXiv:2207.08767](https://arxiv.org/abs/2207.08767) [astro-ph.EP]
- Spadaccia S, Patty CHL, Thomas N et al (2023) Experimental study of frost detectability on planetary surfaces using multicolor photometry and polarimetry. *Icarus* 396:115503. <https://doi.org/10.1016/j.icarus.2023.115503>
- Sparks W, Hough JH, Germer TA et al (2012) Remote sensing of chiral signatures on Mars. *Planet Space Sci* 72(1):111–115. <https://doi.org/10.1016/j.pss.2012.08.010>. [arXiv:1209.0671](https://arxiv.org/abs/1209.0671) [astro-ph.EP]
- Sparks WB, Axon DJ (1999) Panoramic polarimetry data analysis. *PASP* 111(764):1298–1315. <https://doi.org/10.1086/316434>
- Sparks WB, Hough JH, Bergeron LE (2005) A search for chiral signatures on mars. *Astrobiology* 5(6):737–748. <https://doi.org/10.1089/ast.2005.5.737>
- Sparks WB, Hough J, Germer TA et al (2009) Detection of circular polarization in light scattered from photosynthetic microbes. *PNAS* 106(19):7816–7821. <https://doi.org/10.1073/pnas.0810215106>. [arXiv:0904.4646](https://arxiv.org/abs/0904.4646) [astro-ph.EP]
- Spoto F, Tanga P, Mignard F et al (2018) Gaia data release 2. Observations of solar system objects. *A&A* 616:A13. <https://doi.org/10.1051/0004-6361/201832900>. [arXiv:1804.09379](https://arxiv.org/abs/1804.09379) [astro-ph.EP]
- Stam DM (2008) Spectropolarimetric signatures of Earth-like extrasolar planets. *A&A* 482(3):989–1007. <https://doi.org/10.1051/0004-6361/20078358>. [arXiv:0707.3905](https://arxiv.org/abs/0707.3905) [astro-ph]







- Stam DM, Hovenier JW (2005) Errors in calculated planetary phase functions and albedos due to neglecting polarization. *A&A* 444(1):275–286. <https://doi.org/10.1051/0004-6361:20053698>
- Stam DM, De Haan JF, Hovenier JW et al (1999) Degree of linear polarization of light emerging from the cloudless atmosphere in the oxygen A band. *J Geophys Res* 104(D14):16843–16858. <https://doi.org/10.1029/1999JD900159>
- Stam DM, Aben I, Heldermer F (2002) Skylight polarization spectra: numerical simulation of the Ring effect. *J Geophys Res Atmos* 107(D20):4419. <https://doi.org/10.1029/2001JD000951>
- Stam DM, Hovenier JW, Waters LBFM (2004) Using polarimetry to detect and characterize Jupiter-like extrasolar planets. *A&A* 428:663–672. <https://doi.org/10.1051/0004-6361:20041578>
- Stankevich DG, Shkuratov YG, Muinonen K (1999) Shadow-hiding effect in inhomogeneous layered particulate media. *JQSRT* 63(2–6):445–458. [https://doi.org/10.1016/S0022-4073\(99\)00030-8](https://doi.org/10.1016/S0022-4073(99)00030-8)
- Sterzik M, Bagnulo S, Azua A et al (2010) Astronomy meets biology: EFOSC2 and the Chirality of Life. *The Messenger* 142:25–27
- Sterzik MF, Bagnulo S (2009) Search For Chiral Signatures in the Earthshine. In: Meech KJ, Keane JV, Mumma MJ, et al (eds) *Bioastronomy 2007: Molecules, Microbes and Extraterrestrial Life*, p 371
- Sterzik MF, Bagnulo S, Palle E (2012) Biosignatures as revealed by spectropolarimetry of Earthshine. *Nature* 483(7387):64–66. <https://doi.org/10.1038/nature10778>
- Sterzik MF, Bagnulo S, Stam DM et al (2019) Spectral and temporal variability of Earth observed in polarization. *A&A* 622:A41. <https://doi.org/10.1051/0004-6361/201834213>. arXiv:1811.12079 [astro-ph.EP]
- Sterzik MF, Bagnulo S, Emde C et al (2020) The cloudbow of planet Earth observed in polarisation. *A&A* 639:A89. <https://doi.org/10.1051/0004-6361/202038270>. arXiv:2006.05198 [astro-ph.EP]
- Stinson A, Bagnulo S, Tozzi GP et al (2016) Polarimetry of comets 67P/Churyumov-Gerasimenko, 74P/Smirnova-Chernykh, and 152P/Helin-Lawrence. *A&A* 594:A110. <https://doi.org/10.1051/0004-6361/201527696>. arXiv:1606.05192 [astro-ph.EP]
- Stokes G (1852) On the composition and resolution of streams of polarized light from different sources. *Trans Cambridge Phil Soc* 9:399
- Stolker T, Min M, Stam DM, et al (2017) Polarized scattered light from self-luminous exoplanets. Three-dimensional scattering radiative transfer with ARTES. *A&A* 607:A42. <https://doi.org/10.1051/0004-6361/201730780>. arXiv:1706.09427 [astro-ph.EP]
- Swamy KSK (2010) *Physics of Comets*, 3rd edn. World Scientific, <https://doi.org/10.1142/7537>
- Swedlund JB, Kemp JC, Wolstencroft RD (1972) Circular polarization of Saturn. *ApJ* 178:257–266. <https://doi.org/10.1086/151785>
- Takahashi J, Itoh Y, Akitaya H et al (2013) Phase variation of earthshine polarization spectra. *PASJ* 65:38. <https://doi.org/10.1093/pasj/65.2.38>. arXiv:1303.7168 [astro-ph.EP]
- Tanga P, Pauwels T, Mignard F et al (2023) Gaia data release 3. The solar system survey. *A&A* 674:A12. <https://doi.org/10.1051/0004-6361/202243796>. arXiv:2206.05561 [astro-ph.EP]
- Tazaki R, Dominik C (2022) The size of monomers of dust aggregates in planet-forming disks. Insights from quantitative optical and near-infrared polarimetry. *A&A* 663:A57. <https://doi.org/10.1051/0004-6361/202243485>. arXiv:2204.08506 [astro-ph.EP]
- Tholen DJ (1984) *Asteroid taxonomy from cluster analysis of photometry*. PhD thesis, University of Arizona
- Tishkovets VP, Jockers K (2006) Multiple scattering of light by densely packed random media of spherical particles: dense media vector radiative transfer equation. *JQSRT* 101(1):54–72. <https://doi.org/10.1016/j.jqsrt.2005.10.001>
- Tishkovets VP, Petrova EV (2013) Coherent backscattering by discrete random media composed of clusters of spherical particles. *JQSRT* 127:192–206. <https://doi.org/10.1016/j.jqsrt.2013.05.017>
- Tishkovets VP, Petrova EV (2020) An algorithm and codes for fast computations of the opposition effects in a semi-infinite discrete random medium. *JQSRT* 255:107252. <https://doi.org/10.1016/j.jqsrt.2020.107252>
- Tobon Valencia V, Geffrin JM, Ménard F et al (2022) Scattering properties of protoplanetary dust analogs with microwave analogy: Aggregates of fractal dimensions from 1.5 to 2.8. *A&A* 666:A68. <https://doi.org/10.1051/0004-6361/202142656>
- Tomasko MG (1980) Preliminary results of polarimetry and photometry of Titan at large phase angles from Pioneer 11. *J Geophys Res* 85(A11):5937–5942. <https://doi.org/10.1029/JA085iA11p05937>
- Tomasko MG, Doose LR (1984) Polarimetry and photometry of Saturn from Pioneer 11: Observations and constraints on the distribution and properties of cloud and aerosol particles. *Icarus* 58(1):1–34. [https://doi.org/10.1016/0019-1035\(84\)90096-4](https://doi.org/10.1016/0019-1035(84)90096-4)

- Tomasko MG, Smith PH (1982) Photometry and polarimetry of Titan: Pioneer 11 observations and their implications for aerosol properties. *Icarus* 51(1):65–95. [https://doi.org/10.1016/0019-1035\(82\)90030-6](https://doi.org/10.1016/0019-1035(82)90030-6)
- Trees VJH, Stam DM (2022) Ocean signatures in the total flux and polarization spectra of Earth-like exoplanets. *A&A* 664:A172. <https://doi.org/10.1051/0004-6361/202243591>. arXiv:2205.05669 [astro-ph.EP]
- Tropf WJ, Thomas ME (1998) Magnesium aluminum spinel (MgAl₂O₄). In: Palik ED (ed) Handbook of optical constants of solids. Academic Press, Boston, p 883–897, <https://doi.org/10.1016/B978-0-08-055630-7.50055-9>
- Trumbo SK, Davis MR, Cassese B et al (2022) Spectroscopic Mapping of Io's Surface with HST/STIS: SO₂ frost, sulfur allotropes, and large-scale compositional patterns. *Planet Sci J* 3(12):272. <https://doi.org/10.3847/PSJ/aca46d>. arXiv:2212.08783 [astro-ph.EP]
- Vaillon R, Geffrin JM (2014) Recent advances in microwave analog to light scattering experiments. *JQSRT* 146:100–105. <https://doi.org/10.1016/j.jqsrt.2014.02.031>
- Vaillon R, Geffrin JM, Eyraud C et al (2011) A new implementation of a microwave analog to light scattering measurement device. *JQSRT* 112:1753–1760. <https://doi.org/10.1016/j.jqsrt.2010.12.008>
- Väisänen T, Martikainen J, Muinonen K (2020) Scattering of light by dense particulate media in the geometric optics regime. *JQSRT* 241:106719. <https://doi.org/10.1016/j.jqsrt.2019.106719>
- van de Hulst HC (1957) Light scattering by small particles. Structure of matter series, Dover
- Vaughan SR, Gebhard TD, Bott K et al (2023) Chasing rainbows and ocean glints: Inner working angle constraints for the Habitable Worlds Observatory. *MNRAS* 524(4):5477–5485. <https://doi.org/10.1093/mnras/stad2127>. arXiv:2307.15137 [astro-ph.EP]
- Velikodsky YI, Opanasenko NV, Akimov LA et al (2011) New Earth-based absolute photometry of the Moon. *Icarus* 214(1):30–45. <https://doi.org/10.1016/j.icarus.2011.04.021>
- Veverka J (1971) A polarimetric search for a venus halo during the 1969 inferior conjunction. *Icarus* 14(2):282–283. [https://doi.org/10.1016/0019-1035\(71\)90065-0](https://doi.org/10.1016/0019-1035(71)90065-0)
- Veverka J (1971) Polarization measurements of the Galilean satellites of Jupiter. *Icarus* 14(3):355–359. [https://doi.org/10.1016/0019-1035\(71\)90006-6](https://doi.org/10.1016/0019-1035(71)90006-6)
- Veverka J (1973) Titan: Polarimetric evidence for an optically thick atmosphere? *Icarus* 18(4):657–660. [https://doi.org/10.1016/0019-1035\(73\)90069-9](https://doi.org/10.1016/0019-1035(73)90069-9)
- Videen G (2002) Polarization opposition effect and second-order ray tracing. *Appl Opt* 41(24):5115–5121. <https://doi.org/10.1364/AO.41.005115>
- Vokrouhlický D, Nesvorný D, Dones L (2019) Origin and evolution of long-period comets. *AJ* 157(5):181. <https://doi.org/10.3847/1538-3881/ab13aa>, arXiv:1904.00728 [astro-ph.EP]
- Volten H, Muñoz O, Rol E et al (2001) Scattering matrices of mineral aerosol particles at 441.6 nm and 632.8 nm. *J Geophys Res* 106(15):17375–17402. <https://doi.org/10.1029/2001JD900068>
- Wardle JFC, Kronberg PP (1974) The linear polarization of quasi-stellar radio sources at 37.1 and 11.1 centimeters. *ApJ* 194:249. <https://doi.org/10.1086/153240>
- Warren SG (2019) Optical properties of ice and snow. *Phil Trans R Soc A* 377(2146):20180161. <https://doi.org/10.1098/rsta.2018.0161>
- Weiss-Wrana K (1983) Optical properties of interplanetary dust—comparison with light scattering by larger meteoritic and terrestrial grains. *A&A* 126(2):240–250
- West RA, Smith PH (1991) Evidence for aggregate particles in the atmospheres of Titan and Jupiter. *Icarus* 90(2):330–333. [https://doi.org/10.1016/0019-1035\(91\)90113-8](https://doi.org/10.1016/0019-1035(91)90113-8)
- West RA, Hart H, Simmons KE et al (1983) Voyager 2 photopolarimeter observations of Titan. *J Geophys Res* 88(A11):8699–8708. <https://doi.org/10.1029/JA088iA11p08699>
- West RA, Hord CW, Simmons KE et al (1983) Voyager photopolarimeter observations of Saturn and Titan. *Adv Space Res* 3(3):45–48. [https://doi.org/10.1016/0273-1177\(83\)90254-5](https://doi.org/10.1016/0273-1177(83)90254-5)
- West RA, Dumont P, Hu R et al (2022) Spectropolarimetry as a means to address cloud composition and habitability for a cloudy exoplanetary atmosphere in the habitable zone. *ApJ* 940(2):183. <https://doi.org/10.3847/1538-4357/ac9b42>. arXiv:2211.06450 [astro-ph.EP]
- Wiktorowicz S, Nofi L (2015) Simultaneous linear and circular optical polarimetry of asteroid (4) Vesta. *ApJL* 800:L1
- Wöhler C, Arnaut M, Bhatt M (2024) Multiband spectropolarimetry of lunar maria, pyroclastics, fresh craters, and swirl materials. *AJ* 167(5):187. <https://doi.org/10.3847/1538-3881/ad2f2f>
- Wolstencroft RD (1974) The circular polarization of light reflected from certain optically active surfaces. In: Gehrels T (ed) *IAU Colloq. 23: Planets, Stars, and Nebulae: Studied with Photopolarimetry*, p 495

- Wolstencroft RD (1976) The circular polarization of the light from Jupiter. *Icarus* 29(2):235–243. [https://doi.org/10.1016/0019-1035\(76\)90051-8](https://doi.org/10.1016/0019-1035(76)90051-8)
- Wooden DH (2002) Comet grains: their IR emission and their relation to ISM grains. *Earth Moon Planets* 89(1):247–287. <https://doi.org/10.1023/A:1021515023679>
- Woodward CE, Jones TJ, Brown B, et al (2011) Dust in Comet C/2007 N3 (Lulin). *AJ* 141(6):181. <https://doi.org/10.1088/0004-6256/141/6/181>, [arXiv:1103.0593](https://arxiv.org/abs/1103.0593) [astro-ph.EP]
- Zaitsev S, Rosenbush V, Kiselev N (2020) Polarimetry of planetary satellites V1.0. NASA Planetary Data System p 1. <https://doi.org/10.26033/gpax-zx46>
- Zaitsev SV, Kiselev NN, Rosenbush VK et al (2015) Polarimetry of Saturn’s satellite Rhea. *Kinemat Phys Celestial Bodies* 31(6):281–285. <https://doi.org/10.3103/S0884591315060070>
- Zaitsev SV, Kiselev NN, Rosenbush VK et al (2015b) Polarimetry of Saturnian satellite Enceladus. *Adv Astron Space Phys* 5(1), 29–32. <https://doi.org/10.17721/2227-1481.5.29-32>
- Zellner B (1972) On the nature of Iapetus. *ApJL* 174:L107. <https://doi.org/10.1086/180959>
- Zellner B, Gradie J (1976) Minor planets and related objects: XX. Polarimetric evidence for the albedos and compositions of 94 asteroids. *Astron J* 81:262–280
- Zellner B, Gehrels B, Gradie J (1974) Minor planets and related objects. XVI. Polarimetric diameters. *Astron J* 79:1100–1110
- Zellner B, Leake M, Lebertre T, et al (1977) Polarimetry of meteorites and the asteroid albedo scale. Paper presented at the 8th Lunar and Planetary Science Conference, March 1977
- Zerull RH, Gustafson BAS, Schulz K et al (1993) Scattering by aggregates with and without an absorbing mantle: microwave analog experiments. *Appl Opt* 32(21):4088–4100. <https://doi.org/10.1364/AO.32.004088>
- Zhang Q, Kolokolova L, Ye Q et al (2022) Dust evolution in the coma of distant, inbound comet C/2017 K2 (PANSTARRS). *Planet Sci J* 3(6):135. <https://doi.org/10.3847/PSJ/ac6d58>. [arXiv:2205.02854](https://arxiv.org/abs/2205.02854) [astro-ph.EP]
- Zheltebryukhov M, Zubko E, Chornaya E et al (2020) Monitoring polarization in comet 46P/Wirtanen. *MNRAS* 498(2):1814–1825. <https://doi.org/10.1093/mnras/staa2469>. [arXiv:2012.12781](https://arxiv.org/abs/2012.12781) [astro-ph.EP]
- Zubko E, Videen G, Hines DC et al (2016) The positive-polarization of cometary comae. *Planet Space Sci* 123:63–76. <https://doi.org/10.1016/j.pss.2015.09.020>
- Zubko E, Zheltebryukhov M, Chornaya E et al (2020) Polarization of disintegrating Comet C/2019 Y4 (ATLAS). *MNRAS* 497(2):1536–1542. <https://doi.org/10.1093/mnras/staa1725>

Publisher's Note Springer Nature remains neutral with regard to jurisdictional claims in published maps and institutional affiliations.

Authors and Affiliations

Stefano Bagnulo¹  · Irina Belskaya²  · Alberto Cellino³  · Yuna G. Kwon⁴  · Olga Muñoz⁵  · Daphne M. Stam⁶ 

✉ Stefano Bagnulo
stefano.bagnulo@armagh.ac.uk

Irina Belskaya
ibelskaya@karazin.ua

Alberto Cellino
alberto.cellino@inaf.it

Yuna G. Kwon
yuna@ipac.caltech.edu

Olga Muñoz
olga@iaa.es

Daphne M. Stam
daphne.stam@vulcanoids.net

- ¹ Armagh Observatory & Planetarium, College Hill, Armagh BT61 9DG, Northern Ireland, UK
- ² Institute of Astronomy, V. N. Karazin Kharkiv National University, 35 Sum'ska str., Kharkiv 61022, Ukraine
- ³ INAF, Osservatorio Astrofisico di Torino, Torino 10025, Italy
- ⁴ Infrared Processing and Analysis Center (IPAC), California Institute of Technology, 1200 E California Blvd, MC 100-22, Pasadena, CA 91125, USA
- ⁵ Instituto de Astrofísica de Andalucía, CSIC, Glorieta de la Astronomía s/n, Granada 18008, Spain
- ⁶ Leiden Observatory, Einsteinweg 55, Leiden 2333 CC, The Netherlands